

Neutral and Ionic Molecules Observed in
Comet P/Halley

A thesis submitted for the degree of
Doctor of Philosophy

by

ALAN FITZSIMMONS BSc. (Sussex, 1985)

Department of Astronomy
University of Leicester
Leicester, England

May 1989

UMI Number: U017637

All rights reserved

INFORMATION TO ALL USERS

The quality of this reproduction is dependent upon the quality of the copy submitted.

In the unlikely event that the author did not send a complete manuscript and there are missing pages, these will be noted. Also, if material had to be removed, a note will indicate the deletion.



UMI U017637

Published by ProQuest LLC 2015. Copyright in the Dissertation held by the Author.
Microform Edition © ProQuest LLC.

All rights reserved. This work is protected against
unauthorized copying under Title 17, United States Code.



ProQuest LLC
789 East Eisenhower Parkway
P.O. Box 1346
Ann Arbor, MI 48106-1346



3384

X 751556082

750046847D

Abstract

This work is concerned with the study of the coma and gas tail of Halley's Comet. The thesis begins with a summary of the relevant background material. Theories of origin are discussed, after which the known properties of cometary comae, nuclei and tails are described.

Narrow-band photometry of Halley's Comet both pre- and post-perihelion is documented. The observations of the OH band at 3080\AA are discussed first, as it is a product of H_2O . Production rates and lifetimes against photodissociation are calculated using both the Haser Model and the Average Random Walk Model.

The variation of production rates of CN, C_2 and C_3 are discussed in the light of current knowledge of Halley's nucleus. Photodestruction lifetimes of these trace species are found using a Monte-Carlo modelling technique.

The analysis of large-scale image of the plasma tail of Halley is described, resulting in the determination of the solar wind velocity at the comet. The dynamics of the ions in the tail are demonstrated using a simple analytical approximation to the magnetic field structure. Observations of discrete plasma formations within the tail allow the measurement of the internal velocity field, from which an estimate of the tail magnetic field strength is derived.

The Comet at Yell'ham

It bends far over Yell'ham Plain,
And we, from Yell'ham Height,
Stand and regard its fiery train,
So soon to swim from sight.

It will return long years hence, when
As now its strange swift shine
Will fall on Yell'ham; but not then
On that sweet form of mine.

Thomas Hardy (1840-1928)

Acknowledgements

To any historians of astronomy reading this work when Halley returns in 2051 AD, the following people should take at least a part share of the blame:

First and foremost, I am deeply indebted to Dr. Dave Adams for all the help and encouragement he has given me as his research student and friend over the years. Thanks are also due to Prof. Jack Meadows for commencing the onerous task of tutoring me during my first year.

Working in the Leicester University Astronomy Department was made all the more pleasant by the company of several people. Remembered well are the following; Charon for those infamous hand-waving discussions, John for showing me how to make friends with the computer, Marko for giving me the answers to the crosswords and Simon for being Simon. Cheers also to the lecturers and postdocs who had to put up with my general optimism for three years. Special mention must be made of Norma, for generally running the whole thing and handing me all those dodgy phonecalls.

My friends all took their turns in providing advice, company and a shoulder when the going got rough. Good fortune to my comrades in arms, Alastair and Andy. How come we all survived? Best wishes to Pete and S.T. for showing me life after work. Thanks too to Jaytee, for just listening to me ramble on about astronomy. Nearer my roots, who would I go to the pub with if not Richard, Steve and Ian? My round, lads.

The actual observing of Halley was made all the more enjoyable by the friendship and experience of Iwan Williams, Peter Andrews and Gillian Williams. Thanks also to Ken Russel for taking the schmidt plates of Halley, and Sue Tritton and Harvey McGillivray for all the help given.

Financial support from the Science and Engineering Research Council is gratefully acknowledged.

Last but certainly not least, thank you to all of my family, who for some strange reason have always thought I'd finish this. Numbers and ongoing fertility stop me from naming everybody. My mother and my not-so-young brother, Mrs Joan Fitzsimmons and Mr William Fitzsimmons, have always been there to support me. Finally, I would like to dedicate this thesis to my late father, Mr. Neil Fitzsimmons, who forever spurred me on and forevermore will. Thanks, Dad.

Alan Fitzsimmons

May 18th 1989

Contents

	page
Chapter I - An Overview of Cometary Science	
I.1 Introduction	I-1
I.2 The origin and orbits of comets	I-4
I.3 Cometary Nuclei	I-7
I.4 The coma	
I.4.1 The gaseous component	I-12
I.4.2 The dust component	I-16
I.5 The tails of comets	
I.5.1 Dust tails	I-19
I.5.2 Ion tails	I-20
I.6 References	I-23
Chapter II - Photometry of Halley and OH Results	
II.1 Introduction	II-1
II.2 Cometary photometry	II-3
II.3 Observations	II-5
II.4 Reduction	II-11
II.5 The Haser model	II-15
II.6 OH analysis	
II.6.1 Scalelengths and lifetimes	II-18
II.6.2 Production at nucleus	II-26
II.7 References	II-30

page

Chapter III - Analysis of Carbon-based Molecules

III.1	Introduction	III-1
III.2	Molecular production ratios	III-3
III.3	Variability of outgassing	III-12
III.4	Models involving molecular kinetics	
III.4.1	The average random walk model	III-17
III.4.2	The Monte-Carlo model	III-19
III.5	Coma distributions and molecular lifetimes	
III.5.1	Suitability of data	III-25
III.5.2	CN	III-26
III.5.3	C ₂	III-35
III.5.4	C ₃	III-42
III.6	Future work	III-45
III.7	References	III-47

Chapter IV - The Behaviour of Halley's Plasma Tail

IV.1	Introduction	IV-1
IV.2	The solar wind and the imf	IV-3
IV.3	The ion tail of P/Halley and the solar wind	
IV.3.1	Introduction	IV-7
IV.3.2	Observations	IV-8
IV.3.3	Analysis	IV-9
IV.3.4	Results	IV-19
IV.4	Magnetotail structure	IV-23

	page
IV.5 The velocity field in the ion tail	
IV.5.1 Observations	IV-29
IV.5.2 Reduction	IV-30
IV.5.3 The observed velocity field	IV-35
IV.5.4 The tail B-field	IV-39
IV.6 Conclusions and future work	IV-43
IV.7 References	IV-45
Appendix	A-1

Chapter I

AN OVERVIEW OF COMETARY SCIENCE

I.1 INTRODUCTION

Take a large iceberg, ‘Titanic’ sized or larger. Sprinkle liberally with coal dust. Now place it in an elongated orbit about the Sun with a period between 3 years and 3×10^6 years. You have now created your own comet. Even though this appears as rather a simple (and frivolous) description, it essentially embodies over two centuries of scientific investigation. The recent fly-bys of Comet Halley by *Giotto*, *Vega-1*, *Vega-2*, *Suisei*, *Sakigake* and *ICE*, together with the corresponding ground-based observations (of which this work forms a part) have enormously increased both our understanding

of and our puzzlement over these primitive bodies.

It was Halley (1705) who first used Newton's laws of gravitation to show that comets were viable members of the solar system. He demonstrated that a particular comet had returned to the inner solar system at least twice before his observations of 1680. By calculating the orbital elements he successfully predicted its ensuing return in 1755. Since its discovery Halley's Comet has maintained an important standing in cometary science, due to its brightness and orbital period of 76 years. Study of the orbits of comets has revealed important clues concerning both the origin of comets and the formation of the solar system. Current knowledge of this topic is summarised in section 1.2.

Speculation as to what lies at the heart of a comet was only settled in the middle of this century. A theory that the nucleus of a comet was composed of a mass of particles bound by mutual gravitation explained the observed correspondence between certain meteor streams and known cometary orbits. However it had considerable difficulty in explaining (a) the large quantity of mass ejected from the nuclear region at each perihelion passage, and (b) explaining how comets passing close to the sun are not disrupted by tidal forces. This problem was resolved in Whipple's (1950) landmark paper, in which he outlined a quantitative model of a solid nucleus of order 1–10 km in size, consisting of a homogeneous mass of frozen gases (predominantly H₂O)

and dust particles. Further advances in the understanding the nucleus are described in section I.3.

Solar radiation heats the surface of the nucleus as the comet approaches perihelion, which then releases material into the surrounding vacuum to form an atmospheric coma. The visible coma may extend some 10^4 to 10^6 km from the nucleus. Its spectrum reveals the two physical components ejected from the nucleus. Dust particles reflect the solar spectrum at visible wavelengths, and thermally re-radiate the absorbed heat in the infra-red. Superimposed on the reflected solar spectrum are emission lines from various molecular species. Section I.4 describes the physical nature of the coma.

Finally, there are the most striking phenomena associated with comets, the dust and gas tails. These are usually over 10^6 km in length. Gas tails have been observed to stretch some 2×10^8 km from the nucleus. The formation and observed morphology of these features is discussed in section I.5.

I.2 THE ORIGIN AND ORBITS OF COMETS.

Over 600 cometary orbits are catalogued (Marsden, 1982). Broadly speaking this allows comets to be classified into two groups. The majority of periodic comets observed have their aphelia a in the region of Jupiter and Saturn, corresponding to orbital periods of 3 to 20 years. These are known as Short-Period Comets (SPC's). Most bright comets seen tend to have $a > 10^3$ AU, with corresponding orbital periods of thousands of years or more. These are termed Long-Period Comets (LPC's). The boundary between these two sets is marked by the Intermediate-Period Comets (IPC's), the best-known example being P/Halley.

The clue to the origin of comets was first discovered by Oort (1950). Plotting the number of comets with aphelia in a given range against aphelion distance, Oort found a large, statistically significant peak at $a = 10^5$ AU. His original data are shown in Table I.1. He immediately realised that the observed orbital distribution was evidence for a large spherically symmetric comet cloud surrounding the solar system at this mean radius. Comets formed in the primordial solar nebula were thrown out of the planetary region, whence perturbations caused by nearby stars would remove any remaining tendency for the orbital inclination to lie in the ecliptic plane.

Studies since then have mainly concentrated on deducing the formation site of comets and the total mass contained within the Oort cloud, using the

Interval of $1/a$ (10^{-5}AU^{-1})	No. of Comets
0–5	10
5–10	4
10–15	1
15–20	1
20–25	1
25–50	1
50–75	1

Table I.1: The original orbital data denoting the existence of the Oort cloud. From Oort (1950).

orbital distribution as the fundamental observational datum. The primary contributing factors to models of cometary formation are the assumed structure of the protoplanetary disk and the rate of accretion. Opik (1975 and references therein) and Safronov (1977 and references therein) both developed models with a low mass disk of $0.1 M_{\odot}$, but disagreed on the site of cometary formation. On the other hand Cameron (1973) preferred a $1 M_{\odot}$ disk. There were also theories of comet growth outside the planetary region by Cameron (1978) and Biermann and Micheal (1978).

The survivability of these competing theories was lowered considerably by the discovery of Giant Molecular Cloud (GMC) complexes in the 1970's. Napier (1985) and Bailey (1986) have shown that there have been ~ 10 encounters of the solar system with GMC's since the planetary system formed.

Such encounters would effectively strip away from the sun's gravitational influence any comets at heliocentric distances of $R_h \geq 3 \times 10^4$ AU. Thus it seems that the Oort cloud as envisaged cannot exist *per se*, implying a source of replenishment.

At the moment there are considered to be two possible sources for repopulating the Oort cloud. Hills (1981) has proposed the existence of a dense cloud of comets lying at a mean heliocentric distance of 10^3 AU. Mendis (1973) had originally proposed an inner disc of LPC's at $R_h < 10^4$ AU. Trajectory determinations for the Pioneer 10 spacecraft out to 35 AU show that the mass within such a cloud must be less than 5 Earth masses (Anderson and Standish Jr., 1986). A somewhat speculative assessment of the past history of P/Halley's orbit by Olsson-Steel (1988) concluded that Halley may well have originated from a Hills cloud.

Another suggestion as to how to restock the Oort cloud was first put forward by Reeves (1974). He suggested that comets may somehow form at the heliopause, the turbulent boundary where the solar wind meets the interstellar medium. McCrea (1975) has shown that cometary-sized masses may accrete in a region of essentially interstellar density if given a sufficient timespan. In a similar vein, Bailey (1987) has recently formulated a theory of cometary formation due to stellar winds around young early-type stars.

I.3 COMETARY NUCLEI

Perhaps the simplest observation to attempt on a nucleus is to determine the rotation period, via photometric study of the light curve. This is quite difficult because comets generally only become bright with the formation of the coma, a process which may shield the nucleus from observation. Unless the activity is confined to a relatively small area of the nucleus (which would 'switch' off during local night), photometry must be performed either on comets with a negligible coma (i.e. at heliocentric distances $R_h > 5$ AU) or on comets with highly inactive surfaces. Previous studies of rotation using photometric data yield periods in the range 0.28-1.13 days (Spinrad, 1987).

Whipple's (1982) study of the expanding dust haloes of comets should be mentioned. Rotation periods of 47 comets were derived from observations of expanding dust haloes. He found periods between 0.18 and 5 days. A surprising outcome from the intense study of Comet Halley is that the rotation period of the nucleus is still uncertain. There are currently two favoured periods of 2.2 days and 7.4 days. This is discussed in Chapter III.

The most dramatic result of the *Giotto* and *Vega* spacecraft fly-bys of P/Halley in March 1986 was the direct imaging of the nucleus (Keller *et al.*, 1986). Yet, as with all the other findings from the space missions, the true importance lies in a comparison with other comets. It is extremely difficult to observe most nuclei from Earth, as even at a distance of 0.03 AU (achieved

by IRAS-Araki-Alcock in 1983), a 10km-radius nucleus would only subtend 0.8 arcsec. Direct imaging is therefore impossible except for large nuclei at very small geocentric distances.

Photometry of bare nuclei yield the product of geometric albedo p_v and the effective nuclear radius R_e via

$$F_{\odot} R_e^2 p_v \psi(\alpha) = F_{\circ} R_h^2 \Delta^2 \quad (\text{I.1})$$

where F_{\odot} and F_{\circ} are the incident and reflected solar fluxes at the cometary surface and $\psi(\alpha)$ is the scattering phase function (Spinrad, Stauffer and Newburn Jr., 1979). R_h and Δ are the heliocentric and geocentric distances of the comet respectively. Assuming that $\psi(\alpha)$ is generally similar to that measured for asteroids, determination of radii depends on determination of the albedo. This may be avoided by instead fitting the observed photometric infra-red spectrum to a black-body flux distribution. Then the flux density is given by

$$f_{\lambda} = \frac{\varepsilon R_e^2 \pi B_{\lambda}(T)}{\Delta^2} \text{ W cm}^{-2} \quad (\text{I.2})$$

where ε is the emissivity and $B_{\lambda}(T)$ is a planck function. This allows the albedo of nuclei to be derived.

Hartmann, Crouikshank and Tholen (1985) derive a mean geometric albedo of $p_v = 0.051 \pm 0.010$ from 17 comets. This compares well with that measured by Keller *et al.* (1986) via direct imaging of Halley's surface, of $p_v = 0.04$. Such a dark nucleus was predicted by Brin and Mendis (1979)

Comet	Radius (km)	Method	Reference
P/Temple 2	4.4	photometry	Spinrad, Stauffer & Newburn Jr. (1979)
P/Encke	1.0	radar	Kamoun <i>et al.</i> (1982)
P/Encke	3.5	photometry	Mendis, Houpis & Marconi (1985)
P/Arend-Rigaux	5.0	photometry	Brook and Knack (1986)
P/Arend-Rigaux	4.5	photometry	Birkett <i>et al.</i> (1986)
P/Arend-Rigaux	5.2	photometry	Millis, A'Hearn & Campins (1988)
P/Neujmin 1	9.5	photometry	A'Hearn (1986)
Meier	13.0	photometry	Fernandez and Jockers (1983)
IRAS-Araki-Alcock	4.0	radar	Goldstein, Jurgens & Sekanina (1984)
Wirtanen	~50.0	photometry	Mendis, Houpis & Marconi (1985)
Scwassman-Wachmann 1	48.0	photometry	Mendis, Houpis & Marconi (1985)

Table I.2: Radii of nuclei as derived from ground-based observations

and earlier by Shul'man (1972). The low albedo is caused by dust grains too massive to be ejected from the nucleus via outgassing raining back down onto the surface, eventually accumulating to form a dark crustal material. As noted by Wallis and Wickramasinghe (1987) an organic-based crust will be thermally processed into a largely cohesive structure a few centimeters deep.

Using $p_v = 0.02$ as a lower limit to the albedo of cometary nuclei, Spinrad (1987) lists effective radii for six comets. These are included in Table I.2 with other known cometary albedo-area products. Note that higher albedos would require correspondingly smaller cometary dimensions. Two of these comets

appear to have substantially larger nuclei than the norm ($R_e \simeq 50$ km). The existence of such large nuclei (if proven) would have important implications for the theories of formation outlined in section 1.2.

Early observations of the SPC P/Enke revealed large discrepancies between the calculated orbit and that observed at subsequent perihelion passages. This is the result of the reaction of the outflowing jetting material against the nucleus, producing a rocket effect. Marsden, Sekanina and Yeomans (1973) derived an equation of motion that included non-gravitational accelerations both in and perpendicular to the plane of the orbit. The visual appearance of these jets allowed Sekanina and Larson (1984) to determine both spin-pole orientations and rotation rates. Perhaps more importantly, an estimate of the total momentum of the sublimating gases can lead to the determination of the masses of cometary nuclei.

The photometric determination of size also points to the mass, assuming that the density is known. This last point is very important and depends generally on the assumed internal constitution and structure of a nucleus. The non-gravitational motions of comets as studied by Whipple (1950) were well correlated with measured mass-loss rates of a bare-ice nucleus and a density of ~ 1 gm cm⁻³. The lower albedos now accepted imply a lower density to account for the measured orbital perturbations. Rickmann *et al.* (1987) have performed detailed calculations for the case of P/Halley,

resulting in a mean density of $0.1 < \rho < 0.2 \text{ gm cm}^{-3}$. Such low densities (for what is basically a water-ice structure) suggest a high porosity within the nucleus. This seems incompatible with the icy-glue structure envisaged by Gombosi and Houpis (1986), instead pointing towards fractal models as suggested by Donn and Hughes (1986) and Lang (1987).

I.4 THE COMA

I.4.1 The Gaseous Component.

As the gases sublime from the surface they create the atmosphere of the comet known as the coma. The main process by which the various molecular species are observed is resonance fluorescence with solar photons. For the optically thin case, the luminosity is simply equal to the the number of molecules present multiplied by the excitation rate g_λ , given by

$$g_\lambda = \frac{\pi e^2}{m_e c^2} f \frac{F_\odot(\lambda)}{R_h^2} \tilde{\omega} \quad (\text{I.3})$$

where f is the oscillator strength and $\tilde{\omega}$ is the branching ratio for the transition concerned. This is

$$\tilde{\omega} = \frac{A_{v'v''}}{\sum_{v'v''} A_{v'v''}} \quad (\text{I.4})$$

where $A_{v'v''}$ is the relevant Einstein transition probability. The optical depth of the coma is $\ll 1$ at all distances resolvable from Earth i.e. within a nuclear radius or so (Divine *et al.*, 1985). This then allows the direct determination of molecular column densities as seen from Earth.

A ‘typical’ spectrum of a comet at visible wavelengths is presented in figure I.1. Quite noticeable is the absence of any emission lines from the dominant components of cometary nuclei, H_2O and CO_2 . This is because, firstly they have relatively small g -factors, and secondly that their main emission lie at wavelengths other than the visible. Optical spectra are dominated

Figure I.1: Spectrum of Comet Kohoutek 1973 XII. From A'Hearn (1975).

by carbon-based molecular bands, particularly C_2 and CN. If these were out-gassed directly from the nucleus, then projection effects coupled with number conservation would give rise to an $I \propto d^{-1}$ brightness distribution. But the observed column density fall-off is convex in character, pointing to both creation of these molecules at some intermediate point in the coma and their eventual destruction. One of the early successes of coma studies was the creation by Haser (1957) of an analytical model for the brightness distributions of cometary comae. He identified the observed molecular species as daughter molecules, whose parents had been photodissociated by solar radiation in a characteristic lifetime, and who in turn were photodissociated (see Chapter

II for a full discussion). Since then other models have been formulated (See Chapter III) to take into account other physical parameters such as excess kinetic energy from dissociation, velocity distributions and solar radiation pressure.

Table I.3 contains all molecules and ions observed in Halley's comet, together with the suspected parentage. In some cases the source of a particular species is by no means clear. This may be due to a three-stage dissociation process taking place as derived in the case of C_2 by O'Dell *et al.* (1988) or by complex chemical reactions taking place near the surface of the nucleus. Another possibility is that of emission of molecules from dust grains, more of which will be said in chapter III.

The spacecraft missions to Halley confirmed several predictions of cometary coma models. Major achievements included the first detection of the abundant species H_3O^+ and CO_2 , and *in-situ* measurement of the densities and velocities prevalent within the coma. Evidence was gathered for new species such as $C_3H_3^+$ (Korth *et al.*, 1989), and the probable first discovery of a polymer in space, $(H_2CO)_n$ (polyoxymethelene or POM) by Huebner, Boice and Sharp (1987). It remains to be seen if such molecules can account for the unknown sources of C_3 and C_2 .

For molecules with either large g -factors and/or large lifetimes, the resulting radiation pressure inherent in the scattering process serves to distort

Neutral Species	Dominant Parent Molecules	Ionic Species	Dominant Parent Molecules
H ₂ O	-	H ⁺	H ₂ O
O	H ₂ O	H ₂ ⁺	H ₂ O
H	H ₂ O	O ⁺	H ₂ O
OH	H ₂ O	OH ⁺	H ₂ O
CO ₂	-	H ₂ O ⁺	H ₂ O
CO	CO ₂ ?	H ₃ O ⁺	H ₂ O
C	CO ₂ ?	CO ⁺	CO ₂ ?
HCN	-	C ⁺	CO ₂ ?
CN	HCN	CH ⁺	?
C ₂	?	C ₃ H ₃ ⁺	?
C ₃	?	S ⁺	S ₂
NH ₂	NH ₃ ?	Na ⁺	?
NH	NH ₃ ?	Fe ⁺	?
NO	?		
SO	?		
CH	?		
S	S ₂		
S ₂	CS ₂ ?		
CS	CS ₂ ?		

Table I.3: Atomic and molecular species observed in Halley, together with the primary parent (ignoring the number of intermediate reactions). A ‘-’ means a species released directly from the nucleus. A ‘?’ indicates uncertain or unknown parentage.

the coma from spherical symmetry. Well observed species susceptible to this are H and CN. Keller and Meier (1976) have simulated the hydrogen comae of comets with a model that takes into account both the initial velocity distributions of the atomic hydrogen and the differential orbital motion of the comet. His analysis demonstrated the existence of two independent populations of hydrogen atoms; a slow family with velocities around 8 km s^{-1} resulting from the dissociation of H_2O into $\text{OH}+\text{H}$, and a faster travelling component at 20 km s^{-1} whose parent was OH, thus being a grand-daughter of H_2O .

I.4.2 The Dust Component.

The dust coma is formed from non-volatile grains of material that were initially dragged outwards with the expanding gases at sublimation velocities of around 0.6 km s^{-1} at $R_h = 1 \text{ AU}$. The grains decouple from the gas at around 10–100 km above the nucleus (Finson and Probst, 1968). Whereas any molecular orientation of outflow is quickly destroyed by inter-molecular collisions, the dust particles are immune to this and thus remain in collimated jets, each jet being associated with an active area on the nucleus. As the grains expand sunward, they are retarded in their flight via radiation pressure. The dust coma forms a parabolic ‘hood’ around the nucleus of dimensions typically 10^5 km across. The particles are then accelerated out

Wavelength	Identification	Reference
2.8 μm	?	Tokunaga, Nagata & Smith(1987)
3.1-3.2 μm	Water ice	Bregman <i>et al.</i> (1987)
3.2-3.6 μm	C-H bonds	Knacke, Brooke & Joyce (1987)
6.8 μm	Carbonates, various organic molecules	Bregman <i>et al.</i> (1987)
$\simeq 10$ μm	Silicates	Bregman <i>et al.</i> (1987)
	Organic molecules + Polyoxymethelene	Wickramasinghe, Wallis & Hoyle (1988)
$\simeq 20$ μm	Silicates	Herter, Campins & Gull (1987)
23.5 μm	?	Herter, Campins & Gull (1987)
28.4 μm	?	Herter, Campins & Gull (1987)

Table I.4: Observed emission and absorption features in thermal spectra.

of the coma to form the dust tail (see Section I.5.2).

Ground-based studies of dust tails before Halley suggested a minimum size of around 0.5 μm for a grain density of 2 g cm⁻³. Birkett (1988) deduced a smaller lower diameter limit of 0.12 μm for a mean density of 1 gm cm⁻³ in Comet P/Halley. Both the Giotto and Vega craft however detected grains at the lowest masses detectable of < 10⁻¹⁶ gm (Vaisberg, Smirnov and Omelchenko, 1986) (McDonnell *et al.*, 1986) corresponding to $d_{\text{grain}} \sim 0.03$ μm . Such sub-micron grains are not visible from Earth because they scatter solar photons inefficiently.

Studies of the thermal spectra from the grains have detected several emission features, listed in Table I.4. Note that only two of these had been observed before the last apparition of P/Halley. It is apparent that sub-

stantial uncertainties remain over the identification of these features. Prior to the spacecraft encounters, the best derivation of the composition of the grains came from 'Brownlee' particles collected in the Earth's upper atmosphere (Butterworth, 1984). Approximately 60% of these particles have an elemental composition similar to C1 and C2 carbonaceous chondrite meteorites, which are thought to be the most primitive of all meteoritic material gathered.

Langevin *et al.* (1987) has shown that the dust grains in Halley's environment analysed in-situ can be chemically classed into three categories. 35% have a mineral composition similar to carbonaceous chondrites. Another 30% have abundances dominated by the light elements carbon, oxygen, nitrogen and hydrogen – the so-called 'CHON' grains. The remaining 35% of dust studied seemed to be a mixture of these two groups. The dust impact mass analyser (PUMA) on Vega 1 suggests that Chon grains correspond to the majority of low-mass particles detected by other experiments (Kissel *et al.*, 1986), while the SP-1 plasma impact detector onboard Vega-1 furnished evidence that the dust particles in general have low densities and/or fluffy structures (Smirnov, Vaisberg and Omelchenko, 1987).

I.5 THE TAILS OF COMETS

I.5.1 Dust Tails.

A very successful model for the visual appearance of dust tails was developed by Finson and Probst (1968). In this they account for the dust-gas coupling within the inner coma of a water-ice based nucleus, and then derive the resulting equations of motion of the particles. The observed morphology of the dust tail is then a function of the initial size distribution, outflow velocity and (time-dependant) production rate of the grains. Recently both Fulle (1987) and Richter and Keller (1987) have enhanced the theory, reducing the computational effort involved.

Generally speaking, one can consider a distribution of particles ejected from the nucleus at a given time, or a single size of particle outflowing continuously. The former mechanism will give rise to a stream of particles in the tail lying on a locus known as a synchrone. The latter situation gives produces a similar effect, known as a syndyne. Birkett (1988) has shown that the visual appearance of the dust tail of Halley Comet post-perihelion was governed by a series of outbursts from the nucleus that occurred pre-perihelion, creating the observed synchronic structures.

Quantitative imaging of dust tails has always been difficult to obtain, due to the exceedingly large area of sky covered by the tail. Again the knowledge

of the forthcoming apparition of Halley allowed the development of devices useful not only for this purpose but other astronomical research as well. Notable are the CCD-based system used by Lamy, Pederson and Vio (1987) and the IPCS detector operated by Rees, Meredith and Wallis (1986). In particular, Lamy, Pederson and Vio (1987) observed a reddening to occur as one progresses further downtail, a feature observed before in Comet West. The question as to whether this is due to contamination with the ion tail, or actual changes in bulk grain properties (sublimation, size) remains open.

I.5.2 Ion Tails.

All gaseous elements released by the nucleus will eventually be photo-ionised by solar radiation, on a time-scale of around 10^6 seconds. The ionized molecules will be picked up by the IMF (interplanetary magnetic field) that is carried out from the sun's surface with the solar wind. The IMF field lines themselves are draped over the cometary ionosphere, forming a magnetotail. The direction of this is given by the vector sum of the solar wind velocity together with the comets orbital velocity. The 'pick-up' ions then will be swept into the anti-solar direction to form the ion or plasma tail.

Some of the physical processes governing the structure of the ion tail will be discussed in Chapter 4. It is appropriate here to discuss the features seen frequently in plasma tails bright enough to be studied from Earth i.e. those

of relatively high column density produced by bright comets.

A well documented but poorly understood entity is the tail-ray. These appear as linear filaments of plasma attached to the inner coma with a width of $< 10^4$ km, and may reach lengths of $> 10^6$ km. They usually first appear at an angle to the main tail axis, then turn towards and merge with the central tail in a timescale of 15-25 hours, lengthening as they do so (Brandt, 1982). They frequently appear in pairs, one either side of the nucleus, perhaps implying that the rays are actually the projection of a thin sheet of plasma (Ip and Axford, 1982). A major unsolved problem is the discreteness of these features, and how they stop diffusing into the general ionic background.

At times the tail displays prominent kinks. As the tail direction is taken to be the vector sum of the comet's orbital motion and the solar wind velocity, this implies near-discontinuous changes in the solar wind flow vector. Such an occurrence in the tail of Comet Bennet 1970XII was investigated by Jockers and Lüst (1973).

Perhaps the best studied of all ion-tail features is the disconnection event or D.E. At times of D.E.'s the whole tail appears to be 'snipped' from the inner coma, as a new tail develops to take its place. Several of these were seen in the 1986 apparition of Halley (Brandt and Niedner, 1986). There exist two schools of thought as to the mechanism of detachment. Niedner and Brandt (1978) have proposed a model in which the comet encounters a

sector boundary in the solar wind, where the IMF direction moves through a large angle ($> 90^\circ$) over a (vanishingly) small distance. This causes magnetic reconnection to take place on the sunward boundary of the ionosphere, with the old field lines and attached plasma transported downtail as the new field lines drape themselves over the comet head.

The rival theory draws an analogy from processes observed in the Earth's magnetosphere, as described by Russel *et al.* (1986). The arrival at the comet of a high-speed solar wind stream causes reconnection to occur on the tail side of the ionosphere, with the subsequent release of plasma downtail. Correlations of D.E's with crossings of the solar neutral line by comets as investigated by Niedner and Brandt favour the former method, but there exists observational evidence also for the latter process (Jockers, 1985). In reality both mechanisms probably take place.

I.6 REFERENCES.

A'Hearn, M.F., 1975, *Astron. J.*, **80**, 861.

A'Hearn, M.F., 1986, in *Asteroids, Comets, Meteors II.*, ed. Lagerkvist, C.-I., Lindblad, B.A., Lundstedt, H., Rickmann, H., Uppsala University, 187.

Anderson, J.D., & Standish Jr., E.M., 1986, in *The Galaxy and The Solar System*, ed. Smoluchowski, R., Bahcall, J.N. & Matthews, M.S., University Arizona Press, Tucson, 287.

Bailey, M.E., 1986, *Mon. Not. R. astr. Soc.*, **218**, 1.

Bailey, M.E., 1987, *Icarus*, **69**, 70.

Biermann, L., & Michel, K.W., 1978, *Moon & Planets*, **18**, 447.

Birkett, C.M., Green, S.F., Zarnecki, J.C. & Russel, K.S., 1987, *Mon. Not. R. astr. Soc.*, **225**, 285.

Birkett, C.M., 1988, *Mon. Not. R. astr. Soc.*, **235**, 497.

Brandt, J.C., 1982, in *Comets*, ed. Wilkening, L., University Arizona Press, Tucson, 519.

Brandt, J.C. & Niedner Jr., M.B., 1986, *ESA SP-250*, **I**, 47.

Bregman, J.D., Campins, H., Witteborn, F.C., Wooden, D.H., Rank, D.M., Allamandola, L.J., Cohen, M. & Tielens, A.G.G.M., 1987, *Astron.*

Astrophys., **187**, 616.

Brin, G.D. & Mendis, D.A., 1979, *Astrophys. J.*, **229**, 402.

- Brooke, T.Y. & Knacke, R.F., 1986, *Icarus*, **67**, 80.
- Butterworth, P.S., 1984, *Vist. Astron.*, **27**, 1984.
- Cameron, A.G.W., 1973, *Icarus*, **18**, 407.
- Cameron, A.G.W., 1978, *Moon & Planets*, **18**, 5.
- Divine, N., Fechtig, H., Gombosi, T.I., Hanner, M.S., Keller, H.U., Larson, S.M., Mendis, D.A., Newburn Jr., R.L., Reinhard, R., Sekanina, Z. & Yeomans, D.K., 1986, *Sp. Sci. Rev.*, **43**, 1.
- Donn, B. & Hughes, D., 1986, *ESA SP-250*, **III**, 523.
- Goldstein, R.M., Jurgens, R.F. & Sekanina, Z., *Astron. J.*, **89**, 1745.
- Fernandez, J.A. & Jockers, K., 1983, *Rep. Progr. Phys.*, **46**, 665.
- Finson, M.L. & Probst, R.F., 1968, *Astrophys. J.*, **154**, 327.
- Fulle, M., 1987, *Astron. Astrophys.*, **171**, 327.
- Gombosi, T.I. & Houppis, H.L.F., 1986, *Nature*, **324**, 43.
- Goldstein, R.M., Jurgens, R.F. & Sekanina, Z., 1984, *Astron. J.*, **89**, 1745.
- Halley, E., 1705, *Synopsis Astronomiae Cometiariae*, London.
- Hartmann, N.K., Couikshank, D.P. & Tholen, D.J., 1985, in *Ices in the Solar System*, ed. Klinger, J. et al., 169.
- Haser, L., 1957, *Bull. Acad. R. Belg.*, **43**, 740.
- Herter, T., Campins, H. & Gull, G.E., 1987, *Astron. Astrophys.*, **187**, 629.
- Hills, J.G., 1981, *Astr. J.*, **86**, 1730.
- Huebner, W.F., Boice, D.C. & Sharp, C.M., 1987, *Astrophys. J. Lett.*, **320**,

L149.

Ip, W.-H. & Axford, W.I., 1982, in *Comets*, ed. Wilkening, L., University Arizona Press, Tucson, 558.

Jockers, K. & Lüst, Rh., 1973, *Astron. Astrophys.*, **26**, 113.

Jockers, K., 1985, *Astron. Astrophys. Suppl. Ser.*, **62**, 791.

Kamoun, P.G., Campbell, D.B., Ostro, S.J., Pettengill, G.H. & Shapiro, I.I., 1982, *Science*, **216**, 293.

Keller, H.U. & Meier, R.R., 1976, *Astron. Astrophys.*, **52**, 273.

Keller, H.U., Arpigny, C., Barbieri, C., Bonnet, R.M., Cazes, S., Coradini, M., Cosmovici, C.B., Delamere, W.A., Huebner, W.F., Hughes, D.W., Jamar, C., Malaise, D., Reitsema, H.J., Schmidt, W.K.H., Seige, P., Whipple, F.L. & Wilhelm, K., 1986, *Nature*, **321**, 320.

Kissel, J., Brownlee, D.E., Büchler, K., Clark, B.C., Fechtig, H., Grün, E., Hornung, K., Igenbergs, E.B., Jessberger, E.K., Krueger, F.R., Kuczera, H., McDonnell, J.A.M., Morfill, G.M., Rahe, J., Schwehm, G.H., Sekanina, Z., Utterback, N.G., Völk, H.J. & Zook, H.A., 1986, *Nature*, **321**, 336.

Knacke, R.F., Brooke, T.Y. & Joyce, R.R., 1987, *Astron. Astrophys.*, **187**, 625.

Korth, A., Marconi, M.L., Mendis, D.A., Krueger, F.R., Richter, A.K., Lin, R.P., Mitchell, D.L., Anderson, K.A., Carlson, C.W., Rème, H., Sauvaud, J.A. & d'Uston, C., 1989, *Nature*, **337**, 53.

- Lamy, P.L., Pederson, H. & Vio, R., 1987, *Astron. Astrophys.*, **187**, 661.
- Lang, B., 1987, *ESA SP-278*, 483.
- Langevin, Y., Kissel, J., Bertaux, J-L. & Chassefière, E., 1987, *Astron. Astrophys.*, **187**, 761.
- Marsden, B.G., Sekanina, Z. & Yeomans, D.K., 1973, *Astron. J.*, **78**, 211.
- Marsden, B.G., & Roemer, E., 1982, in *Comets*, ed. Wilkening, L., University Arizona Press, Tucson, 707.
- McCrea, W.M., 1975, *Observatory*, **95**, 239.
- McDonnell, J.A.M., Kissel, J., Grün, E., Grard, R.J.L., Langevin, Y., Olearczyk, R.E., Perry, C.H. & Zarnecki, J.C., 1986, *ESA SP-250*, **II**, 25.
- Mendis, D.A., 1973, *Astrophys. Sp. Sci.*, **20**, 165.
- Mendis, D.A., Houppis, H.L.F. & Marconi, M.L., 1985, *Fundam. Cosmic Phys.*, **10**, 1.
- Millis, R.L., A'Hearn, M.F. & Campins, H., 1988, *Astrophys. J.*, **324**, 1194.
- Napier, W.M., 1985, in *Dynamics of comets: Their Origin and Evolution*, *IAU Coll. No.89*, 31.
- Niedner Jr., M.B. & Brandt, J.C., 1978, *Astrophys. J.*, **223**, 655.
- O'Dell, C.R., Robinson, R.R., Krishna Swamy, K.S., McCarthy, P.J & Spinrad, H., 1988, *Astrophys. J.*, **334**, 476.
- Olsson-Steel, D., 1988, *Mon. Not. R. astr. Soc.*, **234**, 389.
- Oort, J., 1950, *Bull. Astron. Inst. Neth.*, **11**, 91.

- Öpik, E.J., 1975, *Irish Astr. J.*, **12**, 1.
- Rees, D., Meredith, N.P. & Wallis, M.K., 1986, *ESA SP-250*, **I**, 493.
- Reeves, H., 1974, *Nature*, **248**, 398.
- Richter, K., & Keller, H.U., 1987, *Astron. Astrophys.*, **171**, 317.
- Rickmann, H., Kamél, L., Festou, M.C. & Froeschlé, C., 1987, *ESA SP-278*, 471.
- Russel, C.T., Saunders, M.A., Phillips, J.L. & Fedder, J.A., 1986, *J. Geophys. Res.*, **91**, 1417.
- Safronov, V.S., 1977, in *Comets, Asteroids, Meteorites, IAU Coll. No.39*, 483.
- Sekanina, Z. & Larson, S.M., 1984, *Astron. J.*, **89**, 1408.
- Shul'man, L.M., 1972, in *The Motion, Evolution of Orbits and Origin of Comets, IAU Symp.12*, 271.
- Smirnov, V., Vaisberg, O.L. & Anisimov, S., 1986, *Astron. Astrophys.*, **187**, 774.
- Spinrad, H., Stauffer, J. & Newburn Jr., R.L., 1979, *Publ. Astron. Soc. Pacific*, **91**, 707.
- Spinrad, H., 1987, *Ann. Rev. Astron. Astrophys.*, **25**, 231.
- Tokunga, A.T., Nagata, T. & Smith, R.G., 1987 *Astron. Astrophys.*, **187**, 519.
- Vaisberg, O., Smirnov, V. & Omelchenko, A., 1986, *ESA SP-250*, **II**, 17.

Wallis, M.K. & Wickramasinghe, N.C., 495, *ESA SP-278*, 495.

Whipple, F.L., 1950, *Astropys. J.*, 111, 375.

Whipple, F.L., 1982, in *Comets*, ed. Wilkening, L., University Arizona Press, Tucson, 227.

Wickramasinghe, N.C., Wallis, M.K. & Hoyle, F., 1988, preprint.

Chapter II

PHOTOMETRY OF HALLEY AND OH RESULTS

II.1 INTRODUCTION

As discussed in Chapter I, the majority of cometary observations are obtained in the visible part of the spectrum. As part of the CHUKCC campaign to observe Comet Halley, narrowband photometry was performed by the author both pre- and post-perihelion. This chapter begins by discussing the techniques needed in cometary photometry and the filters used in section II.2. Section II.3 outlines the actual observations, while section II.4 summarises the reduction procedures used to acquire absolute magnitudes and fluxes. To interpret the OH results, the well-known Haser Model is described in section

II.5, the actual analysis being presented in section II.6.

II.2 COMETARY PHOTOMETRY

Photometry of stars may readily yield errors of < 0.01 magnitudes. But photometric observations of comets involve additional sources of error. Perhaps the most important is that of sky subtraction. Bright comets such as Halley can possess comae several tens of arc-minutes across. This means that any chance of simultaneous measurement of sky and comet is not usually possible, as most dual-channel photometers have aperture separations of one or two arc-minutes. Measurements of sky brightness must be made at a point well away from the nucleus to avoid contamination by the coma, and these measurements have to be interspersed with cometary observations.

Comets generally tend to be observed at small elongations from the sun i.e. at large airmasses X . This can make the corrections for atmospheric extinction extremely difficult. By using a polynomial involving $\sec z$, where z is the zenith angle, one can achieve accurate results down to airmasses of 8 or more in the visible region of the spectrum (A'Hearn, 1983). However, even at relatively low airmasses any observations taken in the near UV will suffer large extinctions that behave non-linearly with airmass (see section II.4)

Although many observations of comets have been taken in the standard UVB system used in stellar work, these filters are not diagnostic of the physical conditions at the comet. Meaningful data must be obtained with

Name	λ_0 Å	$\Delta\lambda$ (FWHM) Å	Molecular Transition	Possible Contamination
OH	3078	75	$A^2\Sigma^+ \rightarrow X^2\Pi$	
BC	3649	88	-	
CN	3869	40	$B^2\Sigma^+ \rightarrow X^2\Sigma^+$	
C ₃	4055	71	$\tilde{A}^1\Pi \rightarrow \tilde{X}^1\Sigma^+$	
CO ⁺	4260	65	$A^2\Pi \rightarrow X^2\Sigma^+$	
VC	4852	62	-	C ₂
C ₂	5141	80	$d^3H \rightarrow a^3\Pi$	
RC	6840	88	-	
H ₂ O ⁺	7000	125	$\tilde{A}^2A \rightarrow \tilde{X}^2B$	NH ₂

Table II.1: IHW narrow-band filter specifications.

narrow band filters, covering wavelengths conjugate with molecular emission bands or isolating the dust continuum. In 1982 the IAU commissioned the construction of a standard set of cometary filters, in time for the work of the IHW. There are six filters commonly used, isolating the emission bands of OH, CN, C₃, CO⁺, C₂ and H₂O⁺. A NH filter at $\lambda = 3365\text{Å}$ is not shown as this was not used in this work. At various wavelengths in between are three continuum filters for measuring the scattered solar radiation from the dust particles present. These are labelled BC, VC and RC for blue, visual and red continuum respectively. The specifications of each filter, as determined from the transmission curves, are given in table II.1. Also listed in this table are possible sources of contamination.

II.3 OBSERVATIONS

All the photometric data presented in this work was gathered during the 1985/86 apparition of Halley's Comet. The dates of observation are presented in table II.2. A description of each observing run follows:

a) December 1985. The observations were performed on the 1-m Jacobus Kapteyn Telescope at the Roque de los Muchachos Observatory on the Island of La Palma. The observers were the author together with Professor I.P. Williams of Queen Mary College, London University and Dr. P.J. Andrews of the Royal Greenwich Observatory. The instrument used was the People's Photometer, a conventional dual-channel photometer. A full description of this instrument may be found in the article by Laing and Jones (1985). Each channel of the photometer can hold 5 filters, thus allowing all 9 IHW filters to be used at once. The tenth channel was fitted with a standard Johnson 'B' filter, to ensure that saturation of the photomultiplier would not occur.

Measurements were taken simultaneously in both channels, consisting of 10 1-second integrations on the object of interest. These were then averaged by the software running the system and the measurements written to a computer file. The next filter was then automatically positioned in the light path and the next measurement taken. When the entire filter sequence had been run through, the telescope was repositioned. At the end of the night, a hard copy of the data file was obtained as a backup.

Date	α (1950.0)	δ	Δ (AU)	$\dot{\Delta}$ (km s ⁻¹)	r_h (AU)	\dot{r}_h (km s ⁻¹)
Dec 8.0	0h 1.165m	+8° 4.17'	0.70	24.75	1.38	-26.43
Dec 9.0	23h 53.599m	+7° 20.93'	0.72	26.22	1.36	-26.48
Dec 10.0	23h 46.421m	+6° 39.34'	0.73	27.55	1.35	-26.52
May 7.0	10h 39.761m	-13° 59.57'	0.99	54.45	1.72	+25.21
May 8.0	10h 38.007m	-13° 25.70'	1.02	54.81	1.74	+25.15
May 10.0	10h 34.961m	-12° 24.25'	1.08	55.41	1.76	+25.04
May 12.0	10h 32.445m	-11° 30.16'	1.15	55.89	1.79	+24.93
May 13.0	10h 31.360m	-13° 5.55'	1.18	56.09	1.81	+24.87

Table II.2: Celestial, geocentric and heliocentric positions for Comet Halley on the nights of observation

The cometary data was gathered in two main modes:

1: Aperture photometry of the comet, with the telescope centered on the nucleus. This gave information on the production of gas and dust within the inner coma. Apertures used were of diameter 14", 28", 41", 63", 84", 110" and 138".

2: Stepping of the telescope equal distances radially outwards from the nucleus to create a low resolution but high signal-to-noise scan of the density distribution in the coma. Measurements were taken in the 63" aperture every 5' from the nucleus at all four compass points out to 30', on December 7/8th and December 8/9th. On December 8/9th and 9/10th the 41" aperture was used to map fluxes North, South, East and West in 59" increments

The two apertures in the photometer are placed 177" apart in a North -

South orientation as seen on the sky. To obtain measurements of a particular position through all filters, the telescope had to be moved this distance and the measurement repeated, thereby creating a set of extra readings $177''$ either side of the point of interest. As noted in section II.2, sky brightness measurements must be taken outside the maximum extent of the coma. On each night therefore, the sky was measured in an objectless field (found by use of the television monitor) some 3° North of the nucleus. During all observations of the comet, the telescope was slewing at a rate and in a direction equal to the apparent motion of the comet.

A problem occurred on the night of 9/10th December. When the telescope was pointed at various regions of blank sky, it was found that the sky readings were a strong function of position of the telescope. It was consequently found that a small red light in the telescope dome had been shining into a viewing eyepiece used for centering the apertures on objects. Inspection of the standard star readings showed that measurements taken in the C_2 , RC and H_2O^+ filters were affected and could not be used.

b) March 1986. The data was gathered at the South African Astronomical Observatory, using the 20-inch telescope situated at Sutherland, Cape Province. The single observer on this run was Dr. P.J. Andrews of the Royal Greenwich Observatory. The instrument used was a modular single channel photometer with 10 filter positions. As this telescope does not possess the

facility for off-set guiding, only aperture photometry was performed. The position of the nucleus was centered in the aperture before each measurement was taken. This data was particularly important as it was obtained during the period of the spacecraft encounters. Because of the low altitude of the site, the OH filter was not used during this run.

c) May 1986. These observations were again performed on the 1-m JKT on La Palma. The observers were the author together with Professor I.P.Williams and Mrs G.P.Williams of Queen Mary College, London University. The modus-operandi was very similar to the observing techniques established during the first run, but with one important difference. A beam splitter was placed in the light path of the photometer between the aperture and the filter slides, allowing simultaneous measurements in both channels of the same point in the sky. Unfortunately the use of the beam-splitter resulted in two undesired side effects. The first was a reduction in sensitivity due to the bifurcation of the beam and absorption in the glass. The second and perhaps more serious effect of the prism was the strong absorption in the blue region of the spectrum. No counts were received unless pointing at the nucleus of Halley or at a star. A subsequent analysis of the standard star measurements in the OH filter showed that the data at this wavelength was of unusable quality.

The observing schedule was very similar to that in December 1985, except

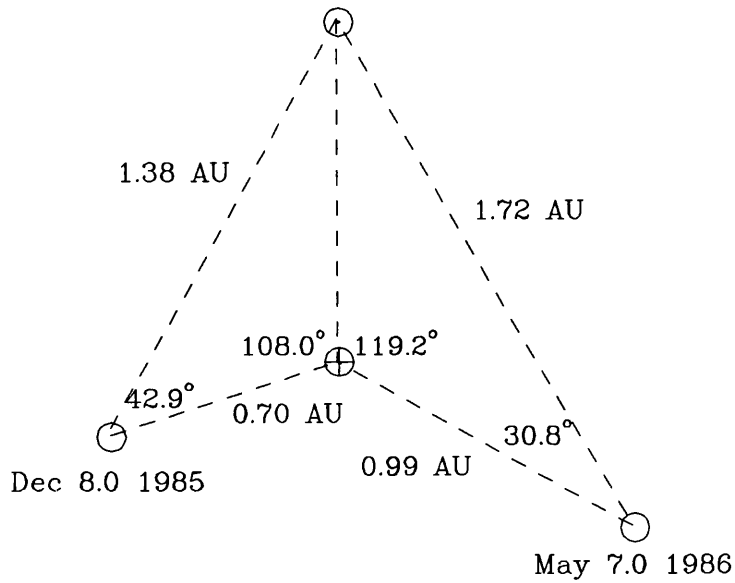


Figure II.1: Relative positions of the Earth, Sun and Halley during the La Palma observations.

that the 41" aperture was used for both the long-range scans stepping every 5' and the short range scans stepping every 60". Also the photocenter of the coma was observed more frequently than in December, in the hope of detecting the recently discovered 2.2 day rotation period of the nucleus.

Figure II.1 shows the relative positions of the Earth and Halley during the La Palma observations. The coma positions observed in all filters both pre- and post-perihelion from La Palma are shown diagrammatically in figure II.2.

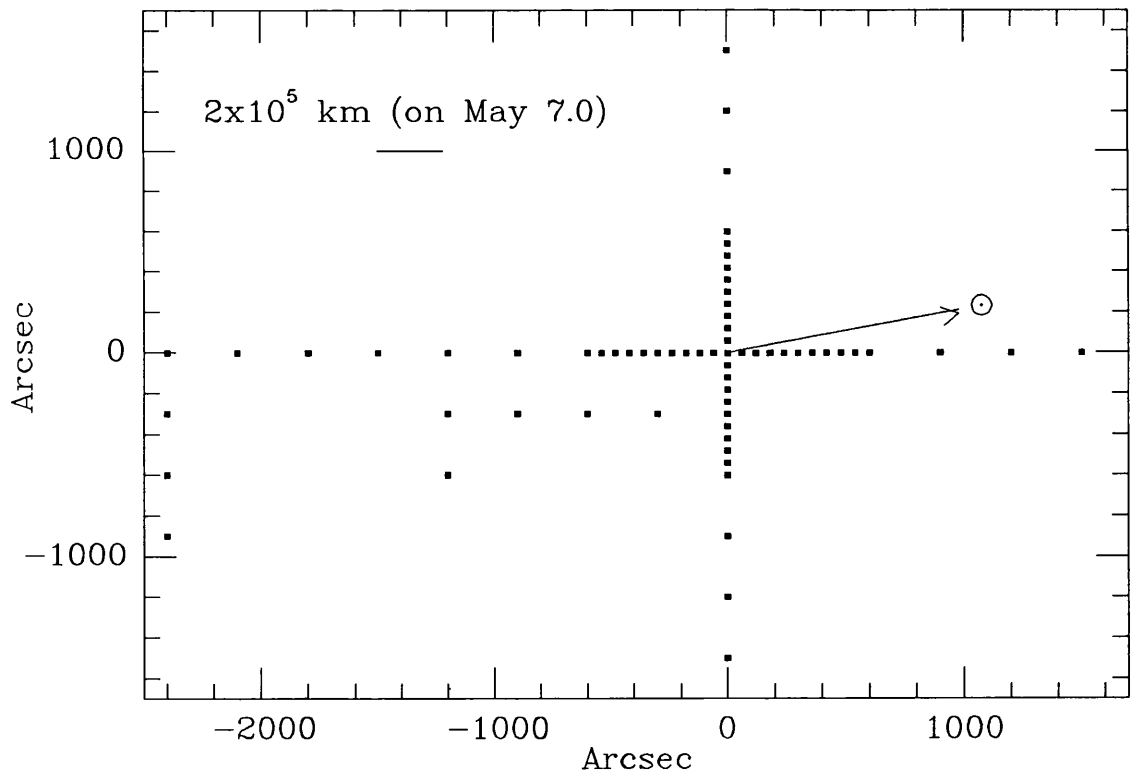
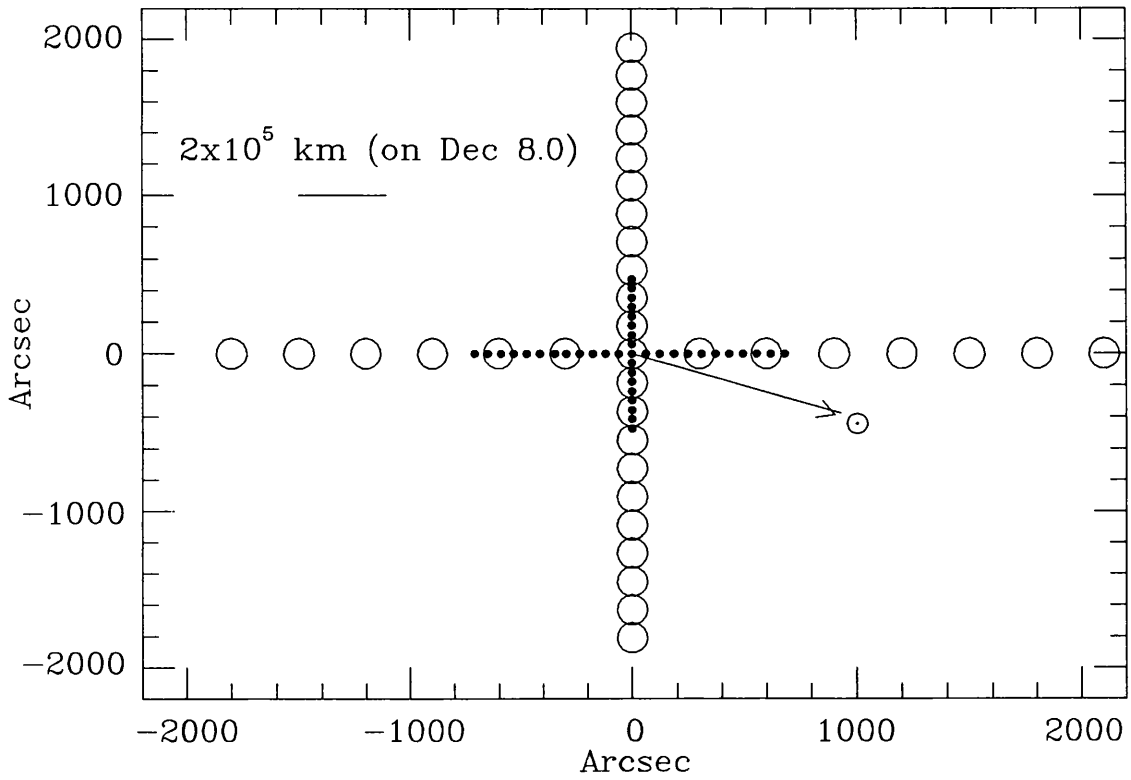


Figure II.2: Positions of coma measurements during the La Palma observing runs. Points indicate fluxes measured through the 41" aperture, circles are measurements made with the 62" aperture.

II.4 REDUCTION

For all the data, the sky counts were interpolated by hand over the observing period and subtracted from the source counts. The atmospheric extinction corrections were derived in the usual manner from the standard star observations for all wavelengths except 3085Å. A problem arises here due to the finite width of the filter and the steep dependence of extinction on wavelength in the near Ultraviolet. This results in the extinction averaged over the filter being a function of the colour of the source. The colour will be a function of airmass, leading to a non-linear variation of magnitude with airmass. A'Hearn (1985) has modelled this variation and accounted for it by giving polynomial expressions for an effective airmass X_{eff} that is dependent on X and the colour of the object i.e. a comet, a G-type or B-type star. Using this proxy, airmass extinction coefficients can be found for both stars and comets. The extinction coefficients for all filters on each observing night are listed in Table II.3.

Comparison with the theoretical values obtained by King (1985) for La Palma show that on several nights above average extinction was present due to the presence of dust in the atmosphere. It should be noted here that U.Carsenty (private communication) has found a red-leak in the OH filter, which when looking at G-type stars will be responsible for $\simeq 50\%$ of the flux at an airmass of 2.5. However, only the B-type standard stars were used

Date	OH	BC	CN	C ₃	CO ⁺	VC	C ₂	RC	H ₂ O ⁺
7/12/85	1.56	0.51	0.41	0.35	0.37	0.21	0.22	0.14	0.17
8/12/85	1.55	0.43	0.34	0.27	0.22	0.14	0.12	0.06	0.07
9/12/85	1.47	0.46	0.36	0.30	0.27	0.15	–	–	–
13/3/86	–	0.49	0.39	0.32	0.25	0.17	0.14	0.07	0.06
14/3/86	–	0.51	0.39	0.33	0.27	0.17	0.14	0.07	0.06
15/3/86	–	0.50	0.40	0.34	0.27	0.18	0.14	0.08	0.06
17/3/86	–	0.54	0.44	0.36	0.28	0.20	0.16	0.10	0.06
18/3/86	–	0.51	0.41	0.35	0.27	0.18	0.15	0.10	0.06
7/5/86	–	0.43	0.34	0.31	0.23	0.18	0.15	0.08	0.06
8/5/86	–	0.67	0.52	0.44	0.37	0.35	0.34	0.20	0.18
10/5/86	–	0.48	0.39	0.34	0.26	0.18	0.17	0.08	0.07
12/5/86	–	0.71	0.66	0.59	0.55	0.44	0.42	0.31	0.31
14/5/86	–	0.61	0.54	0.48	0.45	0.35	0.33	0.23	0.24

Table II.3: Extinction in magnitudes per airmass for all photometric observations

for the flux calibration, which would reduce contamination even at large airmasses. Observations of the comet itself should not be affected due to the high intensity of the OH emission compared to the reflected solar-type continuum.

With the gas filters one is interested in the luminosity due to molecular emission alone, without contamination due to the underlying dust continuum. To calculate this, the observations of the G-type solar standards were used to calculate transformation equations to solar colours in the dust filters. These can then be used to calculate the magnitude $M(dust)$ due to the dust alone at any particular wavelength by extrapolation/interpolation from the

magnitudes at the continuum wavelengths. The gas luminosity is then found simply by

$$L_{gas} = F_{\lambda} (10^{-0.4M(gas)} - 10^{-0.4M(dust)}) \quad (\text{II.1})$$

where $M(gas)$ is the observed magnitude of the cometary emission. The scaling factor F_{λ} converts the instrumental luminosity to absolute flux units. This scaling factor has generally a small dependence on temperature. Unfortunately the temperature was not recorded at the time of observation, so a default value of 5°C was assumed in all calculations.

F_{λ} is a function of the transmission curve of the filter and the profile of the emission band. As the relative intensities of the emission lines change in a band with heliocentric velocity due to the Swings effect (see below), so too will this scaling factor. This effect is non-negligible for the CN($\nu = 0$) and OH(0 – 0) bands. All magnitude and flux determinations were performed using the procedures and transformations listed in A'Hearn (1985).

Once fluxes have been established, they may be converted to column densities along the line of sight once the g -factor is known (see section I.4.1). Festou and Zucconi (1984) point out that the effective g -factor of a filter will also be dependent on the bandpass, especially if some of the constituent lines of the emission band lie in the wings of the transmission curve. This effect was taken into account in the scaling factors of the transformation equations as derived by A'Hearn (1985).

The g -factor is proportional to the solar flux at the respective wavelength, and thus can vary strongly due to Doppler shifting of the Fraunhofer lines in the solar spectrum as seen by the cometary molecules. This is seen particularly in the UV, and may come about via two causes. Firstly the heliocentric velocity of the comet will cause a change in luminosity, termed the Swings effect. Superimposed on this will be the Greenstein effect, which is caused by the internal velocity field of the coma. The variation in the g -factor of OH emission bands has been calculated for varying heliocentric distance and solar flux for OH (Schleicher and A'Hearn, 1982), CN (Zucconi and Festou, 1985) and CO⁺ (Magnani and A'Hearn, 1986) and these results have been used in this study.

The appendix contains all cometary magnitudes observed during the three observing runs.

II.5 THE HASER MODEL

The observed column densities alone do not tell us anything about the physical processes in Halley's coma. It is well known that any molecular species will gradually dissipate as one travels outwards from the nucleus, due to both conservation of flux and processes such as photoionisation and photo-dissociation. Before 1957 this process was investigated via diagrammatic means. The first person to derive an analytical expression for the column density in cometary comae was Haser (1957). He considered the fate of daughter molecules, dissociated from their parents with a half-life of τ_p , in turn dissociating with a half-life τ_d . In an expanding coma where all the molecules flow outwards from the nucleus at an average velocity v , the *in-situ* density at a distance R is given by

$$n(R) = \frac{Q}{4\pi v R^2} (e^{-R/v\tau_d} - e^{-R/v\tau_p}) \quad (\text{II.2})$$

This function must be integrated along the line of sight through the coma to obtain a column density $n(\rho)$. The final integral, for a point a projected distance ρ away from the nucleus is

$$n(\rho) = \frac{Q}{2\pi v \rho} \frac{l_d}{l_d - l_p} \int_{\rho/l_d}^{\rho/l_p} K_0(y) dy \quad (\text{II.3})$$

where $l_p = v\tau_p$, $l_d = v\tau_d$ and K_0 is the modified Bessel function of zeroth order and the second kind.

In reality a finite beamwidth is used of radius r . Then the number N of

molecules within the beam centered at a particular distance x is given by

$$N(x) = \int_{x-r}^{x+r} 2\rho \arccos \left[\frac{\rho^2 + x^2 - r^2}{2x\rho} \right] n(\rho) d\rho \quad (\text{II.4})$$

where θ is the angle subtended at the nucleus from the beam center radius to the edge of the aperture. From equation (II.3), this gives

$$N(x) = \frac{Q}{\pi v} \frac{l_d}{l_d - l_p} \int_{x-r}^{x+r} \arccos \left[\frac{\rho^2 + x^2 - r^2}{2x\rho} \right] \int_{\rho/l_d}^{\rho/l_p} K_0(y) dy d\rho \quad (\text{II.5})$$

When the beam is centered on the nucleus, the total number of molecules within the aperture becomes

$$N = \int_0^r 2\pi\sigma N(\sigma) d\sigma \quad (\text{II.6})$$

giving

$$N = \frac{Q}{v} \left[\int_{r/l_d}^{l_d/l_p} K_0(y) dy + \frac{l_d}{r} \left(1 + \frac{l_d}{l_p} \right) + K_1\left(\frac{l_d}{r}\right) + K_1\left(\frac{l_p}{r}\right) \right] \quad (\text{II.7})$$

More recent models such as the vectorial model by Festou (1981a) and Combi and Delsemme (1980) (see section II.3) indicate that Haser formulae do represent the molecular density distribution in a coma surprisingly well. Both authors conclude that the most important drawback is that of underestimating the true scallengths through ignoring the isotropic ejection of daughter molecules from parents. Although the Haser model is used in the next section it is worth pointing out other deficiencies:

1) The model is monokinetic, with no spread in velocities that is likely in a real coma.

- 2) Acceleration due to solar radiation pressure, an important effect for carbon based molecules that have high scattering factors, is ignored.
- 3) No variation in production rate of the nucleus is allowed for.
- 4) Spherical symmetry is assumed i.e. ejection of parent molecules from the night side of the nucleus as well as the day side.

The last point is perhaps not so serious, as the existence of a collisionally thick atmosphere just above the surface of the nucleus would to a large extent randomise the velocities of the gases. At a distance from the nucleus large compared to the collision zone, the molecules would appear to have a purely radial distribution. Indeed, though Halley was obviously outgassing from its sunlit hemisphere only, the Giotto Neutral Mass Spectrometer and the Vega-1 Neutral Mass Experiment recorded no effect of this in the distribution of neutral molecules in the inner coma (Krankowsky *et al.* 1986, Curtis *et al.* 1986). The data obtained by Curtis *et al.* (1986) do however show an overall asymmetry in the gas density at distances $< 10^5$ km from the nucleus.

II.6 OH ANALYSIS

II.6.1 SCALELENGTHS AND LIFETIMES

Of all the molecular species detected in the observing runs, OH is perhaps the best suited for at least an initial study by Haser Theory. This is due to the small acceleration of the molecule by radiation pressure. The total acceleration due to fluorescent scattering on a molecule of mass m_n is given by Keller and Meier (1976) as

$$b_v = \frac{h\nu}{m_n c} \frac{\pi e^2}{m_e c} f \frac{F_\odot(v)}{R_h^2} \quad (\text{II.8})$$

Comparing this with the expression for the g -factor of a molecular band (equation I.3), one gets

$$b_\lambda = \frac{h}{m_n \lambda} g_\lambda \quad (\text{II.9})$$

where λ is the wavelength of the band. The g -factor of the OH (0-0) band calculated by Schleicher and A'Hearn (1982) at $r_h = 1.36$ AU and $r'_h = -26$ km s⁻¹ is 1.89×10^{-4} photons s⁻¹ molecules⁻¹. The total acceleration due to all emission bands is 2.51×10^{-3} cm s⁻². Thus an OH molecule would only be decelerated by 20 m s⁻¹ after being ejected from the nuclear region at 1 km s⁻¹ and travelling 10⁶ km. The OH molecule should exhibit spherical symmetry in the case of purely anisotropic outflow of the parents.

Due to the high luminosity of the OH (0-0) band, the only non-negligible molecular contamination is from the OH (1-1) band at 3135Å. This contam-

ination was modelled using the g -factors for both bands given by Schleicher and A'Hearn (1982) to give relative luminosity ratios, and the extinction coefficients measured on La Palma centered at 3078\AA together with the theoretical form of the extinction curve (King, 1985). The signal from this band was calculated to be less than 1% of the total received flux at all observed air-masses, due to the narrow bandwidth of our filter. This was then accounted for in the derived OH fluxes.

Festou (1981b) calculated the lifetime of H_2O to be $8.2 \times 10^4\text{s}$ at 1 AU. This value was adopted and used to derive Q/v and $l(\text{OH})$ from the long and short-range scans. This preliminary work was presented by Fitzsimmons, Adams and Williams (1986), in which a value of $l(\text{OH}) = (1.3 \pm 0.2) \times 10^5\text{ km}$ was derived. One can see in figure 3 of this paper that the model fitted quite well the points in the outer coma, but badly underestimated the column densities in the inner coma. As one would expect the measurements nearest the nucleus to have the best signal-to-noise, a fit was attempted to the innermost observations alone again assuming Festou's value for $l(\text{H}_2\text{O})$. As seen in figure II.3, this resulted in both an underestimate of the flux in the outer coma, and a scalelength for OH shorter than that of H_2O , something ruled out by all previous investigators.

Thus it was decided to relax the constraints on the model and treat both parent and daughter scalelengths as unknowns. Feldman *et al.* (1987)

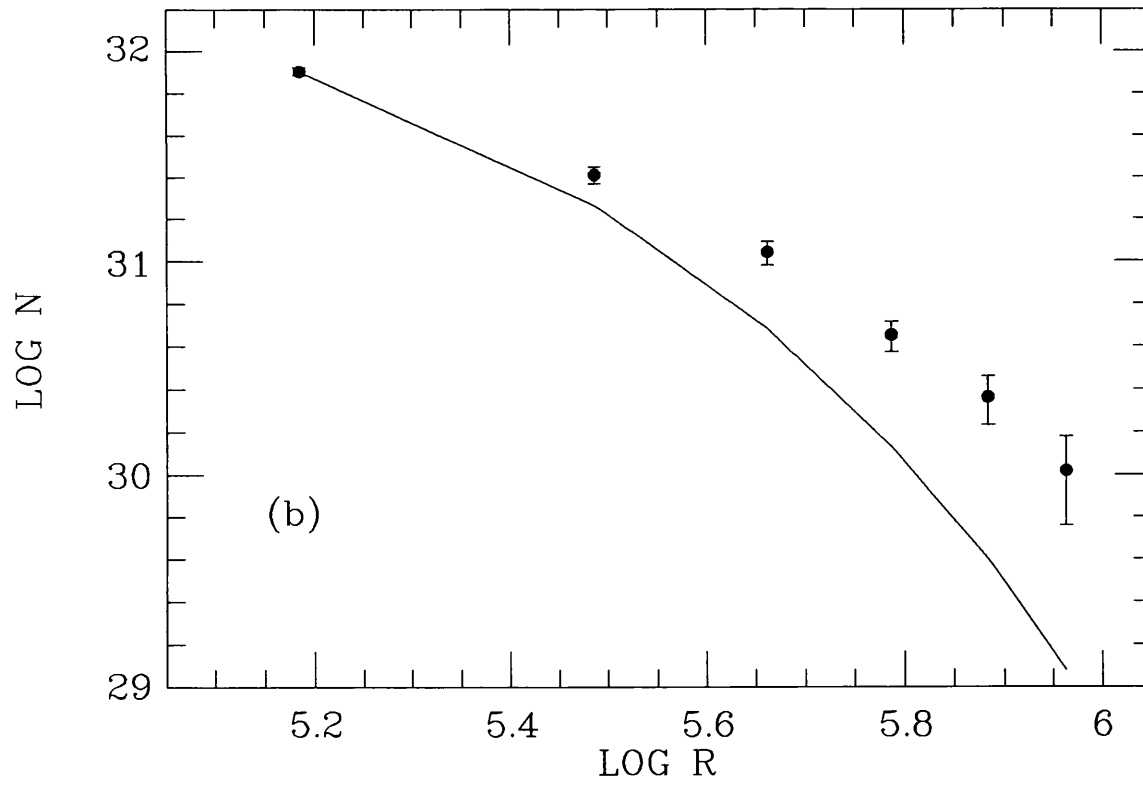
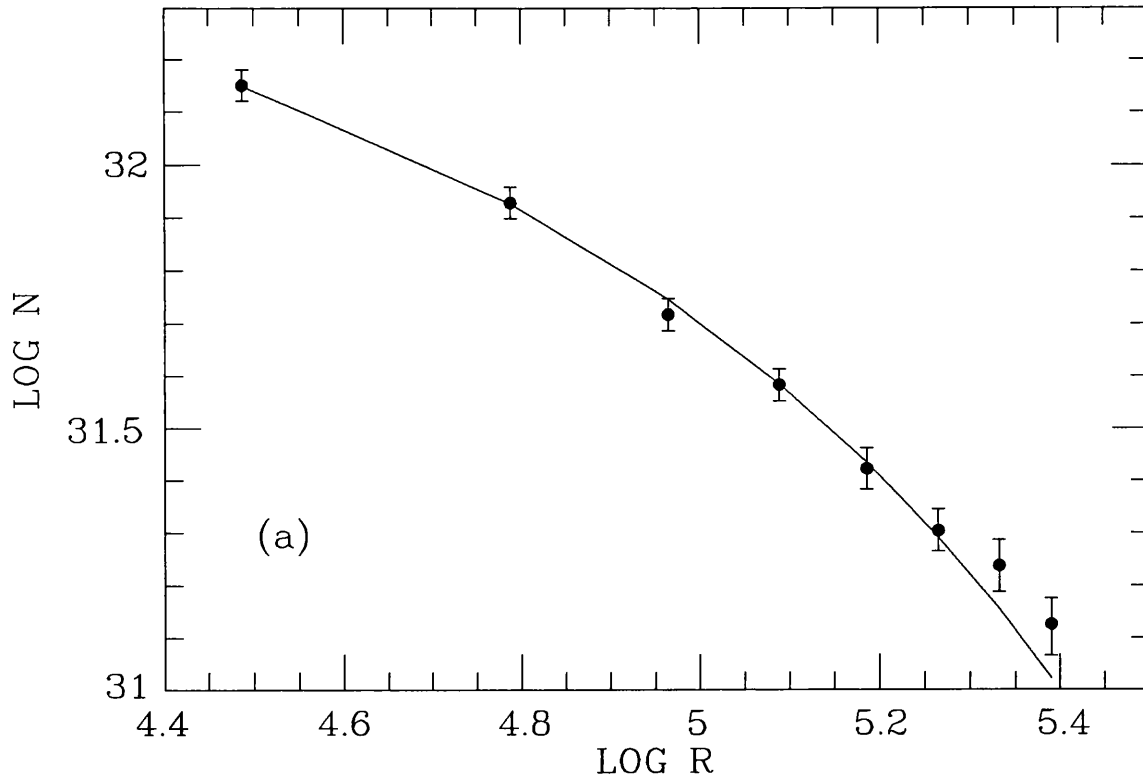


Figure II.3: Calculated Haser column densities, assuming $l(H_2O) = 8.2 \times 10^4$ km at 1 AU.

have shown that the photometric brightness of the comet, and therefore the production of gas and dust by the nucleus, was highly variable in late December on a day to day basis. So each scan was analysed in turn to give a separate estimate of the scalelengths. This was performed by generating theoretical surface brightness distributions with various parent and daughter scalelengths. The parental scalelengths were incremented by 10^3 km between calculations, whereas the daughter scalelengths were increased in 10^4 km steps. It was found that for the long-range scans, the derived column densities were relatively insensitive to changes in the parental scalelength. Thus the following procedure was performed.

The original fitting over a broad range of values was done by eye. The long-range scans were used to produce a best-estimate of the daughter scalelength. Using this value, the short-range scans were analysed to obtain a value for the parental scale-length. Going back to the long-range scans, this routine was iterated until residuals were minimised between the model and the observations. Data points with large errors (i.e. in the outer coma) were given low weight. In the data taken on December 9.9, the two innermost points have been ignored in the fitting - this is discussed in section II.6.2.

The results are given in figures II.4 and II.5. The corresponding scalelengths for the scans are listed in table II.4. When reduced to 1 AU assuming

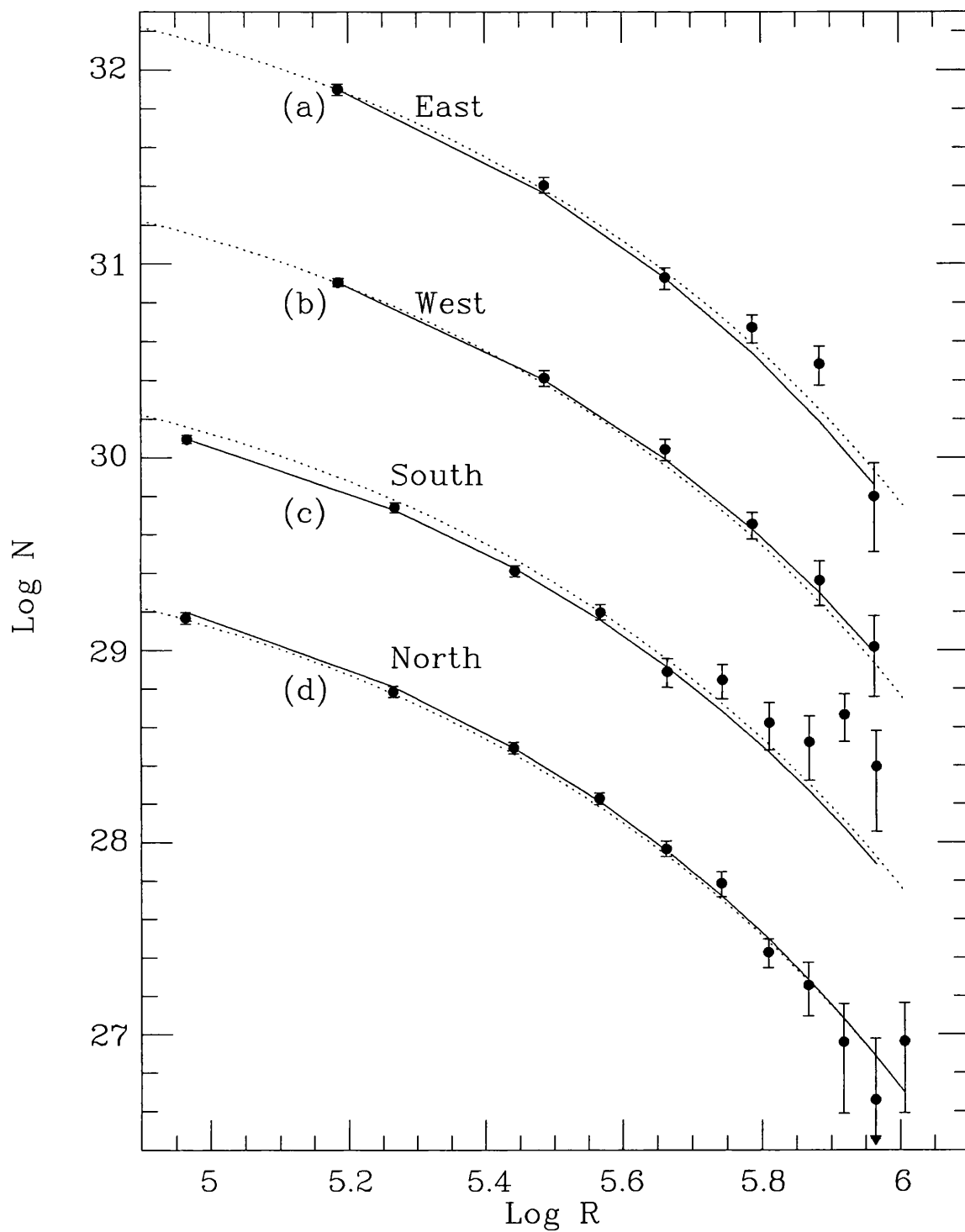


Figure II.4: Fitted Haser models to observed longrange scans. The direction of scan is shown above each curve. The dotted line shows the modelled surface brightness calculated using the mean scalelengths from all eight scans. Formal errors in reduction are shown.

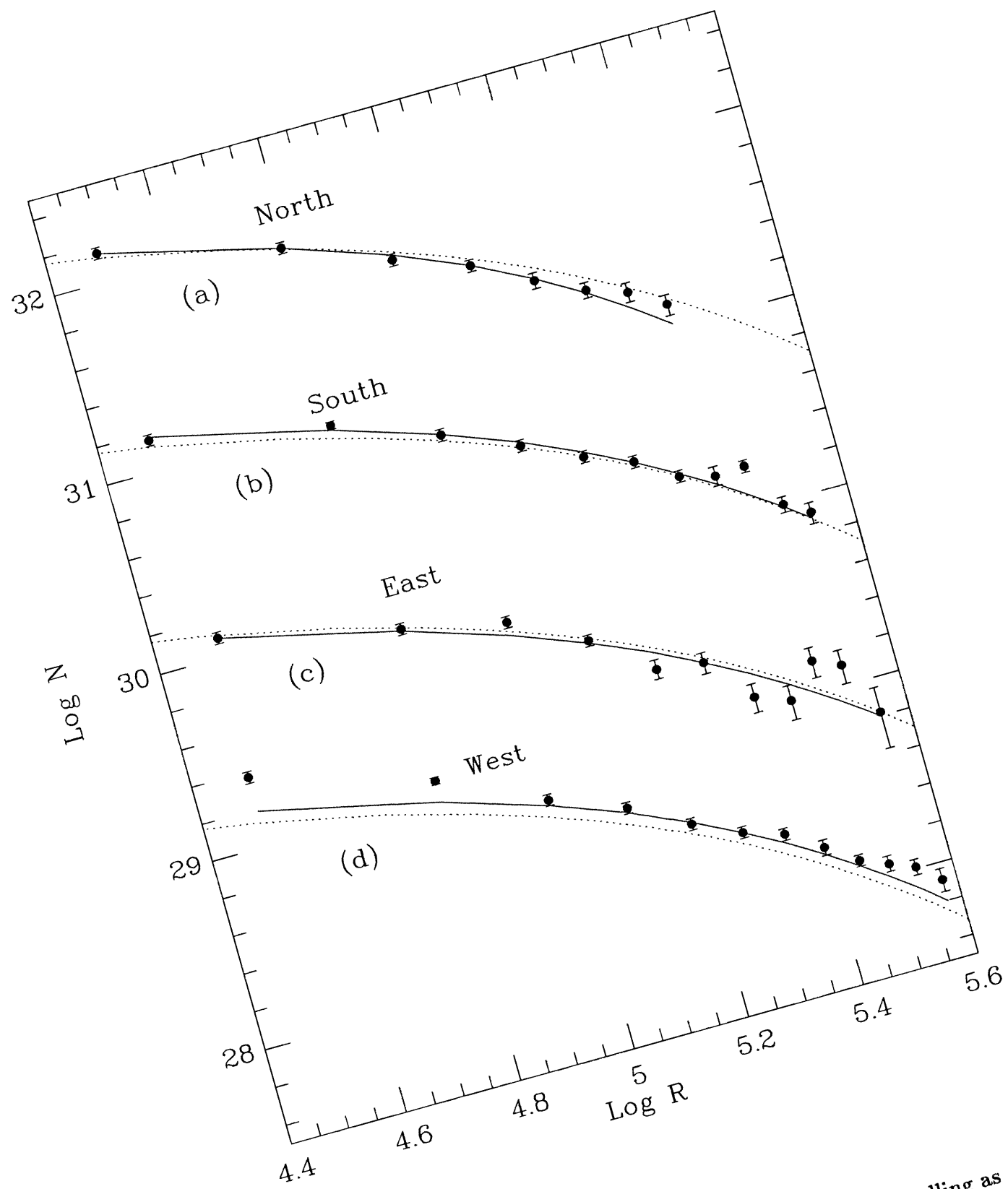


Figure II.5: Fitted Haser models to observed shortrange scans. Labelling as in figure II.4

Date	Scan Direction	$l_p(\text{H}_2\text{O})$ ($\times 10^4 \text{km}$)	$l_d(\text{OH})$ ($\times 10^5 \text{km}$)	Q_{OH} ($\times 10^{29} \text{mols s}^{-1}$)
Dec 7.90	West	4.7 ± 0.5	1.7 ± 0.1	1.4
Dec 7.94	East	4.2 ± 0.5	1.6 ± 0.1	1.4
Dec 7.98	South	4.7 ± 0.5	1.7 ± 0.1	1.3
Dec 8.88	North	4.3 ± 0.5	1.6 ± 0.1	1.3
Dec 8.93	South	3.8 ± 0.5	1.7 ± 0.1	1.2
Dec 8.97	North	3.8 ± 0.5	1.6 ± 0.1	1.1
Dec 9.00	East	4.4 ± 0.5	1.7 ± 0.1	1.3
Dec 9.84	West	4.3 ± 0.5	1.5 ± 0.1	1.2

Table II.4: Haser model parameters derived from OH coma photometry

a R_h^2 law, the Haser scalelengths are

$$l(\text{H}_2\text{O}) = (4.3 \pm 0.4) \times 10^4 \text{ km},$$

$$l(\text{OH}) = (1.6 \pm 0.1) \times 10^5 \text{ km}.$$

The Haser scalelength found for H_2O is a factor of 2 lower than commonly used in pre-1986 studies. However, Wallis *et al.* (1984) had found $l(\text{H}_2\text{O}) = (3.2 \pm 0.3) \times 10^4 \text{ km}$ at 1 AU in Comet Austin 1982g from observations from the International Ultraviolet Explorer satellite. A similar value was found for Halley by Weaver *et al.* (1986), studying this time the infra-red H_2O emission lines. The Giotto Neutral Mass Spectrometer found $l(\text{H}_2\text{O}) = (4.2 \pm 0.3) \times 10^4 \text{ km}$ (Krankowsky *et al.*, 1986). Our mean value is in excellent agreement with the Giotto measurement, although some of the individual scans indicate values closer to the remotely sensed scalelengths.

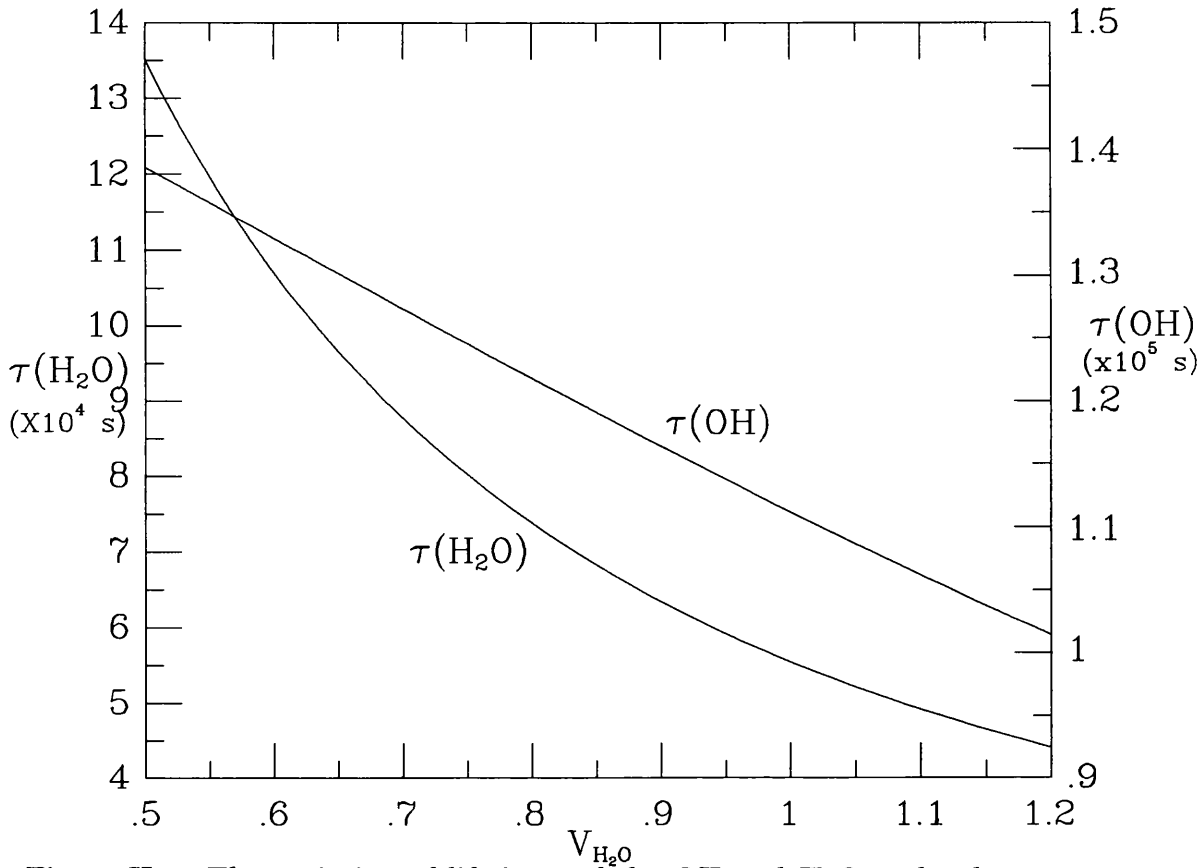


Figure II.6: The variation of lifetimes of the OH and H₂O molecules as a function of outflow velocity from the nucleus.

If one assumes a monokinetic velocity for the H₂O molecules as they leave the vicinity of the nucleus, the Average Random Walk Model (ARWM) of Combi and Delsemme (1980) can relate derived Haser scalelengths to the true photo-dissociation lifetimes of the molecules (see section III.4.2). For this calculation, a knowledge of both the parental velocity and the relative velocity of the daughter after creation is required. Festou (1981) calculates the mean dissociation velocity of OH from H₂O as 1.15 km s⁻¹, with a dispersion of just 0.11 km s⁻¹. This has been used to produce figure II.6, showing the resulting timescales for OH and H₂O as a function of the outflow velocity v_p . Using the lifetime for H₂O at 1 AU deduced from Giotto (5.5×10^4 s),

this leads to an outflow velocity at the comet of $1.0 \pm 0.1 \text{ km s}^{-1}$, and a lifetime for OH at 1 AU of $(1.1 \pm 0.1) \times 10^5$ seconds. The dissociation of OH has been theoretically studied by van Dishoeck and Dalgarno (1984), who found the theoretical lifetimes for the molecule over a large range of heliocentric velocity and solar luminosity. For $\dot{R}_h \simeq -26 \text{ km s}^{-1}$, they find $\tau(OH) = (1.4 \pm 0.3) \times 10^5$ seconds at solar minimum. The value deduced from our observations above is consistent with this.

II.6.2 PRODUCTION AT NUCLEUS

Once the Haser scalelengths have been calculated, simple scaling of the theoretical curves gives the value of Q/v at the nucleus. As v is found above, the production rates come out directly and are given for each scan in Table II.4. Coupled with these we have the number densities derived from our aperture photometry, reduced to production rates using our scalelengths in Haser formula II.6. An initial inspection of these implied that only those measurements taken at airmasses of $X < 1.25$ were of sufficient quality. This implies that the OH extinction still not entirely corrected for, a fact suspected previously (I.P.Williams, private communication). The resulting values are shown in Table II.5.

Two points worth noting are, firstly, that the production rates derived are close but not equal to those calculated from the scans (see table II.4). Second,

Date	Airmass	Aperture Diameter (arcsec)	OH Flux (0-0) band (ergs cm ⁻² s ⁻¹)	Q _{OH} (x10 ²⁹ mols s ⁻¹)
Dec 7.859	1.074	62	(5.07 ± 0.15)x10 ⁻¹⁰	1.88±0.06
Dec 8.865	1.094	62	(5.31 ± 0.32)x10 ⁻¹⁰	1.90±0.12
Dec 8.920	1.244	41	(2.66 ± 0.17)x10 ⁻¹⁰	1.90±0.12
Dec 9.888	1.163	41	(3.71 ± 0.19)x10 ⁻¹⁰	2.57±0.13
Dec 9.891	1.172	62	(7.14 ± 0.29)x10 ⁻¹⁰	2.49±0.10

Table II.5: Hydroxyl production rates derived from aperture photometry

there is an modest increase in the production of OH of $\simeq 33\%$ on the night of 9/10th December. It should be remembered that the Haser model assumes a constant production rate, so that the actual increase may well differ from this value. This is the cause of the discrepancy between the innermost points of the scan that night and the model, as shown in figure II.5(d). Assuming an outflow velocity of $\simeq 1 \text{ km s}^{-1}$, this implies the outburst started $\simeq 17$ hours beforehand, on December 9.2. This is confirmed by our aperture photometry obtained on December 9.00, which shows no sign of increased activity in the near nuclear region. The lack of a significant number of data points prevents the search for any periodicity in the OH production rate.

Previous studies of OH in the radio domain, at 1665 and 1667Mhz, have detected anisotropic emission from cometary nuclei. Bockl e-Morvan and Gerard (1984) have deduced anisotropic emission ratios of between 18% and 67% for comets studied by them. More recently de Pater *et al.*(1986) have produced high resolution maps of the inner coma of Halley showing a highly

irregular distribution of OH. However, as the inferred velocity of these regions is very low ($< 6 \text{ m s}^{-1}$), there is some doubt as to whether these are really areas of high OH concentration, or rather that the excitation of the OH maser varies within the coma.

Our data for figures II.5(a,b & c) were all obtained within 100 minutes of each other, and the points nearest the nucleus do indeed show differing values. The flux East of the comet is 6% less than that to the North, and 9% less than that to the South. Unfortunately we do not have data to the West taken on that night, where outgassing would be greatest due to solar irradiation of the nucleus. However, when looking at this data the Greenstein effect must also be taken into account. From Schleicher and A'Hearn (1982) the variation of the g -factor of the OH molecules could be as high as 12%. Thus although the data does show increased flux with the expected tendency, the cause of this is doubtful.

An highly important parameter in comets is the dust to gas ratio in the inner coma, and it may be estimated as follows. With our production rate, the mass of H_2O creating OH is $3.9 \times 10^6 \text{ g s}^{-1}$. Festou has calculated that $\simeq 80\%$ of H_2O dissociates into OH. This amount may be incorrect however, as the same analysis gave the wrong lifetime for H_2O . In the absence of any improved model we use this figure here, albeit assuming a possible error of $\pm 20\%$. The production rate of dust at this epoch has been calculated by

Tokunga *et al.* (1986) to be $2 \times 10^6 \text{ g s}^{-1}$. This then results in a dust to water ratio by mass of 0.4 ± 0.1 . This is a factor of $\simeq 2$ above that derived from in-situ measurements by Giotto (McDonnell *et al.*, 1986) but similar to the value derived by Tokunga *et al.* from theoretical considerations of the dust-gas interaction near the nucleus. It must be recognised that the Tokunga result uses assumed average properties of dust grains such as size and albedo, so that the derived dust/gas mass ratio of 0.3 ± 0.1 (assuming $n(\text{CO})/n(\text{H}_2\text{O})=0.2$) may be significantly in error. The primary hypothesis though, that a cometary nucleus is mostly water ice, is upheld.

II.7 REFERENCES

- A'Hearn, M.F., 1983, in *Solar System Photometry Handbook*, ed Genet, R.M., Willmann-Bell, 3-1.
- A'Hearn, M.F., *IHW Photometry & Polarimetry Net Newsletter*, 30th August 1985.
- A'Hearn, M.F., *IHW Photometry & Polarimetry Net Newsletter*, 3rd February 1986.
- Bocklée-Morvan, D. & Gerard, E., 1984, *Astron. Astrophys.*, **131**, 111.
- Combi, M.R. & Delsemme, A.H., 1980, *Astrophys. J.*, **237**, 633.
- Curtis, C.C., Fan, C.Y., Hsieh, K.C., Hunten, D.M., Ip, W.-H., Keppler, E., Richter, A.K., Umlauf, G., Afonin, V.V., Dyachkov, A.V., Erö Jr., J. & Somogyi, A.J., 1986, *20th ESLAB Symp., ESA SP-250*, I, 391.
- de Pater, I., Palmer, P. & Snyder, L.E., 1986, *Astrophys. J. Lett*, **304**, L33.
- Feldman, P.D., Festou, M.C., A'Hearn, M.F., Arpigny, C., Butterworth, C.S., Cosmovici, C.B., Danks, A.C., Gilmozzi, R., Jackson, W.M., McFadden, L.A., Patriarchi, P., Schleicher, D.G., Tozzi, G.P., Wallis, M.K., Weaver, H.A. & Woods, T.N., 1987, *Astron. Astrophys.*, **187**, 325.
- Festou, M.C., 1981a, *Astron. Astrophys.*, **96**, 52.
- Festou, M.C., 1981b, *Astron. Astrophys.*, **96**, 69.
- Festou, M.C. & Zucconi, J.M., 1985, *Astron. Astrophys.*, **134**, L4.
- Fitzsimmons, A., Adams, D.J & Williams, I.P., 1986, *20th ESLAB Symp.*,

ESA SP-250, III, 63.

Haser, L., 1957, *Bull. Acad. R. Belg.*, **43**, 740.

Keller, H.U., & Meier, R.R., 1976, *Astron. Astrophys.*, **52**, 273.

King, D.L., 1985, *RGO/La Palma Technical Note No.31*.

Krankowsky, D., Lämmerzahl, P., Herrewerth, I., Woweries, J., Eberhardt,

P., Dolder, U., Herrmann, U., Schulte, W., Berthelier, J.J., Illiano, J.M.,

Hodges, R.R. & Hoffmaa, J.H., 1986, *Nature*, **321**, 326.

Laing, R. & Jones, D., 1985, *Vistas Astron.*, **28**, 483.

Magnani, L. & A'Hearn, M.F., 1986, *Astrophys. J.*, **302**, 477.

McDonnel, J.A.M., Kissel, J., Grün, E., Grard, R.J.L., Langevin, Y.,

Olearczyk, R.E., Perry, C.H. & Zarnecki, J.C., 1986, *20th ESLAB Symp.*,

ESA SP-250, II, 25.

Schleicher, D.G. & A'Hearn, M.F., 1982, *Astrophys. J.*, **258**, 864.

Tokunga, A.T., Golisch, W.F., Griep, D.M., Kaminski, C.D. & Hanner,

M.S., 1986, *Astron. J.*, **92**, 1183.

van Dishoeck, E.F. & Dalgarno, A., 1984, *Icarus*, **59**, 305.

Wallis, M.K., Carey, W.C., Hughes, D.W. & Burton, W.M., 1984, *Proc.*

4th European IUE Conf., *ESA SP-218*, 459.

Weaver, H.A., Mumma, M.J., Larson, H.P. & Davis, D.S., 1986, *Nature*,

324, 441.

Zucconi, J.M. & Festou, M.C., 1985, *Astron. Astrophys.*, **150**, 180.

Chapter III

ANALYSIS OF CARBON-BASED MOLECULES

III.1 INTRODUCTION

Absolute column densities for the molecular species CN, C₂ and C₃ have been evaluated from the observations described in chapter II. The measurements centred on the nucleus can be used to derive parent production rates and abundance ratios via the Haser model. This in turn provides information on the variability of outgassing. These results are given in sections III.2 and III.3. To analyse the photometric scans of the coma, a model based on that

Date	<i>g</i> -factor (photons s ⁻¹)		
	CN	C ₂	C ₃
Dec 8.0	0.036	0.061	0.107
Dec 9.0	0.038	0.063	0.110
Dec 10.0	0.038	0.034	0.112
March 13.1	0.092	0.147	0.258
March 14.1	0.089	0.142	0.250
March 15.1	0.086	0.137	0.242
March 17.1	0.081	0.129	0.227
March 18.1	0.079	0.125	0.220
May 7.0	0.024	0.039	0.069
May 8.0	0.024	0.038	0.068
May 10.0	0.023	0.037	0.065
May 12.0	0.022	0.036	0.064
May 14.0	0.022	0.035	0.062

Table III.1: Molecular *g*-factors on the dates of observation.

III.2 MOLECULAR PRODUCTION

RATIOS.

The parents of the carbon based molecules CN, C₂ and C₃ typically have number densities $\simeq 10^{-2}$ that of H₂O in cometary comae, but these species dominate the optical spectrum of a comet because of their large *g*-factors (see section I.4). The *g*-factors for these trace elements are presented in Table III.1. The *g*-factors for C₂ and C₃ were calculated from A'Hearn *et al.* (1985). The *g*-factor for CN, like that of OH, has a strong dependence on heliocentric velocity, and the value calculated most recently by Zucconi and

derived by Combi and Delsemme (1980a) was used and is described in section III.4. The results of using this model to analyse the CN and C₂ photometric scans are given in section III.5, together with a brief study of the C₃ data.

Date (March 1988)	Log(Q ₁) (Combi & Delsemme)	Log(Q ₂) (Cochran)	Log(Q ₃) (Newburn & Spinrad)
13.1	(27.30±0.03)	(27.40±0.01)	(27.60±0.02)
14.1	(27.26±0.02)	(27.35±0.02)	(27.55±0.03)
15.1	(27.37±0.04)	(27.49±0.02)	(27.67±0.01)
17.1	(27.24±0.02)	(27.36±0.02)	(27.52±0.04)
18.1	(27.30±0.06)	(27.42±0.04)	(27.58±0.04)

Table III.2: Comparison of production rates calculated from published scale-lengths. Q_1 : $l_p = 1.6 \times 10^4 R_h^2$, $l(C_2) = 1.1 \times 10^5 R_h^2$. Q_2 : $l_p = 2.5 \times 10^4 R_h^{2.5}$, $l(C_2) = 1.2 \times 10^5 R_h^2$. Q_3 : $l_p = 3.5 \times 10^4 R_h$, $l(C_2) = 1.2 \times 10^5 R_h^2$.

Festou (1985) has been used.

When one is looking at the inner coma, the simplest method of calculating production rates of molecular species is to use the Haser model described in section II.5. Although the high g -factors imply a relatively large radiation pressure on these molecules, within $\simeq 10^5$ km of the nucleus departures from spherical symmetry should be small. The determination of production rates will then depend critically on the scale-lengths and assumed outflow velocity used in the calculations. This is illustrated in Table III.2. The production rates for C₂ from the March observations through a 45-arcsec radius aperture are calculated with parent and daughter scale-lengths given by Combi and Delsemme (1986), Cochran (1985) and Newburn and Spinrad

(1984). Differences of up to 50% between the derived values are apparent.

To avoid ambiguity, the scale-lengths derived by Cochran (1985) are used from here on in this section and the next. While this may lead to inaccurate results in some comets due to differing creation processes, it has the advantage of allowing an immediate comparison of production rates. The analysis by Cochran (1987) showed that there is a well-defined correlation between abundance ratios in comets when these scale-lengths are used. For the 29 comets studied, it became apparent that a 'normal' comet is one for which $Q(C_3)/Q(CN) = 0.19 \pm 0.13$, and $Q(C_2)/Q(CN) = 1.48 \pm 0.68$.

The outflow velocities observed in Halley's coma were generally higher than those expected from the velocity dependence derived by Delsemme (1982). Thus the velocity used in each determination in this section comes from the revised expression proposed by Wyckoff *et al.* (1988) that fits the value measured in-situ by *GIOTTO* at 0.89 AU. Revising the velocity used in the Haser model leaves unaffected the production ratios.

Table III.3 contains the production rates calculated from all nights of our observing programme. The mean ratios over the whole apparition give $Q(C_3)/Q(CN) = 0.09 \pm 0.01$ and $Q(C_2)/Q(CN) = 1.57 \pm 0.20$. To derive better information on the production of gas by Halley more data is needed, so the photometric data set published by Catalano *et al.* (1986) was used. The calculation of above atmosphere fluxes by these authors followed the

Date	Δ	R_h	Log Q(CN)	Log Q(C ₂)	Log Q(C ₃)	$\frac{Q(C_2)}{Q(CN)}$	$\frac{Q(C_3)}{Q(CN)}$
Dec 7.9	0.70	1.38	26.33	26.56	25.36	1.70	0.11
Dec 8.9	0.72	1.36	26.39	26.68	25.41	1.95	0.10
Dec 9.9	0.73	1.35	26.51	–	25.51	–	0.10
Mar 13.1	0.99	0.89	27.20	27.36	26.02	1.45	0.07
Mar 14.1	0.96	0.90	27.15	27.30	25.98	1.41	0.07
Mar 15.1	0.94	0.92	27.22	27.44	26.11	1.66	0.08
Mar 17.1	0.88	0.95	27.11	27.30	26.06	1.55	0.09
Mar 18.1	0.86	0.96	27.20	27.36	26.03	1.45	0.07
May 7.0	0.98	1.72	26.28	26.54	25.24	1.82	0.09
May 8.0	1.02	1.74	26.49	26.64	25.42	1.55	0.09
May 10.0	1.08	1.76	26.52	26.52	25.54	1.00	0.10
May 12.0	1.14	1.79	26.55	26.45	25.54	0.79	0.10
May 14.0	1.21	1.82	26.23	26.45	25.16	1.66	0.09

Table III.3: Production rates from La Palma observations. Typical formal errors are 0.02 in Log Q.

standard procedure as published by A'Hearn (1986). Thus their fluxes should be in the same standard system as those presented here, providing the filter characteristics are the same.

The production rates published by these authors needed revision; they used the original Delsemme velocity dependence and also a value for the C₂ *g*-factor that is now believed to be incorrect. The presently accepted *g*-factor is 2.04 times the old one . The revised figures are shown in Table III.4. The Q(CN) values were also recalculated using the most recent determination of the CN *g*-factor (Zucconi and Festou, 1985).

This enlarged dataset allows the investigation of the production ratios over the apparition. It was found that $Q(C_2)/Q(CN)$ varied considerably.

Date	Δ	R_h	Log Q(CN)	Log Q(C ₂)	Log Q(C ₃)	$\frac{Q(C_2)}{Q(CN)}$	$\frac{Q(C_3)}{Q(CN)}$
Nov 9	0.84	1.79	25.90	26.17	24.99	1.86	0.12
Nov 10	0.82	1.78	25.83	26.11	24.89	1.91	0.11
Nov 11	0.80	1.76	25.84	26.11	24.95	1.86	0.13
Nov 15	0.72	1.71	26.09	26.41	25.16	2.09	0.12
Nov 21	0.64	1.62	25.97	26.35	24.99	2.40	0.10
Nov 22	0.63	1.60	26.05	26.35	25.10	2.00	0.11
Nov 23	0.63	1.59	26.15	26.46	25.20	2.04	0.11
Nov 30	0.63	1.48	26.05	26.43	25.11	2.40	0.11
Dec 6	0.69	1.39	26.29	26.59	25.26	2.00	0.09
Dec 8	0.72	1.36	26.33	26.61	25.28	1.91	0.09
Dec 11	0.77	1.32	26.41	26.69	25.42	1.91	0.10
Dec 15	0.84	1.25	26.31	26.65	25.33	2.19	0.10
Dec 17	0.88	1.22	26.45	26.87	25.46	2.63	0.10
Dec 18	0.90	1.21	26.32	26.66	25.26	2.19	0.09

Table III.4: Production rates calculated from the observations of Catalano *et al.* (1986).

This ratio had a mean value of 2.07 ± 0.24 pre-perihelion and 1.52 ± 0.18 post-perihelion. The ratios of $Q(C_3)/Q(CN)$ displayed much less variance, with values of 0.11 ± 0.01 and 0.09 ± 0.01 respectively. Thus, post-perihelion, Halley displayed the characteristics of a normal comet as defined by Cochran (1987). Pre-perihelion the comet also falls within this description, but only just in the case of the $Q(C_2)/Q(CN)$ ratio.

A bare-ice surfaced nucleus would outgas water vapour with an inverse-square dependence on the heliocentric distance of the comet (Brandt and Chapman, 1981). Such a variation has rarely been observed for any molecular species and there is usually a higher power-law index. This was true in the case of Halley as reported by Craven and Frank (1987) and Catalano *et al.*

(1986). Account must be taken however of the OH and HCN observations by Shloerb *et al.* (1987a,b) of Halley, which do exhibit a R_h^{-2} behaviour. Least-squares fits were performed on the production rates presented and are shown in figures III.1(a, b & c). The pre-perihelion results are:

$$Q(CN) \propto R_h^{-3.38 \pm 0.42}$$

$$Q(C_2) \propto R_h^{-3.50 \pm 0.35}$$

$$Q(C_3) \propto R_h^{-2.76 \pm 0.44}$$

Post-perihelion, results are:

$$Q(CN) \propto R_h^{-2.69 \pm 0.25}$$

$$Q(C_2) \propto R_h^{-2.65 \pm 0.17}$$

$$Q(C_3) \propto R_h^{-2.33 \pm 0.29}$$

Errors are formal $1-\sigma$ errors from the least squares fit.

The first obvious feature apparent in these graphs is that the heliocentric dependence of the production rates of CN and C_2 was much greater before the comet rounded the sun, whereas the production rates themselves were generally higher for a given heliocentric distance post-perihelion. A similar effect was observed by various authors including Stewart (1987) and Feldman *et al.* (1987). Such an effect was modelled by Divine *et al.* (1986) by assuming a non-negligible thermal inertia for the surface of the nucleus. Weismann

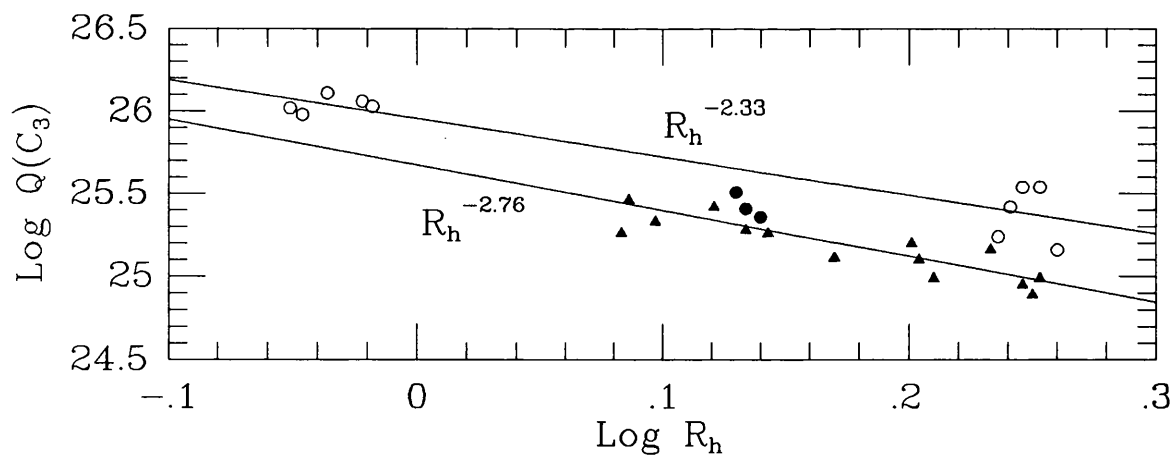
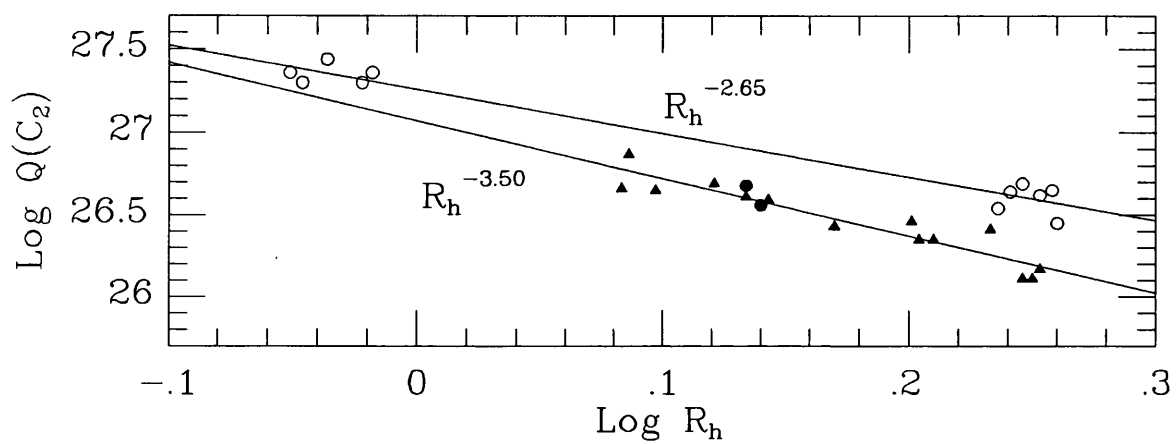
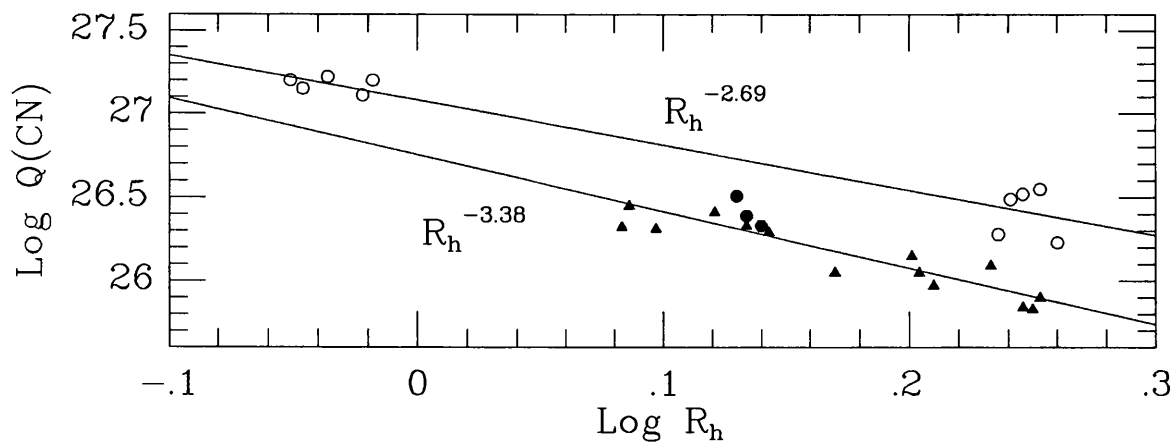


Figure III.1: Production of CN, C_2 and C_3 as a function of heliocentric distance. Filled circles are pre-perihelion production rates, open circles are post-perihelion. Filled triangles denote values derived from the fluxes from Catalano *et al.*, (1986).

(1987) has offered the alternative explanation of the effect as being caused by the sudden illumination of Halley's northern hemisphere as the comet passed perihelion, causing a large increase in the amount of volatile surface exposed to sunlight.

The heliocentric dependence indices do show something rather striking. The production rates of C_2 and CN vary in the same manner within the errors, whereas the C_3 production exhibits a much less steep variation with R_h over the apparition. This implies that the mechanism by which C_3 is released into the coma is controlled in a different manner to that of the more abundant species. It should be kept in mind here that C_3 is a true trace element. Previous authors have found an abundance $\simeq 0.1$ that of CN and C_2 and $\simeq 10^{-3}$ that of H_2O . One reason could be that C_3 (or its parent) is inhomogeneously mixed within the nucleus. Thus some jets when activated by the sun would contain an underabundance of the molecule. A more plausible explanation would be that the creation of C_3 is governed by a chemical process whose reaction rate is less dependent on temperature than that of C_2 and CN.

It is apparent from figure III.1 that the overall increase in production of C_2 after perihelion is less than that of CN. The fact that the power-laws for CN and C_2 are the same both pre and post-perihelion points to the pre-perihelion excess of C_2 being produced via another source with the same general depen-

dence on R_h . Regarding the possibility that volatile dust grains may be such a source (Wallis, Rabilizirov and Wickramasinghe, 1987), a power-law fit to the pre-perihelion dust production rates calculated by Tokunga *et al.* (1986) gives an index of $-(3.24 \pm 0.33)$. This is very similar to the power-law indices derived above for C_2 and CN, and could be evidence of the production of C_2 from dust particles rather than from the nucleus.

III.3 VARIABILITY OF OUTGASSING

The day-to-day variations in Table III.2 were investigated further in relation to the variation observed by Millis and Schleicher (1986). Figure III.2 shows the March production rates of C_2 superimposed on their lightcurve. These were first recalculated as they used the scalelengths derived by Combi and Delsemme (1986) and an outflow velocity of 1 km s^{-1} . As demonstrated in Williams *et al.* (1986) the agreement is extremely good. Also shown are the $Q(C_2)/Q(CN)$ and $Q(C_3)/Q(CN)$ ratios from Table III.2. $Q(C_3)/Q(CN)$ exhibits very little variation. The small increase in $Q(C_2)/Q(CN)$ on March 15.14 (by a factor 1.18 from the previous night) occurred when strong jets of C_2 and CN appeared in non-coincident positions in the inner coma (Cosmovici *et al.*, 1988). This points to the sources of the two molecules being distinct from each other at this time.

The original lightcurve published by Millis and Schleicher (1986) extends only to mid-April 1986. To compare the May data over three rotation periods later, account must be taken of the synodic rotation of the nucleus. This will advance or retard the zero-phase depending on both the sense of rotation and the orientation of the pole with respect to the orbital plane, in a similar fashion to the sidereal motion of the Sun caused by the Earths' orbital motion. The maximum discrepancy would be 0.44 days, assuming that the spin pole is at 90° to the orbital motion. The production rates and

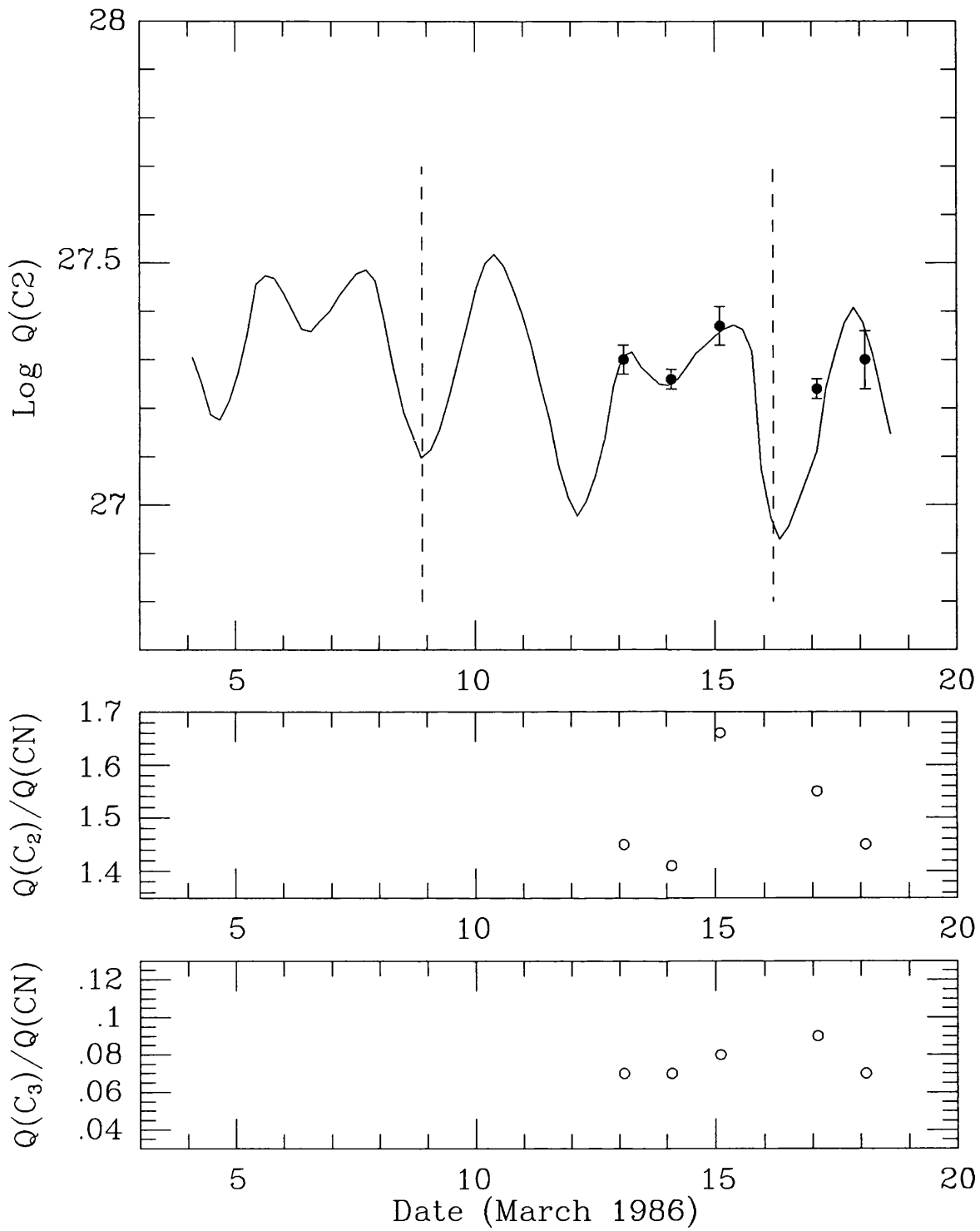


Figure III.2: Variation of production rates in March 1986. The curve is from Millis and Schleicher (1986).

ratios observed in May are shown in figure III.3, superimposed on the April data of Millis and Schleicher. The April lightcurve has just been shifted by 4 periods of 7.37 days. Certainly a large modulation in the production rate of C_2 is still evident. Both the decline in outgassing of the nucleus and the uncertainty in zero-phase make comparison with the observed lightcurve difficult.

Confirmation of the production ratio variation is best achieved by study of both the March and May data against phase of the lightcurve. The lowest values measured occur at a phase of $\simeq 0.72$ in March and $\simeq 0.64$ in May. Given the incomplete coverage these times agree with each other well.

A factor that could influence these observations is the scale-length of the parent molecule, coupled with the size of the aperture used. In both cases an increase in gas production would be starting according to the lightcurves. Given the values of the Haser scale-lengths and outflow velocities assumed above, the parental lifetimes of C_2 and CN are approximately 18 hours and 9 hours respectively. The physical radius of the aperture in May ranged between 14,600 and 18,000 km at the comet. Thus relatively more C_2 molecules would be produced outside the aperture than CN.

Following an outburst in gas production at the nucleus, this would have the effect of decreasing the observed $Q(C_2)/Q(CN)$ ratio when assuming a steady state model. As this is opposite to the observed behaviour, it may be

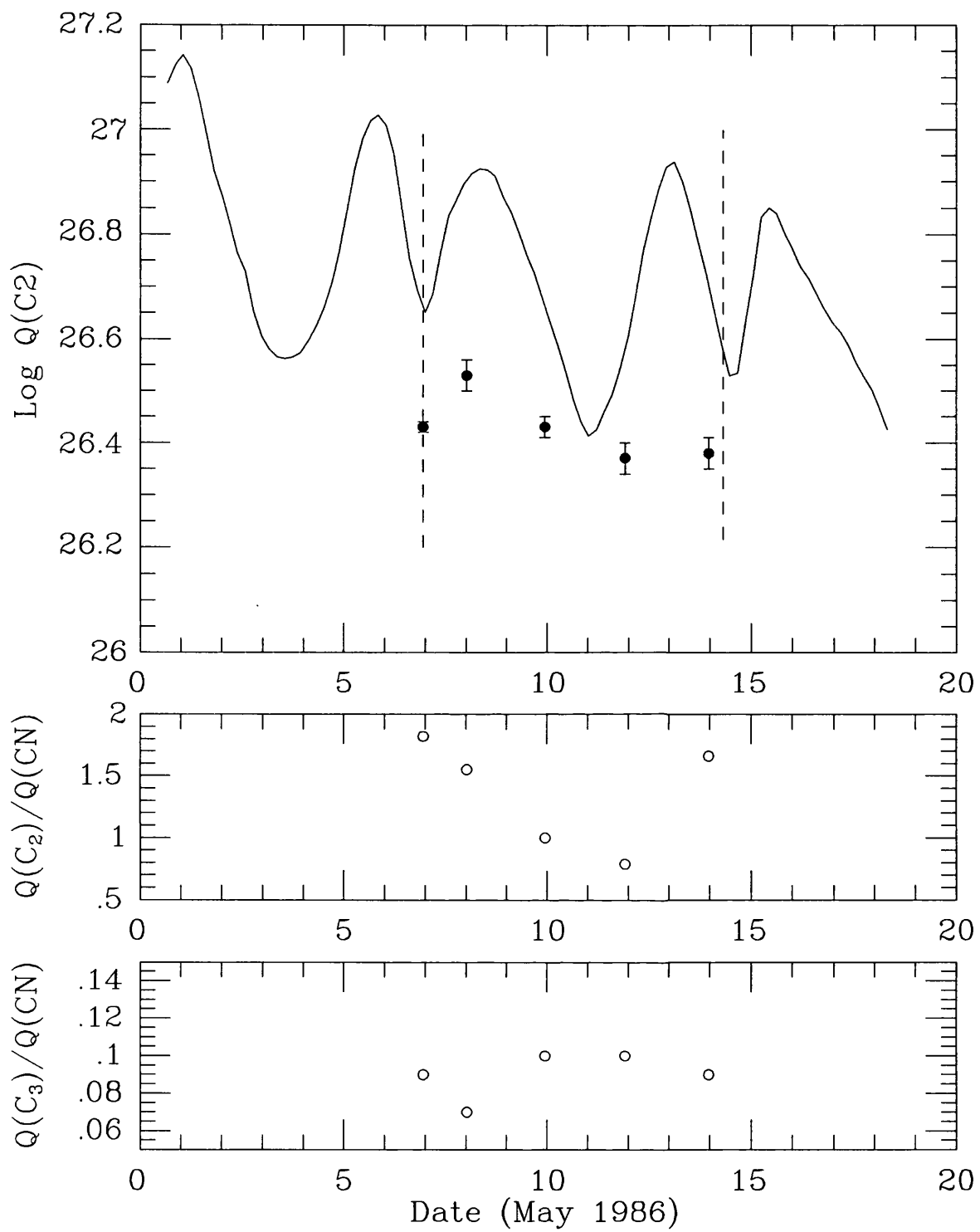


Figure III.3: Variation of production rates in May 1986. April lightcurve is taken from Millis and Schleicher (1986).

inferred that the variation in production ratios is a real effect, perhaps caused by either inhomogeneous composition of the nucleus or differing sources for the two molecular species.

III.4 MODELS INVOLVING MOLECULAR KINETICS

III.4.1 The Average Random Walk Model

The Average Random Walk Model (ARWM) was first presented by Combi and Delsemme (1980a). Like the Haser model, it assumes a spherically symmetric coma that is undistorted by radiation pressure. This has already been implemented in the case of OH (see section II.6). In their paper, Combi and Delsemme showed that for monokinetic ejection a simple average of sunward and anti-sunward profiles (where measured) was sufficient to cancel out the effects of radiation pressure. Simulations with a Maxwellian velocity distribution also showed this to be the case. Thus it may be used in relation to the modifications described above.

Each parent molecule is ejected from the nucleus and travels an average distance $\gamma_p = v_p \tau_p$ before dissociating. The resulting daughter molecules are isotropically ejected. This will give a mean velocity v_d perpendicular to the parents direction of travel. The radical will then decay on average after travelling a distance $\gamma_d = (v_p^2 + v_d^2)^{\frac{1}{2}} \tau_d$. The Haser scale-lengths l_p and l_d are then the radial projections of these distances.

The decay scheme is illustrated in Figure III.4. Given that μ is the ratio of a parent to daughter scalelength and that $\delta = \arctan(v_p/v_d)$, the scalelengths

Figure III.4: Vectorial decay scheme. Taken from Combi and Delsemme (1980a).

are related by

$$\gamma_d^2 - \gamma_p^2 = \gamma_{dH}^2 - \gamma_{pH}^2 \quad (\text{III.1})$$

and

$$\mu_H = \left(\frac{\mu + \sin \delta}{1 + \mu \sin \delta} \right) \mu . \quad (\text{III.2})$$

Equation III.10 can be re-written as

$$\mu = (\mu_H - 1) \frac{\sin \delta}{2} + \left[(\mu_H - 1)^2 \frac{\sin^2 \delta}{4} + \mu_H \right]^{\frac{1}{2}} \quad (\text{III.3})$$

Finally, the daughter molecules' radial velocity in the Haser model is given by

$$v_{dh} = v_d \frac{\gamma_{dh}}{\gamma_d} \quad (\text{III.4})$$

These equations relate the Haser scale-lengths of molecules to the true velocities and lifetimes of the species. Thus a logical procedure for the evaluation of molecular lifetimes is first the evaluation of the mean Haser scale-lengths. If the outflow velocity is known together with the dynamics of one of the molecules, then the decay time of the other may be found using the ARWM. This may be checked using the Monte-Carlo modelling procedure described below. If not, then the ARWM can be used to produce a range of acceptable lifetimes and velocities, from which Monte-Carlo simulations may be produced to fit the observations.

III.4.2 The Monte-Carlo Model

Neither the Haser model nor the ARWM can take into account solar radiation pressure. This is certainly needed for dealing with the large-scale distribution of CN, C₂ and C₃ in cometary comae. Hence, the data for Halley was analysed using in combination the Monte-Carlo model and the Average Random Walk Model (ARWM) as developed by Combi and Delsemme (1980a). The former is essentially the same as the vectorial model described by Festou (1981), in that it embodies the true kinetics of the molecules.

In the Monte-Carlo simulations, molecules are assumed to leave the nucleus (taken to be a point source) with a velocity v_p , and exponentially decay to form daughter molecules. The radicals are ejected from the parent

molecules with an velocity v_d due to excess dissociation energy. They themselves will decay after a lifetime τ_d . By simulating the flights of N molecules ejected from the nucleus between times $t = 0$ and $t = t_f$, a coma density distribution may be generated.

The times of parent production are given by

$$t_i = t_f R_1 \quad (\text{III.5})$$

where R_1 is a random number between 0 and 1. This and all other R_i used were generated using the routine G05CAF programmed in the Numerical Algorithms Group (NAG) software library. The ejection directions are given by

$$\phi_i = 2\pi R_2 \quad (\text{III.6})$$

$$\theta_i = \arccos(1 - 2R_3) \quad (\text{III.7})$$

The time t_p at which the the parent decays is given by the expression

$$R_4 = e^{\frac{-(t_p - t_i)}{\tau_p}} \quad (\text{III.8})$$

which after rearranging becomes

$$t_p = t_i - \tau_p \ln(R_4) \quad (\text{III.9})$$

Similarly the time of decay of the radicals is given by

$$t_d = t_p - \tau_d \ln(R_5) \quad (\text{III.10})$$

If the molecule decays such that $t_d < t_f$ or $t_p > t_f$, then the daughter does not contribute to the coma density at the time of observation. If however $t_d > t_f$ and $t_p < t_f$, then that molecule is observed at time t_f . Its position relative to the nucleus is calculated in a rectangular coordinate system so that the acceleration a due to solar radiation pressure has to be calculated for one axis only. If the z -axis lies along the comet-Sun line, and x lies in the plane defined by the comet-Sun-Earth, then the position of a radical at time t_f is:

$$\begin{aligned}
 x_f &= v_p(t_f - t_i) \sin \theta_p \sin \phi_p + v_d(t_f - t_p) \sin \theta_d \sin \phi_d \\
 y_f &= v_p(t_f - t_i) \sin \theta_p \cos \phi_p + v_d(t_f - t_p) \sin \theta_d \cos \phi_d \quad (\text{III.11}) \\
 z_f &= v_p(t_f - t_i) \sin \theta_p + v_d(t_f - t_p) \sin \theta_d - \frac{a}{2}(t_f - t_p)^2
 \end{aligned}$$

To calculate the column densities as seen from Earth, a new (x', y', z') frame of reference is used, with the z' -axis pointing to Earth and $y' = y$. The coordinates of a molecule in this frame are

$$\begin{aligned}
 x' &= x \cos \omega - z \sin \omega \\
 y' &= y \\
 z' &= x \sin \omega + z \cos \omega
 \end{aligned} \quad (\text{III.12})$$

where ω is the Sun-comet-Earth angle. Thus the x' -axis denotes the anti-sun vector as seen in the sky. To calculate column densities is then a case of binning the molecules into areas of the (x', y') plane.

From the model, the production rate is given by $Q = N/t_f$. In their original paper, Combi and Delsemme (1980a) arbitrarily chose the time over which the densities were summed as $t_f = 7 \times (\tau_p + \tau_d)$ to ensure that a steady-state coma was simulated. However a problem may arise if this time is less than the timescale for acceleration out of the coma. This was calculated assuming $v_p = 0.5 \text{ km s}^{-1}$ in a ‘worst case’ scenario *i.e.* both parent and daughter molecules initially travelling directly sunwards. This acceleration time was then taken as the lowest possible t_f .

As pointed out by Beard, Whelan and Gast (1985), a broad velocity distribution would considerably alter the column density profiles generated in the above model. However, in their analysis they assume the observations take place in the regime where molecular decay is negligible. As the Halley observations extended greater than 10^6 km from the nucleus, this precluded the use of their theoretical analysis.

The velocity distribution prevalent in the coma is somewhat uncertain. However recent modelling has assumed the molecules to be collisionally thermalised (Divine *et al.*, 1986) and provided the collision zone near the nucleus is large enough, this will be justified. Thus the original parent molecules in the Monte-Carlo simulation were given a Maxwellian velocity profile with the mean velocity V being a model parameter. This was done by generating gaussian velocity components for the parent molecules using the NAG library

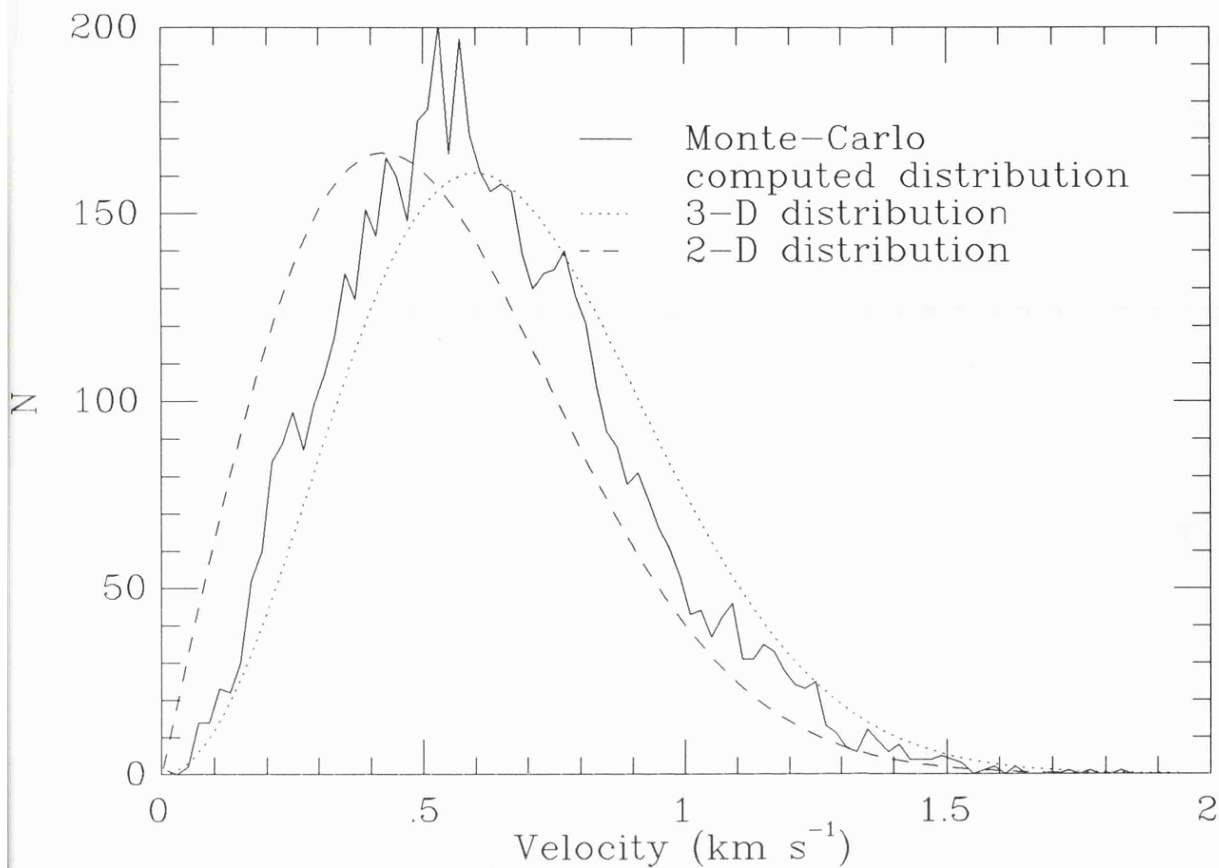


Figure III.5: Velocity distribution of molecules observed in a coma scan.

routine G05DDF.

The actual velocity distribution of the molecules that would be observed in a scan of the coma from the nucleus outwards has been generated by the Monte-Carlo model and is shown in figure III.5. In the limit of an infinitely small aperture, the velocity distribution of the molecules seen in a scan would be that of a two-dimensional gas. This is because of an observational selection effect in the outer coma, where all the molecules observed have a velocity dominated by the radial component. Due to this and the finite size of the aperture, the observed distribution is somewhere between a two-dimensional and a three-dimensional distribution.

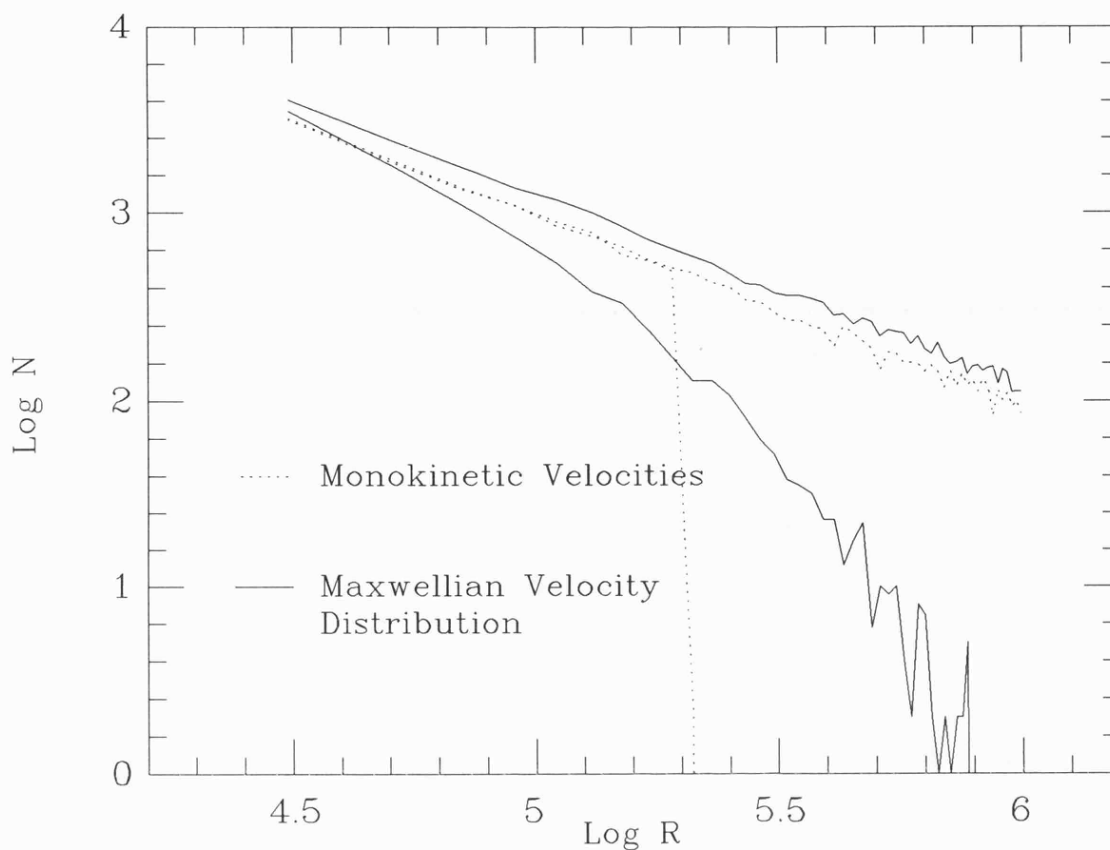


Figure III.6: Variation of column density with assumed parental velocity distribution.

Figure III.6 shows the effect on the observed distribution of molecules by including a range of velocities in the simulation. The case modelled was that of parent molecules both dissociating and undergoing repulsion due to solar radiation. In the monokinetic case both sunward and anti-sunward profiles follow closely an R_h^{-1} distribution as expected theoretically out to 2×10^5 km. At this distance the sunward profile cuts off dramatically, due to solar radiation pressure. The simulation with the Maxwellian velocity distribution has molecules well beyond this limit, with the sunward edge of the coma now placed at $\simeq 6 \times 10^5$ km from the nucleus.

III.5 COMA DISTRIBUTIONS AND MOLECULAR LIFETIMES

III.5.1 Suitability of Data.

The Monte-Carlo model and ARWM described above are necessary to analyse the CN, C₂ and C₃ coma distributions. The large *g*-factors of these molecules are expected to cause an asymmetry in the coma along the sun-comet line. This indeed was observed, particularly in the case of CN (see sections III.5.2 and III.5.3).

In order to produce the best possible fits to the data, it was decided to combine both the short and long-range scans in each direction to produce a composite column density profile that extended from 3×10^4 km out to 10^6 km from the nucleus. As the scans were taken at different times, this approach is only justifiable if the nuclear gas production is in a steady state. The December observations of OH had already shown this to be the case for all nights except the last. The May scans were unsuitable. To proceed it was necessary to reduce the total molecular counts to an average column density at the central position of the aperture. This could be done only if averaging the column density over a finite aperture did not significantly alter the true density distribution.

This method was tested by generating Haser column densities at the

aperture positions, and comparing them with total molecular counts at that position through an aperture as generated by equation II.5. When divided by the aperture area at the comet, the maximum difference in the two column densities was 0.01 in $\log(N)$. This result also implies that the use of rectangular aperture counting bins in the model to generate column densities at that position is allowable. The projected area of the bins was 4.0×10^8 km², while the 41-arcsec aperture had areas of 3.6×10^8 km² and 8.1×10^8 km² in December 1985 and May 1986 respectively.

III.5.2 CN

From the g -factors calculated by Zucconi and Festou (1985), the acceleration on the CN molecules at $R_h = 1.365$ AU and $\dot{R}_h = -26$ km s⁻¹ is 0.224 cm s⁻². Thus the possibility of a large Greenstein effect due to molecules being accelerated in the anti-solar direction could not be ignored. The g -factor variation published in the above study about the heliocentric velocity of the comet was included in the Monte-Carlo program. The resulting change in the deduced column density is shown in figure III.7, for a simulation of the CN parameters found by Combi and Delsemme (1980b) and the viewing angle for Halley. Although it was found that their CN lifetime did not reproduce the observations, this example serves to illustrate the effect of the non-zero

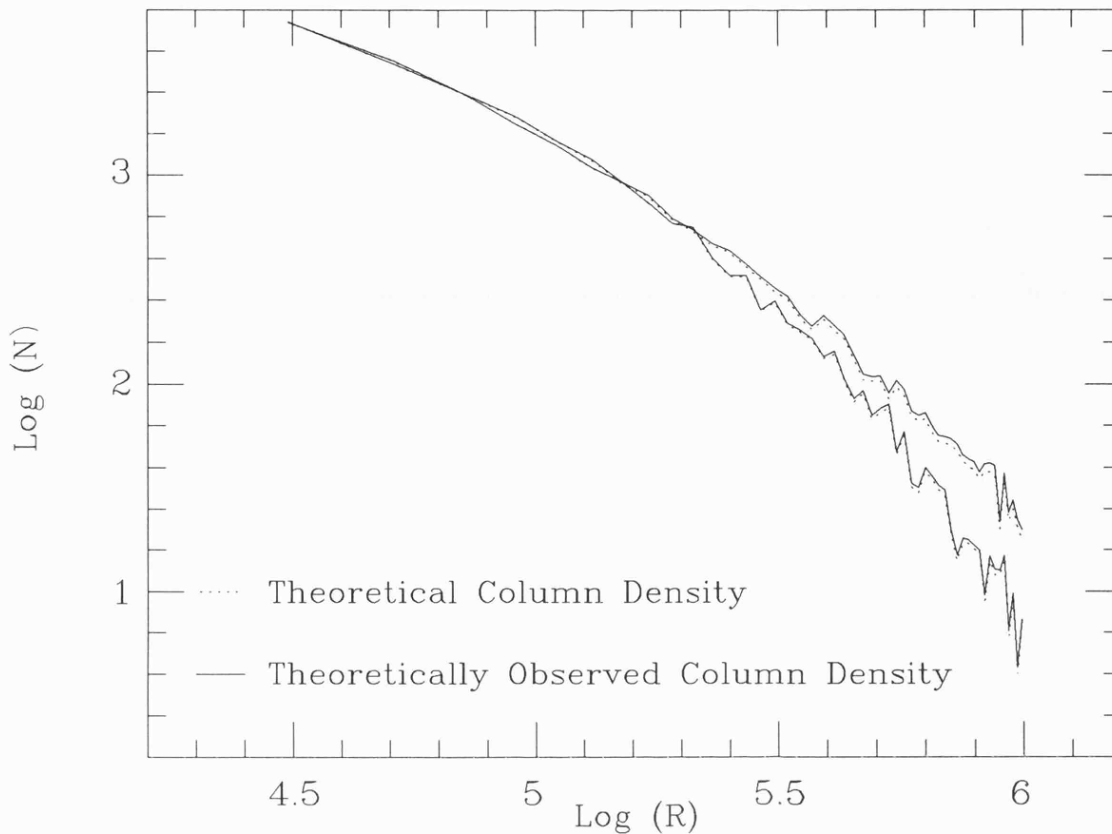


Figure III.7: Modification of the coma distribution of CN by the Greenstein effect.

molecular velocities in the rest-frame of the comet. It can be seen that the velocities 'downwind' of the nucleus produce only a small increase in luminosity and a corresponding small overestimate of the molecular abundances in this region.

Shown in Figure III.8 are the CN number densities observed, together with the Haser distribution computed using the scale-lengths derived by Cochran (1985). The asymmetry of the coma is obvious, with a large density enhancement apparent in the anti-solar direction. Independent Haser scale-lengths were found for the observed distributions. The mean scalelengths found were $l_p = 3.3 \times 10^4$ km and $l(CN) = 5.0 \times 10^5$ km at the comet. Both

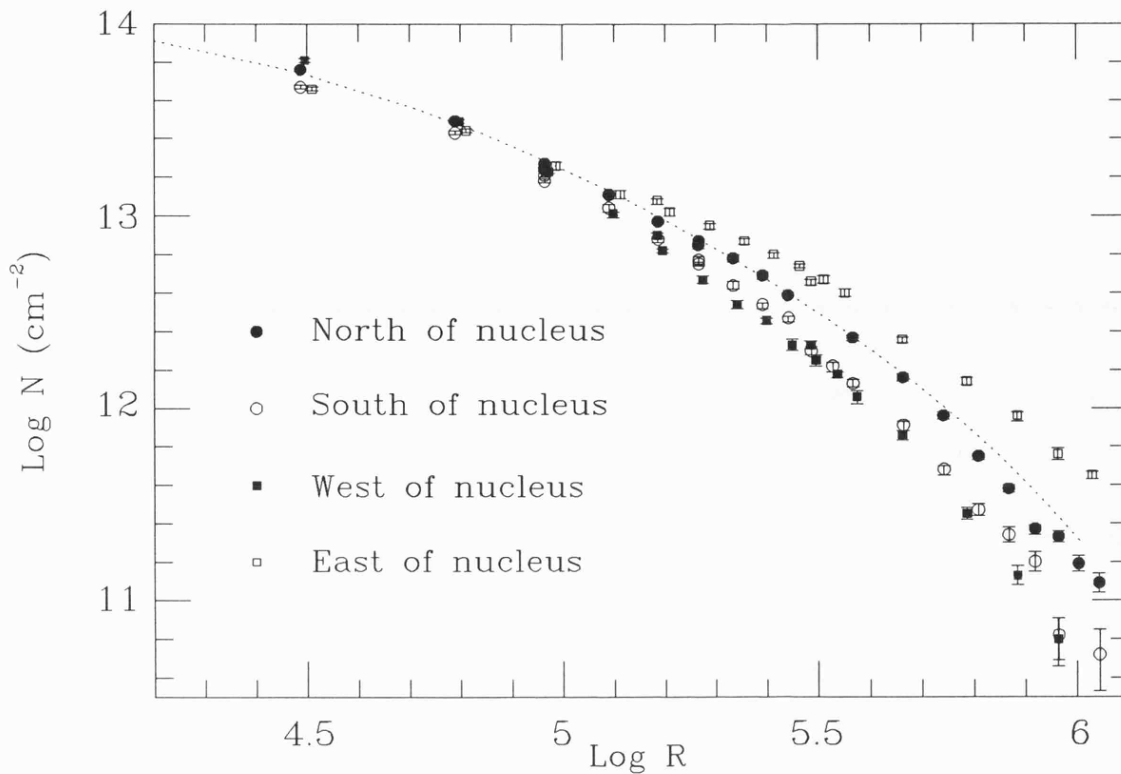


Figure III.8: Observed pre-perihelion CN column densities. Dotted line shows those predicted using a Haser model and the scale-lengths of Cochran (1985).

these scale-lengths and the Cochran scale-lengths were then used in the same manner as for the OH data (section II.6.1) to derive true photo-dissociation lifetimes. As previously, knowledge of the parent's life-time and daughter ejection velocity is required.

Unfortunately the identification of the parent from which CN is produced is disputed. HCN is the most likely molecular candidate and some studies have shown this to account for the observations *e.g.* Schloerb *et al.* (1987b). However the identification remains uncertain, as a one-to-one correspondence between the production of HCN and CN in Halley was not found by Bocklée-

Morvan *et al.* (1986). There also exists the identification by A'Hearn *et al.* (1986) of CN jets, which they interpret as evidence of a dust grain parentage. In this work HCN was assumed initially to be the only source of CN in the coma. This gives a theoretical photodissociation lifetime of 8.0×10^4 s at 1 AU and a CN ejection velocity from the parent of 1.02 km s^{-1} (Schloerb *et al.*, 1987).

When these parameters were put into a Monte-Carlo simulation, it was found that a close approximation to the North-South distribution of CN in December was obtained. By varying the parameters around these values by 20%, a much better fit was obtained. The final value accepted for $\tau(CN)$ was $(6.0 \pm 0.5) \times 10^5$ s at the comet, corresponding to $(3.2 \pm 0.5) \times 10^5$ s at 1 AU. The outflow velocity was of order 0.6 km s^{-1} . Reversing the calculation using the ARWM, the adopted Haser scalelengths are $l_p = 2.8 \times 10^4$ km and $l(CN) = 3.8 \times 10^5$ km at 1 AU. This compares favourably with the values as derived by Combi and Delsemme (1980b), but differs from those evaluated by Cochran.

Figures III.9(a-b) show the resulting fits from the Monte-Carlo simulations. The North-South scans are reproduced quite well. There does seem to be a small excess of CN to the North, the amount of which varies. Looking at the innermost points measured on the 8th December, the luminosities to the South and East were within 2% of each other, whilst to the North

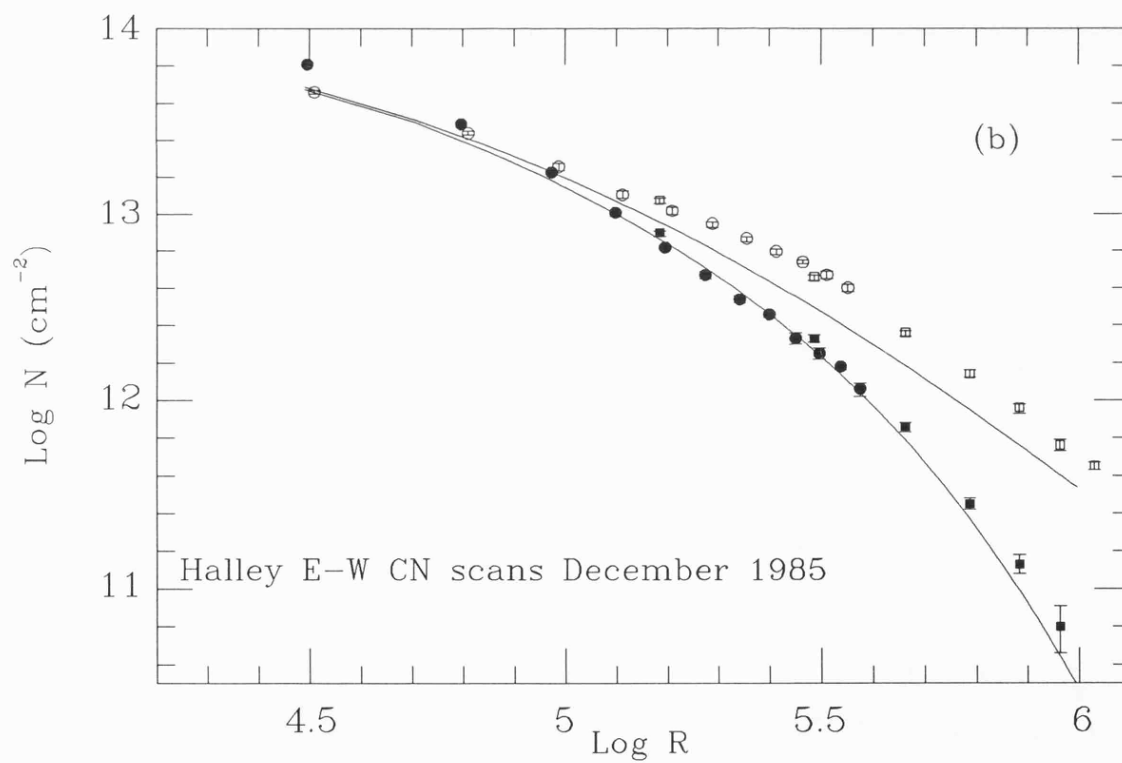
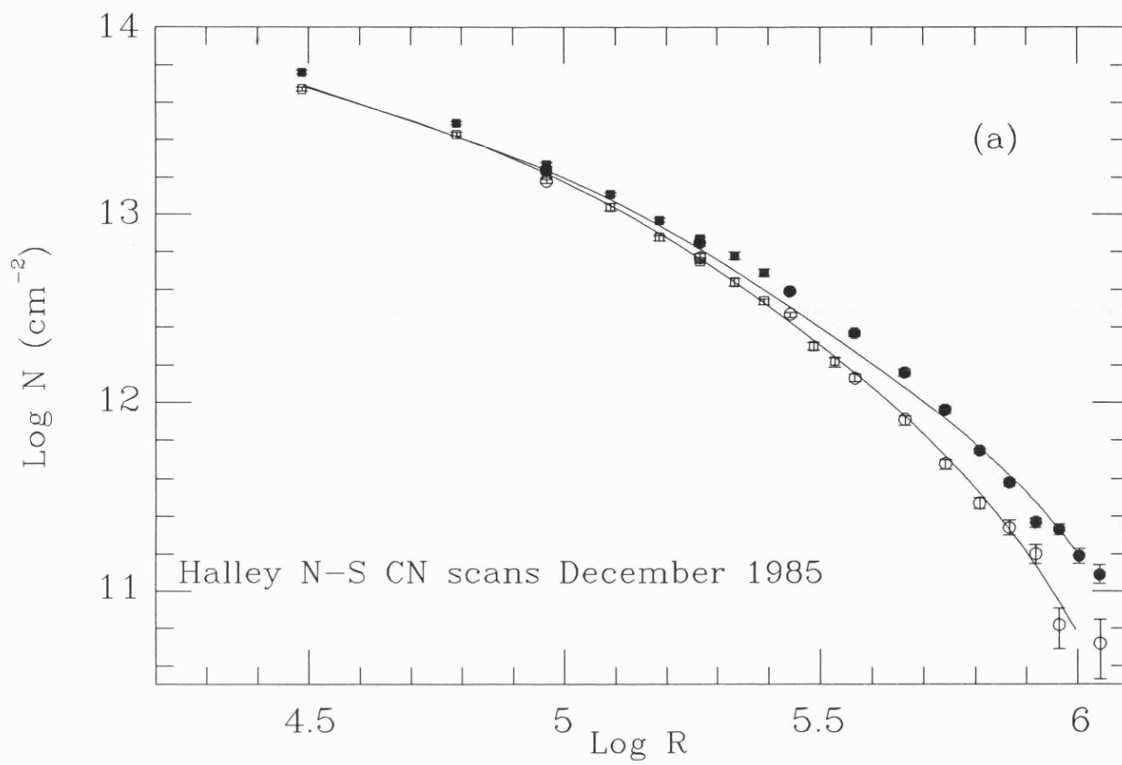


Figure III.9: Monte-Carlo fits to the observed CN distribution as described in the text. Point types are as for figure III.8.

it increased by over 20%. A differential molecular velocity between these two measurements would give a luminosity difference of approximately 10% via the Greenstein effect. Thus this may be taken as direct evidence of anisotropy in the inner coma of Halley at this epoch. This is also consistent with outgassing primarily from the sunlit hemisphere of the nucleus.

The model column densities in figure III.9(b) clearly demonstrate that the parameters above do not describe the observed CN distribution near the projected Sun-Comet line. The excess within $\simeq 10^5$ km West of the nucleus was caused by the outburst that occurred around December 9.2, as displayed by the OH results in Chapter II. There also appears to be an overabundance of CN in this direction at distances greater than 4×10^5 km. However, the inherent errors in the both the data and the counting statistics within the model means that this is by no means a definite feature. What is clear is the discrepancy between the model and the observations in the East scan. Between 10^5 km and 3×10^5 km the column density of CN observed rises steadily above that predicted. Beyond this projected distance the CN column density is 50% higher than expected out to the limit of our observations. There would appear to be three possible explanations for this apparent excess of CN.

Firstly, photosputtering from grains. This theory was originally put forward by A'Hearn *et al.* (1986) to explain the observation of CN jets imaged

in the inner coma of Halley. The inherent problem with this theory is that the suggested dust grain parents, the low mass sub-micrometre CHON particles detected by the GIOTTO and VEGA spacecraft, are not produced abundantly enough to create the observed jet densities (Cosmovici *et al.*, 1988).

Alternately, Rees, Meredith and Wallis (1986) observed narrow tail-like features in the images taken in the CN($\nu = 0$) passband on several occasions. They present a scenario in which dust grains rich in organic compounds are occasionally located within Halley's ion tail, as the ion tail is moved by the varying solar wind. The cometary plasma then provides a large source of photosputtering ions, creating a neutral tail in the same location as the plasma tail. The problem with interpreting our observations in this light is that one would expect the excess to decrease as one moves out of the coma, as the Sun-Comet line was 22° North of the scan. This effect is not exhibited in our data.

Finally, Combi (1987) has proposed that the jets may be composed of gas molecules. This 'trace-jet' hypothesis receives some support from the observations presented here, in that the CN excess starts its growth at a distance comparable to the scalelength of the parent HCN. However, as the acceleration of the molecules due to solar radiation differs by a factor of two, one would expect the morphologies of the CN and the C₂ jets to differ. This

is not supported by the images obtained by Cosmovici *et al.* (1988).

The cause of the CN excess therefore remains in dispute.

The Haser scale-lengths found give values of $l_p = 8.5 \times 10^4$ km and $l(CN) = 1.15 \times 10^6$ km when calculated for $R_h = 1.74$ AU. These compare favourably with the average values from the Haser model fits to the May 1987 data. However, as already discussed in section III.2, the nucleus was varying its output considerably during this epoch, a situation which will effect the molecular density profiles observed. Again the largest anisotropy near the nucleus appears to the North, being 78% more than to the East. Variation via the Greenstein effect would be expected to be less than 10%. The derived number densities are thus again consistent with outgassing primarily from the sunlit hemisphere of the nucleus.

Using the lifetime for CN found from the December data, a number of simulations were performed of the May CN molecular profiles with a range of outflow velocities from the nucleus. The best fit to the data was found by assuming a mean parent velocity of 0.7 km s^{-1} and is shown in figure III.10. Surprisingly this is higher than that found in the pre-perihelion data, even though the comet was then considerably nearer the sun. This result is supported by other ground-based observations concerning the velocity field in Halley's coma. Direct measurements of near-infrared H_2O lines by Larson *et al.* (1987) at heliocentric distances of 1.13 AU pre-perihelion and 1.02 AU

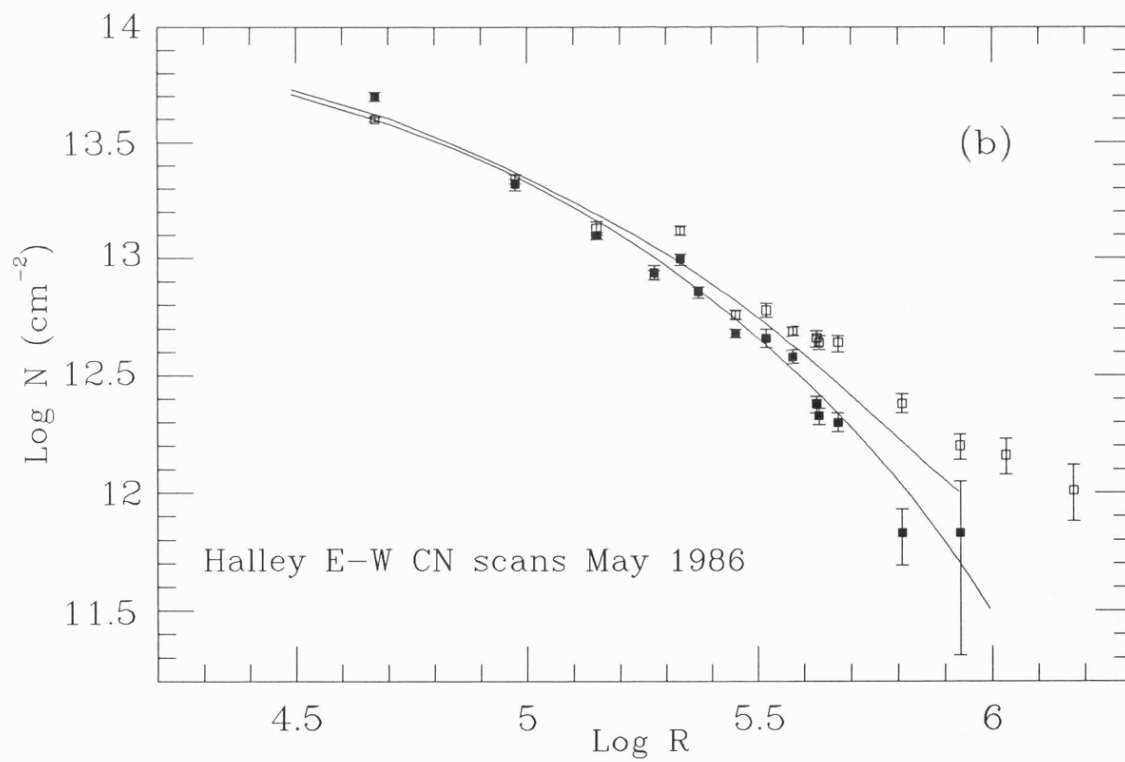
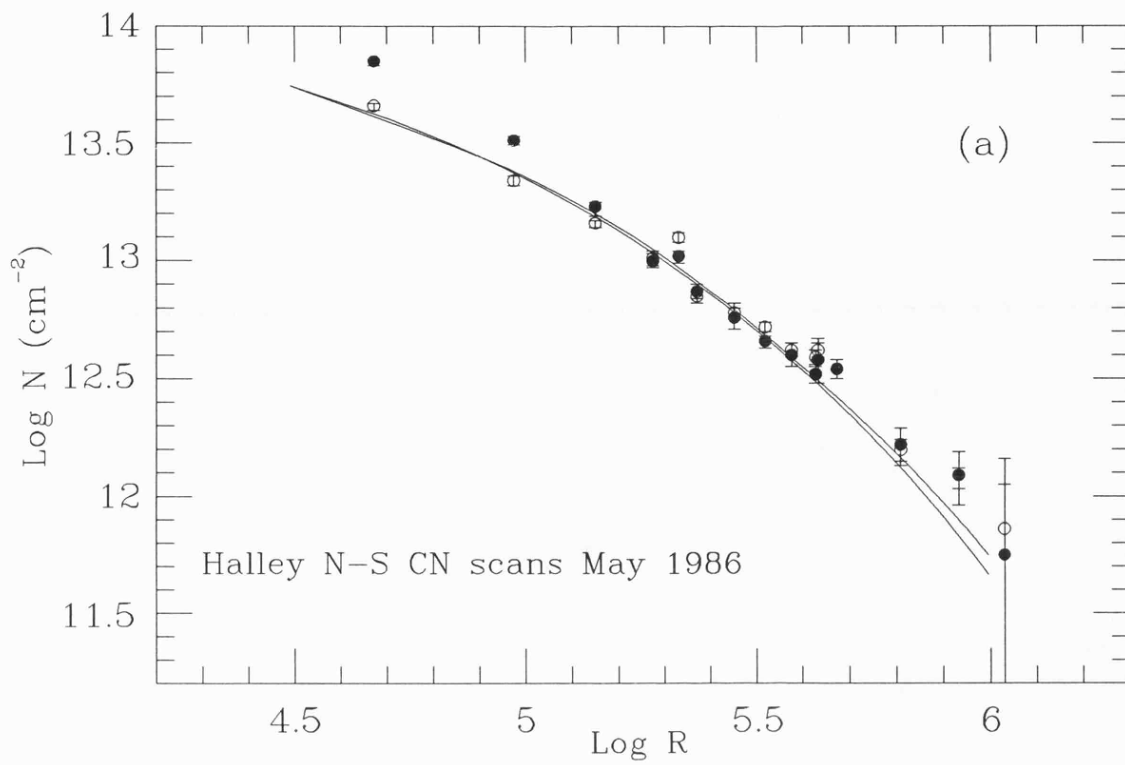


Figure III.10: Monte-Carlo fits to the post-perihelion CN data. Point styles are as in figure III.8

post-perihelion gave outflow velocities of $0.9 \pm 0.2 \text{ km s}^{-1}$ and $1.4 \pm 0.2 \text{ km s}^{-1}$ respectively.

Scaling the model results to the observations provides a direct estimate of the production rates of CN at the times of observation. These were $7.6 \times 10^{26} \text{ mols s}^{-1}$ in December and $7.1 \times 10^{26} \text{ mols s}^{-1}$ in May. Comparison with the Haser model results in section III.2, of 2.3×10^{26} and $2.6 \times 10^{26} \text{ mols s}^{-1}$ respectively, shows that this well-established method seriously underestimates the sublimation rates from the nucleus.

III.5.3 C_2

The December C_2 column densities, together with the Haser scale-lengths found by Cochran (1985), appear in figure III.11. In this case the standard scale-lengths seem to reproduce the observations very well in all directions except towards the sun. This is surprising, as the large acceleration caused by solar radiation pressure (0.47 cm s^{-2} at 1.365 AU) would be expected to push the molecules behind the nucleus. To derive the true dissociation for C_2 involves considerably more calculation than for CN, as there is no identification of the parents of C_2 . The obvious choice of C_3 has not been considered because it is about ten times less abundant than C_2 in cometary comae (but see subsection III.5.4). Other possibilities such as C_2H_2 and C_2H have been discounted due to disagreement between their theoretical lifetimes

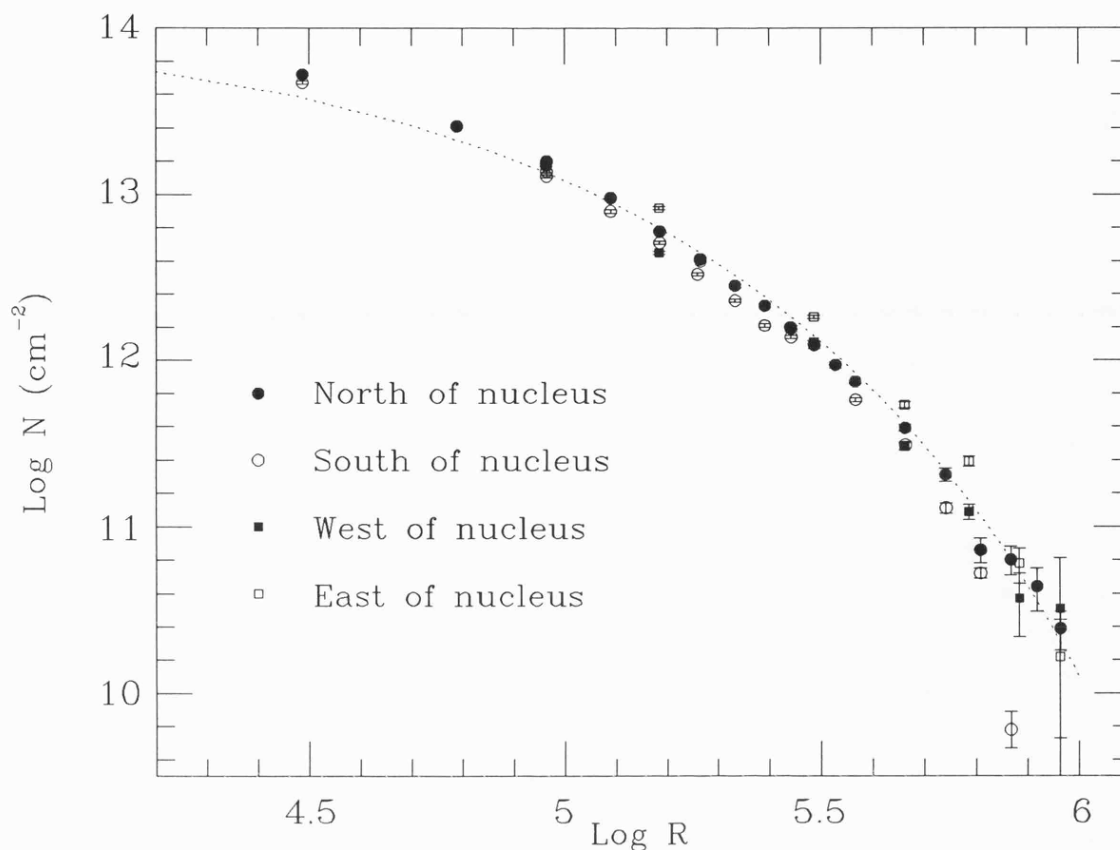


Figure III.11: Observed C₂ column densities pre-perihelion. Dotted line shows the predicted distribution using the scale-lengths of Cochran (1985).

and that observed for the creation of C₂ (Combi and Delsemme, 1986).

The lifetimes for the creation and destruction of C₂ in the ARWM are a function of the measured Haser scalelengths and the velocities of the parent and daughter molecules. Figures III.12a and III.12b show this dependence as a function of v_p and v_d , assuming either Cochran's scalelengths or those found from the December observations. Simulations using Combi and Delsemme's lifetimes did not match the data for outflow velocities less than 1 km s⁻¹.

The problem was to try and minimise the search space for the Monte-Carlo simulations, as generating density distributions by varying both v_p and

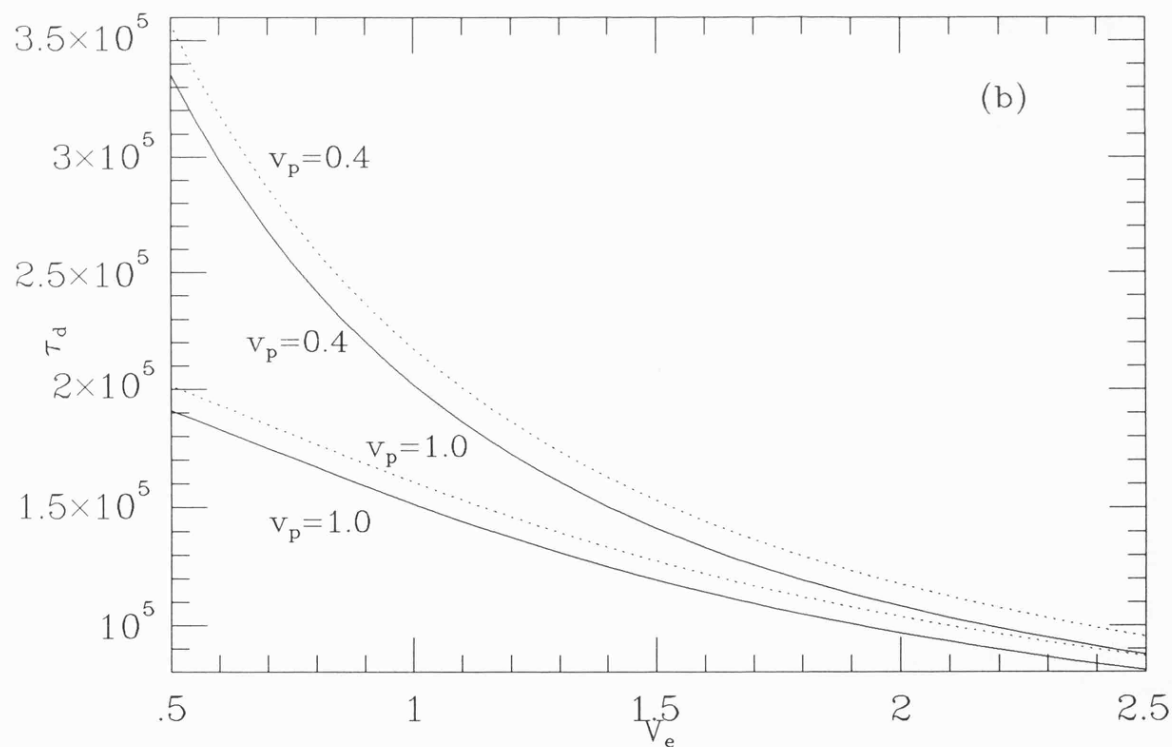
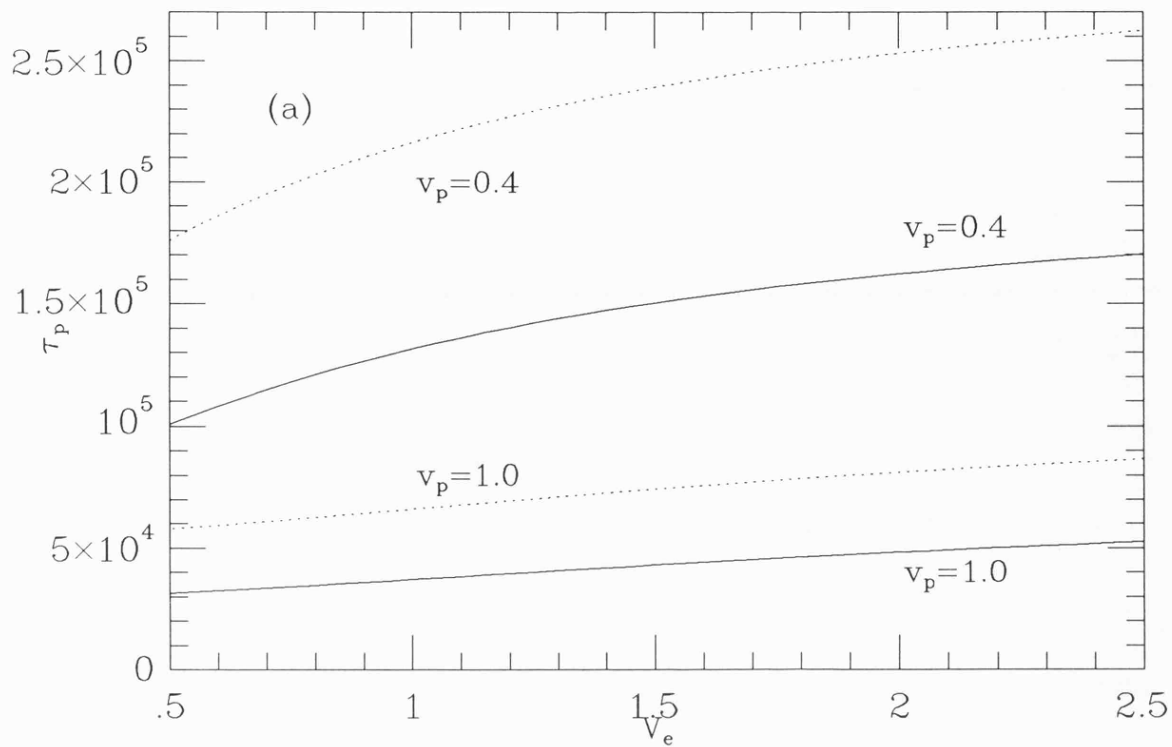


Figure III.12: Creation and destruction scale-times of C_2 as a function of parent and daughter velocities.

v_d would have involved an inordinate amount of computer time. The clue came from comparison of the profiles North and South of the nucleus. These are very similar out to $\simeq 6 \times 10^5$ km, showing that radiation pressure has not had a substantial effect on the distribution. This in turn suggests that either the terminal velocity of the C_2 molecules is high enough to avoid significant deceleration by solar radiation, or that the source scale-length is very large compared to that of C_2 . In either case the C_2 lifetime cannot be so long as to allow a large asymmetry to appear in the column densities.

Figure III.12 (b) demonstrates that the smallest possible lifetimes for C_2 occur for ejection velocities of greater than 1.5 km/s. From figure III.12(a) this gives a parental lifetime of the same order. Models were generated assuming v_p to lie between 0.5 and 0.7 km s⁻¹ *i.e.* comparable with the CN parental outflow velocity already found. The best fitting simulation to the North-South data is shown in figure III.13(a). The resulting parameters for the C_2 molecule are

$$v_p = 0.5 \text{ km s}^{-1}$$

$$v_d = 2.0 \pm 0.2 \text{ km s}^{-1}$$

$$\tau_p = 1.22 \times 10^5 \text{ s at comet}$$

$$\tau(C_2) = 1.07 \times 10^5 \text{ s at comet}$$

The resulting East-West model simulations are shown in figure III.13(b). Agreement is poor compared to the North-South scans, but account must

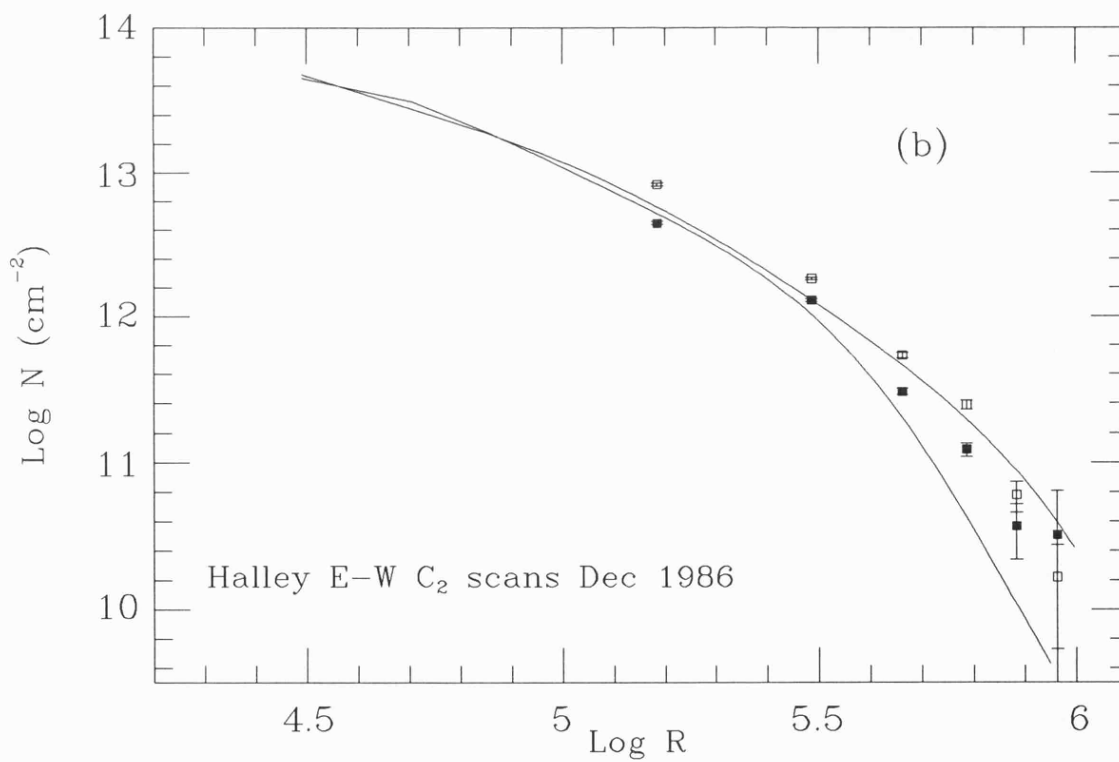
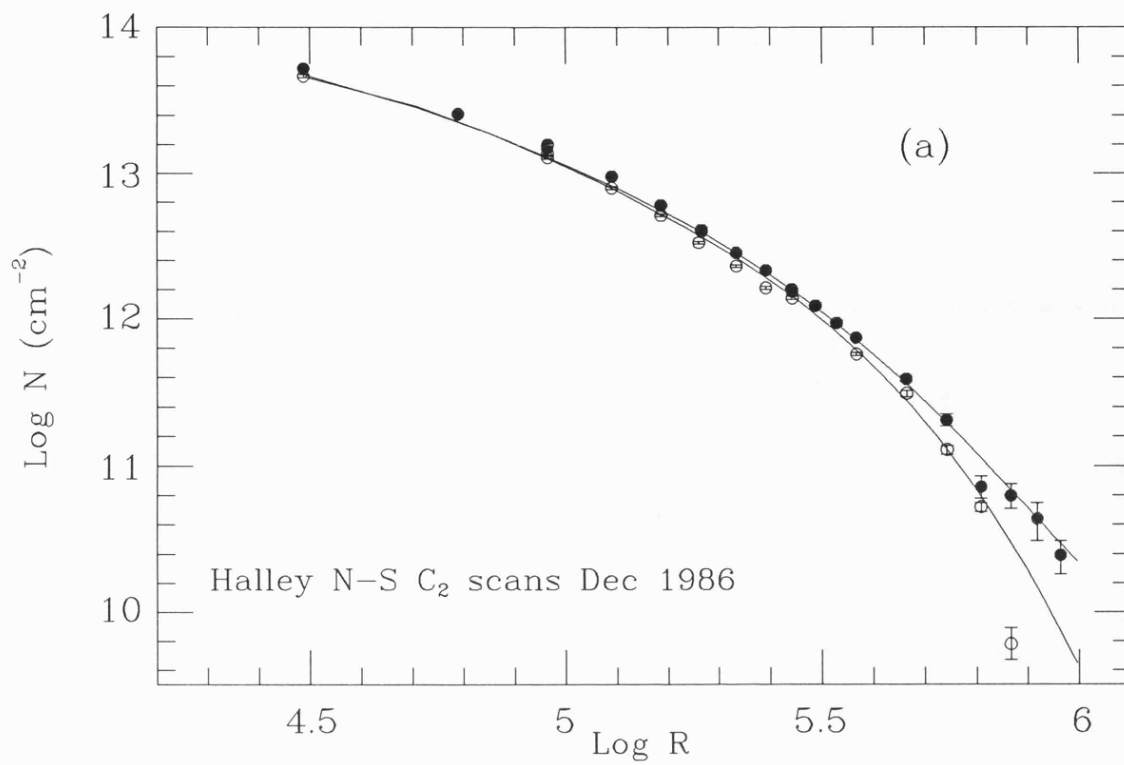


Figure III.13: The distribution of C_2 according to the Monte-Carlo model parameters described in the text.

be taken of the low signal to noise for most of the data here. The resulting lifetimes when reduced to 1 AU, $\tau_p = 6.4 \times 10^4$ s and $\tau(C_2) = 5.7 \times 10^4$ s, are significantly different from previous determinations due to the high daughter ejection velocity.

When scaled to a heliocentric distance of 1.74 AU, the Monte-Carlo model data produces the profiles seen superimposed on the observed column densities in figures III.14(a,b). As in the case of the CN analysis, the poor fit to some points was taken to be due to the high variability of outgassing. A reasonable representation of the observed column densities was found for outflow velocities of 0.7 ± 0.1 km s⁻¹, as for CN. The only discrepancy readily apparent, considering the quality of the data, is near the nucleus. This may be, as stated before, due to the nuclear sublimation increasing. There is also the possibility that it may be caused by the presence of C₂ jets. This question is only resolvable by inspection of images taken on this date.

The production rates were found from the model to be 9.0×10^{26} mols s⁻¹ in December and 1.1×10^{27} mols s⁻¹ in May. Again, comparison with the Haser modelling results in section III.2 (4.2×10^{26} and 3.9×10^{26}) show that the Haser model underestimates the true production rate by a factor of 2 or more. As this is the case with CN, the production ratios found from the Monte-Carlo simulations are similar to those found using the Haser model.

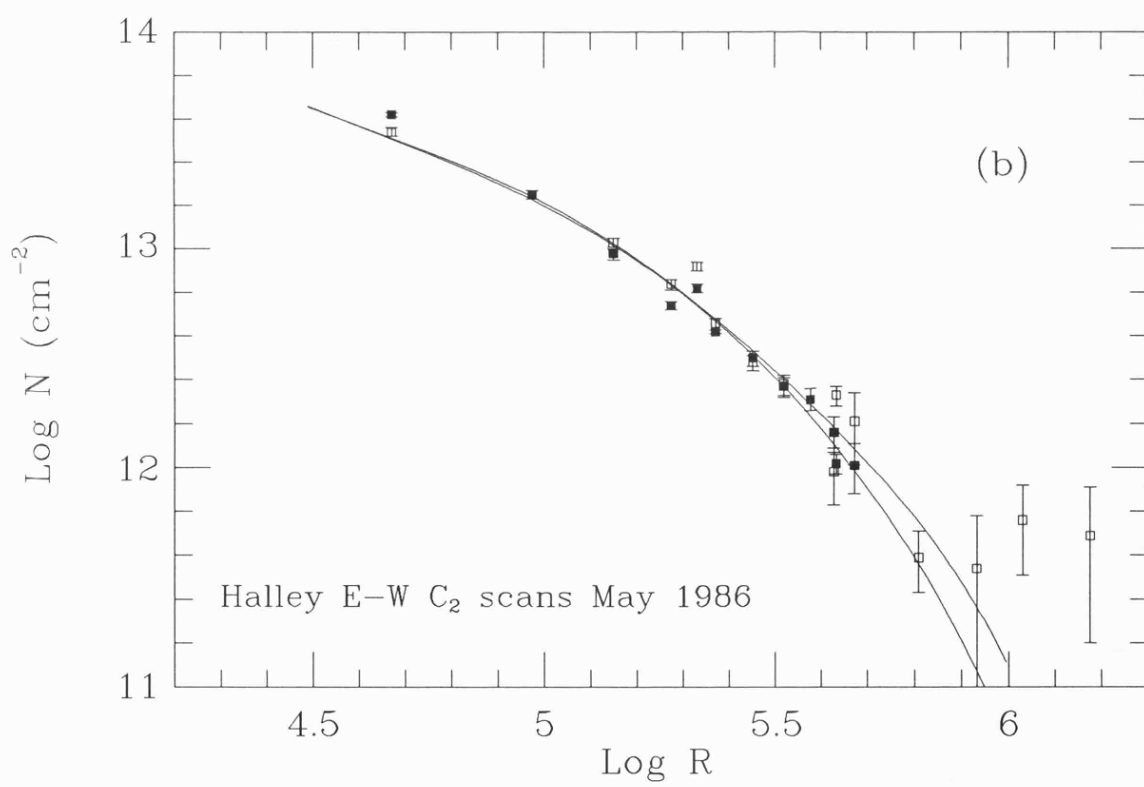
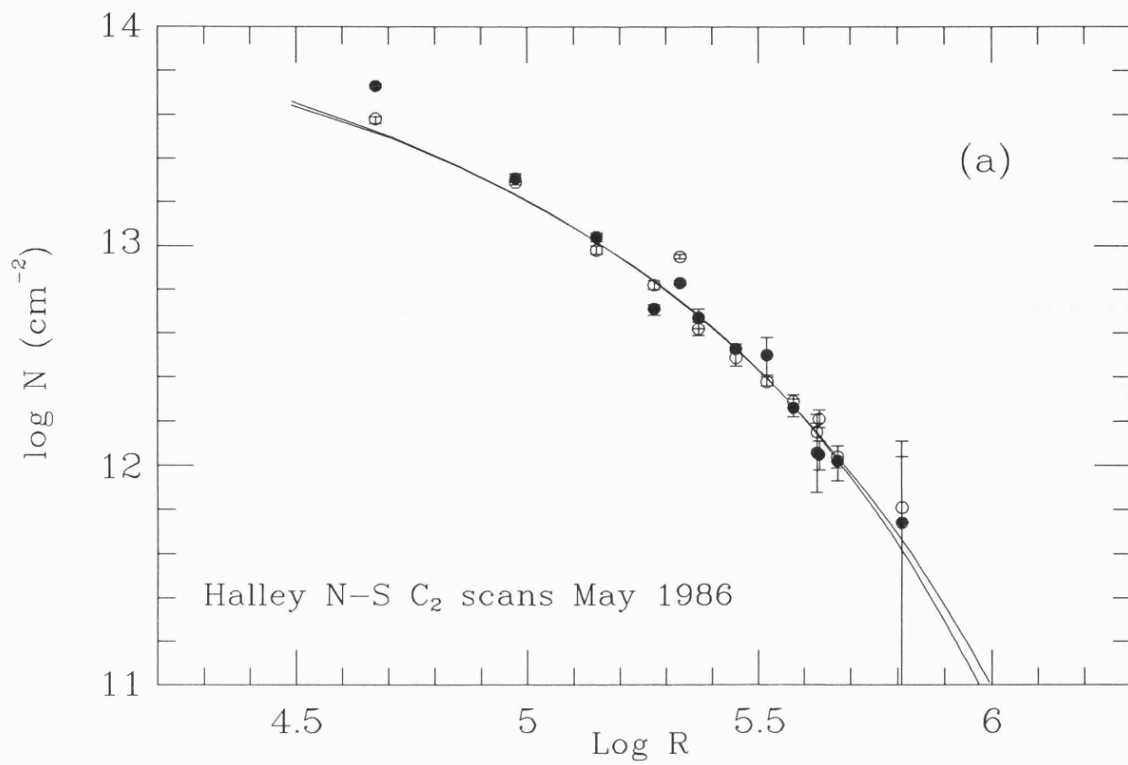


Figure III.14: Monte-Carlo model post-perihelion column densities using pre-perihelion molecular lifetimes.

The ratios found are:

$$Q(C_2)/Q(CN) = 1.3 \pm 0.1, R_h = 1.36\text{AU}$$

$$Q(C_2)/Q(CN) = 1.5 \pm 0.1, R_h = 1.74\text{AU}$$

The errors are produced from the uncertainty in the relative scaling between the simulations and the column densities measured in the inner coma.

III.5.4 C₃

The C₃ data is of poorer quality than that of either CN or C₂ due to two factors; the relative weakness of the molecular emission above the underlying dust continuum and the shorter lifetime of the molecule. It was felt that a general analysis via the ARWM and Monte-Carlo program would not be worthwhile considering the low signal-to-noise. The data from December are shown in figure III.15, together with the Haser scale-length deduced by Cochran (1985). For the first time there is a substantial difference between the density profiles observed and those derived by Cochran. The mean Haser scalelengths found from this data were:

$$l_p = 1.0 \times 10^3 \text{ km}$$

$$l(C_3) = 5.0 \times 10^4 \text{ km.}$$

These can be compared with Cochran's values of $l_p = 5.8 \times 10^3 \text{ km}$ and $l(C_3) = 2.7 \times 10^5 \text{ km}$. Clearly the C₃ scale-length observed by us is less than

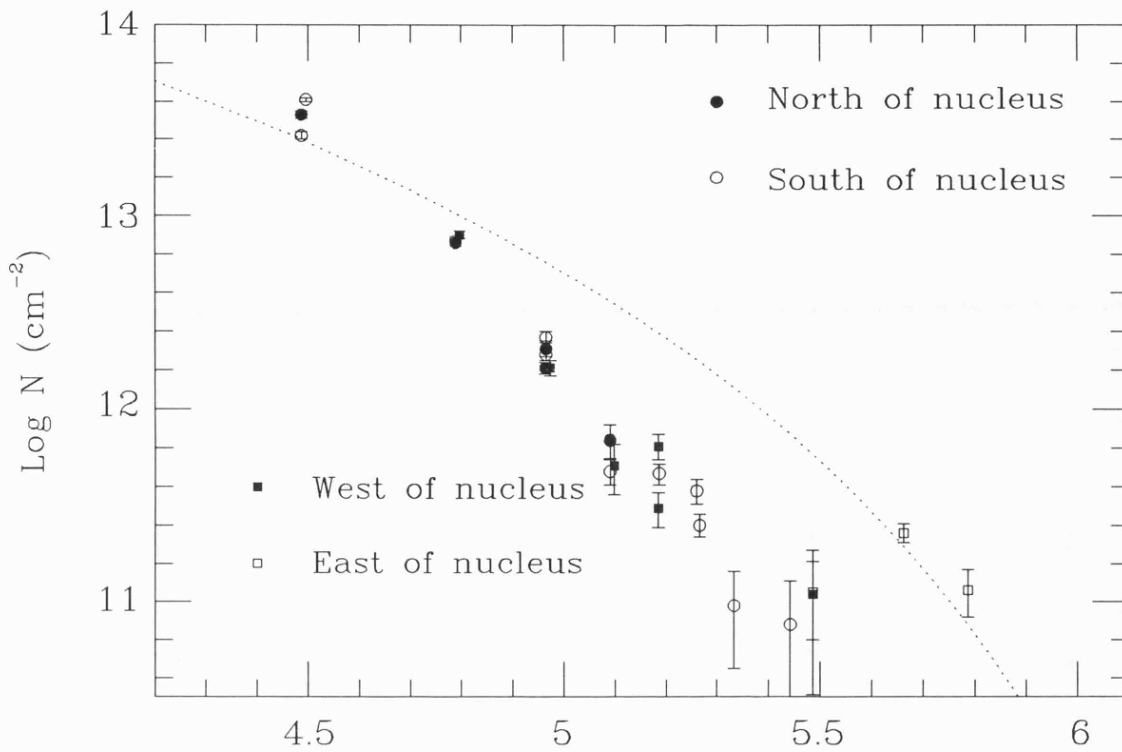


Figure III.15: Observed C_3 column densities in December 1985. Dotted line shows the predicted distribution given by the scale-length derived by Cochran (1985).

that expected, even though the errors on the measurements are substantial.

Given that the C_3 must dissociate into C_2+C , it was decided to check whether C_3 could be a significant parent of C_2 when modelled more realistically than in Haser terms. The fundamental assumption was that the destruction lifetime of C_3 should equal the creation lifetime of C_2 , already found to be 1.22×10^5 s above. Also, the terminal velocity of C_3 should equal that of the parent of C_2 , i.e. 0.5 km s^{-1} .

With these two conditions, Monte-Carlo simulations were run with the Haser scale-lengths found above, and for outflow velocities between 0.1 and

0.4 km s⁻¹. The case of C₃ being ejected directly from the nucleus with $v_p =$ 0.5 km s⁻¹ was also considered. In no case was a good reproduction of the observed data found, as the anti-solar acceleration of 0.30 cm s⁻² caused by the high g -factor of this molecule produced highly dissimilar column densities to the North and South of the nucleus.

III.6 Future Work

This chapter has dealt with the distributions of carbonaceous molecules in Halley's coma as far as the data allows. Results include confirmation of the variability of outgassing as seen by other observers, and the evaluation of *true* photo-dissociation lifetimes of CN and C₂. As is the rule of most scientific investigations, this study has raised as many questions as it has attempted to answer.

An obvious line of inquiry is the stability of the lightcurve studied in section III.2. Was it apparent at any time pre-perihelion, and did it survive until sublimation from the surface finally ceased? One would think this should be the case, considering that the outgassing should be tied to the rotation of the nucleus. If this is so, then why did this variability not start until mid-December 1985, when a coma had been apparent since at least August, 6 months before perihelion (IAUC 4094). Data able to help with this investigation will become available with the publication of the IHW photometry archive.

The scans in four orthogonal directions have proved extremely useful in deducing the global distribution of molecules in Halley's coma. However the full surface-brightness distribution can only be realised with the use of a two-dimensional detector such as a CCD or IPCS. The problem here is that most such devices have a very narrow field of view, unsuitable for objects such

as the $\simeq 1^\circ$ diameter coma of Halley. At least one system for viewing such objects is known of (Rees, Meredith and Wallis, 1986) and it is intriguing that their imaging system also showed anomalies in the distribution of CN molecules.

Finally, one question remains that even the huge amount of data in the IHW archive will not be able to answer. Is Comet P/Halley a normal comet? While previously published data on comets such as Comet Bennet, Comet West and Comet Kohoutek will give clues, techniques of observation have advanced so rapidly since the last apparition of a bright comet. We need to acquire for another object the high signal-to-noise observations that were the norm for Halley. Luckily, with Comet Brorsen-Metcalf reaching perihelion in September 1989, we will be able to establish very soon whether our depth of understanding stretches to one comet or to many.

III.7 REFERENCES

A'Hearn, M.F., Birch, P.V., Feldman, P.D. & Millis, R.L., 1985, *Icarus*, **64**,

1.

A'Hearn, M.F., *IHW Photometry & Polarimetry Net Newsletter*, 3rd

February 1986.

A'Hearn, M.F., Hoban, S., Birch, P.V., Bowers, C., Martin, R. &

Klinglesmith III, D.A., 1986, *Nature*, **324**, 649.

Beard, D.B., Whelan, T.A. & Gast, M.A., 1985, *Astrophys. J.*, **295**, 668.

Bocklée-Morvan, D., Crovisier, J., Despois, D., Forveille, T., Gérard, E.,

Schraml, J. & Thum, C., 1986, *20th ESLAB Symp.*, *ESA SP-250*, I, 365.

Brandt, J.C. & Chapman, R.D., 1981, in *Introduction to Comets*,

Cambridge University Press, 128.

Catalano, F.A., Baratta, G.A., Presti, C.Lo & Strazzulla, G., 1986, *Astron.*

Astrophys., **168**, 341.

Cochran, A.L., 1985, *Astron. J.*, **90**, 2609.

Cochran, A.L., 1987, *Astron. J.*, **92**, 231.

Combi, M.R., 1987, *Icarus*, **71**, 178.

Combi, M.R., & Delsemme, A.H., 1980a, *Astrophys. J.*, **237**, 633.

Combi, M.R., & Delsemme, A.H., 1980b, *Astrophys. J.*, **237**, 641.

Combi, M.R., & Delsemme, A.H., 1986, *Astrophys. J.*, **308**, 472.

Cosmovici, C.B., Schwartz, G., Ip, W.-H. & Mack, P., 1988, *Nature*, **332**,

705.

Craven, J.D. & Frank, L.A., 1987, *Astron. Astrophys.*, **187**, 351.

Delsemme, A.H., 1982, in *Comets*, ed. L.L. Wilkening, University of Arizona, Tucson, 85.

Divine, N., Fechtig, H., Gombosi, T.I., Hanner, M.S., Keller, H.U., Larson, S.M., Mendis, D.A., Newburn Jr., R.L., Reinhard, R., Sekanina, Z. & Yeomans, D.K., 1986, *Space Sci. Rev.*, **43**, 1.

Feldman, P.D., Festou, M.C., A'Hearn, M.F., Arpigny, C., Butterworth, P.S., Cosmovici, C.B., Danks, A.C., Gilmozzi, R., Jackson, W.M., McFadden, L.A., Patriarchi, P., Schleicher, D.G., Tozzi, G.P., Wallis, M.K., Weaver, H.A. & Woods, T.N., 1987, *Astron. Astrophys.*, **187**, 325.

Festou, M.C., 1981, *Astron. Astrophys.*, **95**, 69.

Larson, H.P., Mumma, M.J. & Weaver, H.A., 1987, *Astron. Astrophys.*, **187**, 391.

Millis, R.L., & Schleicher, D.G., 1986, *Nature*, **324**, 646.

Newburn Jr., R.L. & Spinrad, H., 1984, *Astron. J.*, **89**, 289.

Rees, D., Meredith, N.P. & Wallis, M.K., 1986, *20th ESLAB Symp., ESA SP-250*, I, 493.

Schloerb, F.P., Claussen, M.J. & Tacconi-Garman, L., 1987, *Astron. Astrophys.*, **187**, 469.

Schloerb, F.P., Kinzel, W.M., Swade, D.A. & Irvine, W.M., 1987, *Astron.*

Astrophys., **187**, 475.

Stewart, A.I.F., 1987, *Astron. Astrophys.*, **187**, 369.

Tokunga, A.T., Golisch, W.F., Griep, D.M., Kaminski, C.D. & Hanner,

M.S., 1986, *Astron. J.*, **92**, 1183.

Wallis, M.K., Rabilizirov, R. & Wickramasinghe, N.C., 1987, *20th ESLAB*

Symp., *ESA SP-250*, **II**, 251.

Weismann, P.R., 1987, *Astron. Astrophys.*, **187**, 873.

Williams, I.P., Andrews, P.J., Fitzsimmons, A. & Williams, G.P., 1987,

Mon. Not. R. astr. Soc., **226**, 1p.

Wyckoff, S., Tegler, S., Wehinger, P.A., Spinrad, H. & Belton, M.J.S., 1988,

Astrophys. J., **325**, 927.

Zucconi, J.M. & Festou, M.C., 1985, *Astron. Astrophys.*, **150**, 180.

Chapter IV

THE BEHAVIOUR OF HALLEY'S PLASMA TAIL

IV.1 INTRODUCTION.

The formation and morphology of a cometary plasma tail is jointly controlled by the prevalent conditions in the solar wind and the production of ions in the coma. Section IV.2 contains a review of current knowledge (based on both observation and theory) of the solar wind and the associated Interplanetary Magnetic Field (IMF). Large-scale images of Halley's plasma tail are analysed in Section IV.3 to determine the velocity field of the solar wind and a comparison is drawn with data measurements performed in-situ by spacecraft. Section IV.4 outlines the current understanding of the physical

structure of cometary magnetotails. This picture is used in Section IV.5, in which a series of Schmidt plates with high spatial and time resolution are analysed in order to derive the velocities of discrete structures within the ion tail itself. The conclusions resulting from this work are discussed with reference to both present and future work in the final part of this chapter, Section IV.6.

IV.2 THE SOLAR WIND AND THE IMF.

The solar wind is a flux of ions that is continually expelled from the sun as a form of minor stellar mass-loss. It is composed primarily of protons and electrons, with He^+ being the next most abundant species. Basic observed parameters are tabulated in Table IV.1.

As already mentioned in chapter I, the idea of a continuous outflow of material from the sun was first put forward by Biermann (1951) from his study of type I (ionic) comet tails. It was Parker (1958) who first calculated a theoretical model of a continuously outflowing solar wind. The plasma flowed outwards from the sun as a natural consequence of the large temperature gradient. This model, although containing a number of assumptions, can give both the correct boundary conditions (such as zero pressure at infinity) and reproduced the observed (via comet tails) mean velocity W_{sw} of $\sim 300 - 400$ km s^{-1} . Unfortunately, in the early models the deduced density was ~ 100 times larger than that actually observed.

The detailed theory of the solar wind was subsequently improved by a number of authors. Chamberlain (1961) integrated an energy equation into the model and found that both Parkers solution, and that of a ‘solar breeze’ ($W_{sw} \sim 20$ km s^{-1}), were possible. Other refinements include the effects of viscosity (Meyer and Schmidt, 1967) and the fact that the solar wind is largely a two component plasma of protons and electrons (Hartle and

Radial velocity $W_{sw}(r)$	400 km s^{-1}
Electron density n	$6.5 \times 10^6 \text{ m}^{-3}$
Electron temperature T_{elec}	$2 \times 10^5 \text{ K}$
Proton temperature T_{prot}	$5 \times 10^4 \text{ K}$
IMF field strength $ \mathbf{B} $	6 nT
Alfven speed V_A	60 km s^{-1}

Table IV.1: Average physical parameters observed in the solar wind.

Sturrock, 1968). Successively detailed studies have brought into line the theoretical models with the observed nature of the solar wind.

In his work, Parker realised that a continuously outflowing solar wind would affect the gross structure of the IMF. The time taken for the magnetic field to diffuse through a plasma a distance l is given by;

$$\tau(diff) = 4\pi\sigma l^2 \quad (\text{IV.1})$$

whereas the time taken for the field to be transported through that distance by bulk motion is given by:

$$\tau(trans) = l/W_{sw} \quad (\text{IV.2})$$

Dividing (IV.1) by (IV.2) gives the magnetic Reynolds number R_M as

$$R_M = 4\pi\sigma l W_{sw} \quad (\text{IV.3})$$

For typical velocities in the solar wind (see Table IV.1) R_M is very large. This is equivalent to saying that the IMF is carried along by the plasma; the

field is ‘frozen-in’. The radially outflowing plasma draws the field lines out into an Archimedian spiral, because the ‘feet’ of the lines are fixed on the rotating solar surface. The angle ψ the field lines make with the anti-solar direction is given by

$$\tan \psi = \frac{(R_h - R_{h_0})\Omega}{W_{sw}} \quad (\text{IV.4})$$

where R_h and R_{h_0} are the radii at which the observer and the solar surface lie, and Ω is the angular velocity of the sun. For $W_{sw} = 400 \text{ km s}^{-1}$ at 1AU, $\psi \simeq 45^\circ$. This simple picture has been observed to be correct to heliocentric distances of 8.5 AU by spacecraft (Smith, 1979).

Theoretical models of the solar wind including the solar magnetic field give higher outflow velocities than without the magnetic field. This is because of more efficient conversion of total flux energy to kinetic energy, through the damping of thermal conductivity transverse to the field lines at large heliocentric distances. More importantly, close to the sun the magnetic field is strong enough and W_{sw} is low enough to allow the magnetic field to impart angular momentum to the solar wind. This occurs whilst the outflow speed of the plasma is less than the Alfvén speed V_A , given by

$$V_A = \frac{B}{\sqrt{4\pi\rho}} \quad (\text{IV.5})$$

From data gathered from the Helios spacecraft, this occurs at roughly $12R_\odot$ (Priest, 1984a). Early theoretical studies of this by Weber and Davis (1967) gave the azimuthal velocity component $W_{sw}(\phi)$ as $\sim 1 \text{ km s}^{-1}$. Subsequent

inclusion of viscous forces by the same authors (1970) gave a much larger velocity component at 1 AU of $W_{sw}(\phi) = 6 \text{ km s}^{-1}$. This is more in line with the values deduced from spacecraft and comet studies of 8 km s^{-1} and 7 km s^{-1} respectively. However the theoretical value of $W_{sw}(\phi)$ is extremely sensitive to both the assumed form of $W_{sw}(R_h)$ and the proton temperature $T_p(R_h)$, and a certain amount of 'fine-tuning' is required in the models to reproduce the observed values.

IV.3 THE ION TAIL OF P/HALLEY AND THE SOLAR WIND.

IV.3.1 Introduction.

An important assumption in ion tail theory is that the overall morphology of the tail is controlled by the ambient solar wind conditions. The IMF is draped over the cometary ionosphere to create a magnetic channel down which the pick-up ions flow to form the tail. Thus the tail of a comet acts as a 'windsock' (See subsection I.5.2). Previously this fact has been used to probe the solar wind velocity field. In this section a similar analysis is performed on large-scale images of the plasma tail, in light of the *in - situ* measurements made by spacecraft during the apparition.

The fundamental observed datum is the position angle of the comets plasma tail as it appears projected on the sky for a particular position of the cometary head relative to the sun. The most thorough survey of this undertaken in the past was that of Belton and Brandt (1966), who catalogued ~ 1600 tail position angles of various comets. More recent studies have concentrated on particular comets with good photographic and imaging coverage over the apparition. These have included Comet Kohoutek 1973 XII (Jockers, 1985) and of course Comet P/Halley (Celnik and Schmidt-Kaler, 1987).

IV.3.2 Observations

A total of 39 plates showing Halley's plasma tail were obtained by the United Kingdom Schmidt Telescope during the 1985/86 apparition. A full description of the 1.2-m Schmidt can be found in the UKSTU handbook (1983). The majority of the plates used in this study were obtained specifically for the Comet Halley United Kingdom Co-ordinating committee. These images were obtained using a combination of Eastman Kodak IIA-O emulsion and a GG 395 Schott glass broadband filter. This emulsion/filter combination (hereafter referred to as 'JB') restricts transmittance to the wavelength region 3850Å to 5000Å. The brightest fluorescence lines of the CO⁺ (A²π_i - X²Σ⁺) transitions are the (3-0) bands at 4000Å and the (2-0) bands at 4260Å (Magnani and A'Hearn, 1986). JB plates are therefore well suited to studying the CO⁺ ions observed in cometary plasma tails. Unfortunately this bandpass also includes the strong C₂ (d³π_g - a³π_u) bands around 4650Å. So detection of plasma features in the inner coma is exceedingly difficult because of the large amount of C₂.

The other plates showing CO⁺ ions were those with IIA-O emulsion and a GG 385 filter ('B' plates) and IIIa-J emulsion with a GG395 filter ('J' plates). With FWHM bandwidths of ~ 1000Å and ~ 1500Å respectively, there is greater contamination on the J plates from both neutral species and continuum. The contamination by reflected solar radiation is particularly

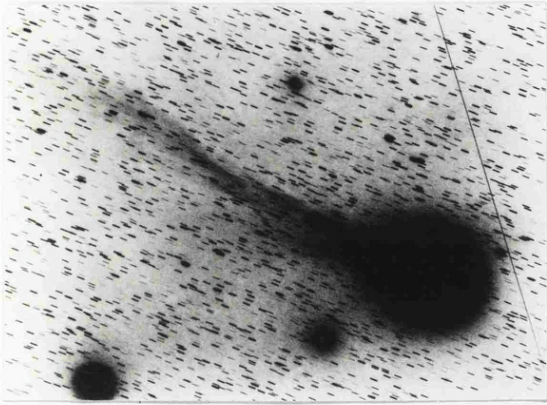
important when the dust tail appears close to the plasma tail as projected on the plane of the sky. The JB plates were used in preference to the B plates due to the higher sensitivity of the former.

It should be noted that plasma tail features are also visible on 'R' type Schmidt plates. These have a maximum transmittance at around 6700\AA and a FWHM of $\sim 500\text{\AA}$. These features are probably attributable to H_2O^+ emission from the $(\tilde{A}^2A_1 - \tilde{X}^2B_1)$ bands at 7000\AA . The ion tail can only be traced a short distance from the coma, probably because H_2O has a shorter lifetime than CO (Eberhardt *et al.*, 1987).

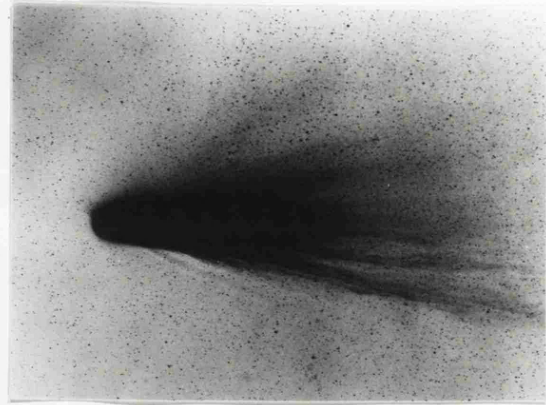
Table IV.2 lists all the UKSTU plates used in the following analysis. Note that some plates exist that were not used due to flaws or unavailability. Of the 11 plates taken on the night of 15th April only the first and last plates are contained in this study (see section IV.5 for a full analysis of these plates). Three plates taken after JB11065 were not used due to confusion between the fading plasma tail and the relatively bright dust tail. Six of the images studied are reproduced in plate IV.1.

IV.3.3 Analysis.

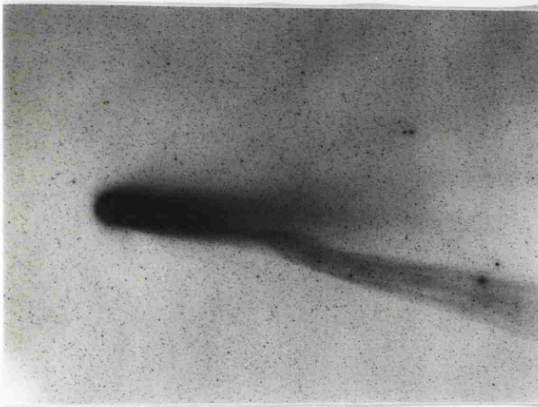
The primary aim is to derive the position vector of the expected tail direction in the plane of the sky, and to compare with that actually observed. This has to be calculated by using an assumed velocity field of the solar wind.



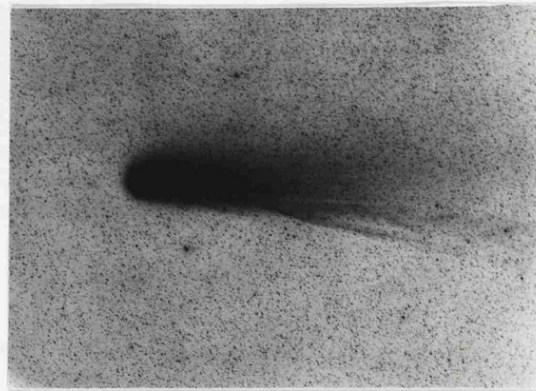
B10578



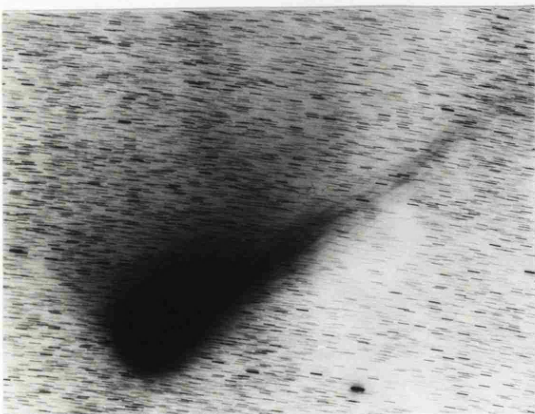
B10800



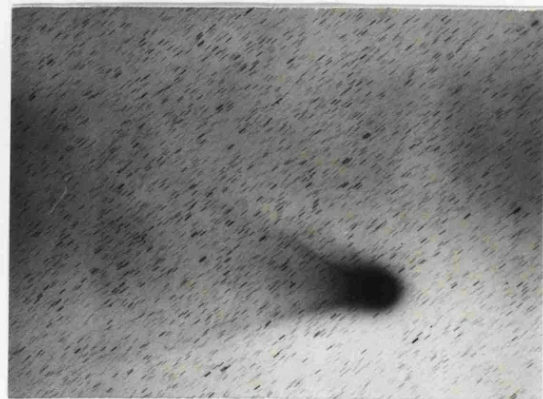
JB10879



JB10921



JB10998



JB11065

Plate	Date	R_h (AU)	Δ (AU)	α (1950.0)	δ
JB10567	4/12/85	1.431	0.660	0h 31.466m	+10° 50.52'
B10578	9/12/85	1.355	0.726	23h 50.543m	+07° 03.78'
B10800	4/3/86	0.771	1.185	20h 19.936m	-17° 43.03'
B10803	5/3/86	0.784	1.163	20h 18.147m	-18° 06.32'
J10822	9/3/86	0.840	1.067	20h 10.235m	-19° 51.50'
JB10829	10/3/86	0.854	1.044	20h 08.195m	-20° 18.94'
J10831	10/3/86	0.855	1.042	20h 10.112m	-20° 14.08'
JB10879	17/3/86	0.958	0.867	19h 50.029m	-24° 19.62'
JB10887	18/3/86	0.973	0.843	19h 46.914m	-24° 59.34'
JB10896	19/3/86	0.989	0.817	19h 43.315m	-25° 44.48'
JB10913	21/3/86	1.019	0.766	19h 35.482m	-27° 19.62'
JB10921	23/3/86	1.050	0.716	19h 26.259m	-29° 05.98'
JB10925	24/3/86	1.066	0.691	19h 23.069m	-30° 00.97'
JB10973	3/4/86	1.219	0.480	17h 43.342m	-42° 29.83'
JB10982	4/4/86	1.235	0.465	17h 25.900m	-43° 48.48'
JB10986	5/4/86	1.250	0.451	17h 05.930m	-45° 02.22'
JB10998	7/4/86	1.281	0.431	16h 21.079m	-46° 50.68'
JB11019	10/4/86	1.328	0.417	15h 01.887m	-47° 09.87'
JB11035	14/4/86	1.389	0.437	13h 25.622m	-42° 31.06'
JB11037	15/4/86	1.400	0.444	13h 11.409m	-41° 16.62'
JB11047	15/4/86	1.405	0.448	13h 05.583m	-40° 43.11'
JB11049	17/4/86	1.433	0.475	12h 34.451m	-37° 12.89'
JB11058	19/4/86	1.464	0.512	12h 07.531m	-33° 23.64'
JB11059	19/4/86	1.465	0.512	12h 07.018m	-33° 18.52'
JB11065	20/4/86	1.480	0.533	11h 56.058m	-31° 30.84'

Table IV.2: Heliocentric distance, geocentric distance and celestial positions of Comet Halley for the plates used in this study.

Figure IV.1: Definition of vectors $\mathbf{L}, \mathbf{M}, \mathbf{N}$ and the angle μ .

A reference frame for calculating unit velocity and position vectors in the sky plane have been defined by Finson and Probst (1968). \mathbf{L} is the unit vector pointing from the comet towards Earth, \mathbf{M} is the anti-solar direction projected onto the sky. The \mathbf{N} axis then completes a right-handed co-ordinate system with the other two. Jockers (1985, and references therein) described fully the process for calculating the relevant tail-direction vectors in this co-ordinate system and his procedure was used in this work.

As the simplest model of the solar wind has its axis of symmetry in the solar equatorial system, one needs to first transform the ecliptic elements of the comet orbit and the positions of the comet and Earth into this frame of

reference.

$$\omega_c^s = \omega_c^e - \arctan \left[\frac{\sin(\Omega_c^e - \Omega_\odot)}{-\cos i_c^e \cos(\Omega_c^e - \Omega_\odot) + \frac{\sin i_c^e}{\tan i_\odot}} \right] \quad (\text{IV.6})$$

$$\Omega_c^s = \arctan \left[\frac{\sin(\Omega_c^e - \Omega_\odot)}{-\cos i_\odot \cos(\Omega_c^e - \Omega_\odot) - \frac{\sin i_\odot}{\tan i_c^e}} \right] \quad (\text{IV.7})$$

$$\cos i_c^s = \cos i_\odot \cos i_c^e + \sin i_\odot \sin i_c^e \cos(\Omega_c^e - \Omega_\odot) \quad (\text{IV.8})$$

$$\sin \theta^s = \cos i_\odot \sin \theta^e - \sin i_\odot \cos \theta^e \sin(\phi^e - \Omega_\odot) \quad (\text{IV.9})$$

$$\phi^s = \arctan \left[\frac{\sin i_\odot \tan \theta^e + \cos i_\odot \sin(\phi^e - \Omega_\odot)}{\cos(\phi^e - \Omega_\odot)} \right] \quad (\text{IV.10})$$

Here $\arctan[X/Y]$ is chosen so that the signs of X and Y satisfy the condition $\arctan[\sin(a)/\cos(a)] = a$ for $0 < a < 2\pi$. The subscript 'c' refers to the comets orbital elements. Superscripts e and s refer to the solar ecliptical and solar equatorial systems respectively. From now on the equatorial system is used.

The angles μ and γ are introduced. These are used to project the heliocentric spherical polar vectors $\hat{\mathbf{r}}, \hat{\boldsymbol{\theta}}, \hat{\boldsymbol{\phi}}$ onto the sky M,N plane. They are shown in figures IV.1 and IV.2. μ defines the angle between M and the anti-solar vector $\hat{\mathbf{r}}$, the sense being given by $\mathbf{L} \cdot \hat{\mathbf{r}} < 0$ meaning μ is positive. The angle γ is the angle between $\hat{\boldsymbol{\phi}}$ and N, turning around $\hat{\mathbf{r}}$.

$$\sin \mu = \frac{R_h^2 + \Delta^2 - \rho_\oplus^2}{2R_h\Delta} \quad (\text{IV.11})$$

$$\gamma = \arctan \left[\frac{\sin(\phi_\oplus - \phi_c)}{\tan \theta_\oplus \cos \theta_c - \sin \theta_c \cos(\phi_\oplus - \phi_c)} \right] \quad (\text{IV.12})$$

In the expression defining μ , ρ_\oplus is the heliocentric distance of the Earth,

Figure IV.2: Definition of the angle γ .

whilst the other symbols have their usual meanings. With these angles, the transformation of $\hat{\mathbf{r}}, \hat{\theta}, \hat{\phi}$ into $\mathbf{L}, \mathbf{M}, \mathbf{N}$ is as follows:

$$\begin{aligned}\hat{\mathbf{r}} &= -\mathbf{L} \sin \mu + \mathbf{M} \cos \mu \\ \hat{\theta} &= \mathbf{L} \cos \mu \cos \gamma + \mathbf{M} \sin \mu \cos \gamma - \mathbf{N} \sin \gamma \\ \hat{\phi} &= \mathbf{L} \cos \mu \sin \gamma + \mathbf{M} \sin \mu \sin \gamma + \mathbf{N} \cos \gamma\end{aligned}\tag{IV.13}$$

Figure IV.3 shows these unit vectors projected on the sky for several of the plates. Thus a model solar wind $W_{sw}(r, \theta, \phi)$ may be projected onto the comets position in the sky.

The form of the field used was that given by Brandt (1973).

$$W_{sw}(r) = \text{constant}$$

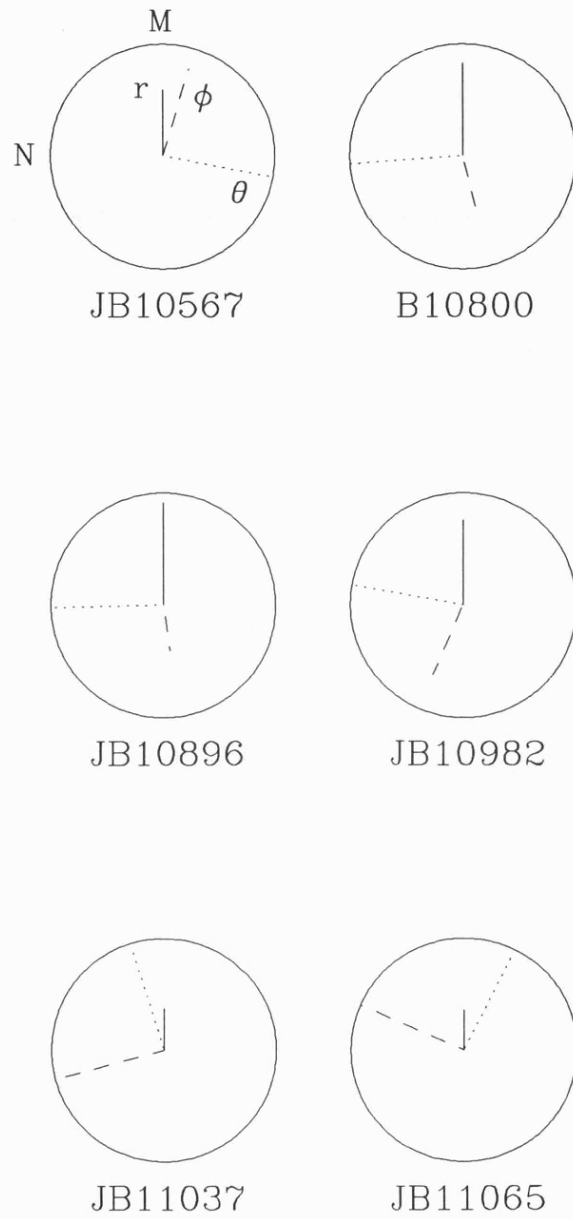


Figure IV.3: Unit solar equatorial vectors projected on the sky (**M,N**) plane for six of the plates studied.

$$W_{sw}(\phi) = W_{\phi_0} \frac{(\cos b)^{2.315}}{r}$$

$$W_{sw}(\theta) = W_m \sin 2b$$

The constants $W_{sw}(\phi)$ and $W_{sw}(\theta)$ were taken to be 6.7 km s^{-1} and 2.3 km s^{-1} respectively. From published spacecraft measurements (Oyama *et al.*,1986), the flow speed varied from 400 to 600 km s^{-1} over the apparition of the comet . Table IV.3 lists the theoretical aberration angles of the plasma tail in all the plates studied for $W(r)$ components in this range. For most viewing geometries and orbital positions the $W_{sw}(r)$ term is dominant, being $\sim 10^2$ larger than the other velocity components.

The ‘windsock’ equation governing the tail vector \mathbf{T} is given by

$$\mathbf{T} = \mathbf{W}_{sw} - \mathbf{V}_c \tag{IV.14}$$

where \mathbf{V}_c is the velocity vector of the comet. Again \mathbf{V}_c needs to be expressed in the L,M,N co-ordinate system. The easiest way to do this is by splitting the comets’ velocity into components parallel and perpendicular to the sun-comet line. The corresponding unit vectors are $\hat{\mathbf{r}}$ and $\hat{\boldsymbol{\eta}}$, which points in the direction opposite to the cometary motion and perpendicular to $\hat{\mathbf{r}}$ (Finson and Probst,1968). $\hat{\boldsymbol{\eta}}$ can be defined using the angles already introduced and λ , which is the angle between the comets’ transverse heliocentric velocity

Figure IV.4: Definition of the angle λ .

and $\hat{\phi}$. λ is shown in figure IV.4, and is defined by:

$$\sin \lambda = \sin i_c \cos(\phi_c - \Omega_c) \quad (\text{IV.15})$$

$\hat{\eta}$ is thus given as:

$$\hat{\eta} = -\mathbf{L} \cos \mu \sin(\gamma + \lambda) - \mathbf{M} \sin \mu \sin(\gamma + \lambda) + \mathbf{N} \cos(\gamma + \lambda) \quad (\text{IV.16})$$

The components V_r , V_θ and V_ϕ of the cometary velocity are given by:

$$\mathbf{V}_c = V_{\parallel} \hat{\mathbf{r}} + V_{\perp} \cos \lambda \cdot \hat{\phi} + V_{\perp} \sin \lambda \cdot \hat{\theta} \quad (\text{IV.17})$$

V_{\parallel} and V_{\perp} are the components of \mathbf{V}_c parallel and perpendicular to $\hat{\mathbf{r}}$. For

Halley, these can be calculated from

$$V_{\perp} = \frac{32.0051}{R_h} \text{ km s}^{-1} \quad (\text{IV.18})$$

$$V_{parallel} = \frac{32.0051}{R_h} \sqrt{\left(\frac{R_h}{0.5871} - 1\right) (1 - 0.0283R_h)} \quad (\text{IV.19})$$

The measured quantity is the angle the tail makes with the radial vector \hat{r} .

This aberration angle ε is defined as

$$\tan \varepsilon = \frac{-\mathbf{T} \cdot \mathbf{N}}{\mathbf{T} \cdot \mathbf{M}} \quad (\text{IV.20})$$

As the cometary velocity components are calculated from orbital mechanics, the unknown quantity in equation (IV.14) is the solar wind velocity field. Values of $W_{sw}(r, \theta, \phi)$ may be inserted into (IV.14) to give \mathbf{T} , which then produces a value of ε that may be compared with the observed aberration angle.

The measurement of the actual aberration angle was relatively straightforward on the majority of the plates. The STARLINK software package CHART was used to produce a hard copy of the field 2° across containing the comet, with the calculated position of the nucleus marked. This was then used in conjunction with the relevant film copy on which the tail direction could be measured. This was the stage which produced most errors, as the comet tail in most images was both highly structured and often showed kinks in the tail direction. It was therefore decided that the tail vector \mathbf{T} would be measured as close to the coma as possible, using the apparent axis of symmetry as the tail axis. This distance was always $< 2 \times 10^6$ km and in most cases closer than 10^6 km. Thus the aberration angle measured re-

Plate	$\varepsilon(\text{theo})$			$\varepsilon(\text{obs})$
	400 km s ⁻¹	500 km s ⁻¹	600 km s ⁻¹	
JB10567	0.58°	0.46°	0.39°	1.3 ± 1.0°
B10578	0.57°	0.45°	0.38°	-0.1 ± 1.0°
B10800	2.25°	1.75°	1.43°	3.4 ± 1.0°
B10803	2.17°	1.68°	1.38°	1.3 ± 1.0°
J10822	1.94°	1.51°	1.23°	1.6 ± 1.0°
JB10829	1.90°	1.48°	1.21°	2.9 ± 1.0°
J10831	1.90°	1.48°	1.21°	2.7 ± 1.0°
JB10879	1.81°	1.42°	1.16°	2.5 ± 1.0°
JB10887	1.82°	1.42°	1.17°	2.6 ± 1.0°
JB10896	1.83°	1.43°	1.18°	1.7 ± 1.0°
JB10913	1.88°	1.47°	1.21°	2.5 ± 1.0°
JB10921	1.95°	1.52°	1.25°	1.7 ± 1.0°
JB10925	2.00°	1.56°	1.28°	2.3 ± 1.0°
JB10973	3.16°	2.46°	2.02°	2.5 ± 1.0°
JB10982	3.44°	2.68°	2.19°	-0.8 ± 1.0°
JB10986	3.77°	2.93°	2.40°	5.2 ± 1.0°
JB10998	4.66°	3.62°	2.96°	2.6 ± 1.0°
JB11019	6.91°	5.38°	4.40°	8.9 ± 1.0°
JB11035	10.45°	8.23°	6.79°	12.3 ± 1.0°
JB11037	10.79°	8.54°	7.06°	8.6 ± 1.0°
JB11047	10.83°	8.59°	7.11°	9.4 ± 1.0°
JB11049	10.02°	8.02°	6.69°	2.2 ± 1.0°
JB11058	8.23°	6.63°	5.55°	9.4 ± 1.0°
JB11059	8.05°	6.48°	5.42°	7.3 ± 1.0°
JB11065	7.46°	6.02°	5.05°	7.7 ± 1.0°

Table IV.3: Theoretical and observed aberration angles of the ion tail.

lates to the solar wind at the comet less than 1.4 hours previously (assuming $W_{sw} = 400 \text{ km s}^{-1}$). The error in each measurement of the aberration angle ϵ was judged to be $\leq \pm 1.0$ degrees.

IV.3.4 Results.

The measured aberration angles ϵ are given in table IV.3 alongside those calculated theoretically. Clearly, for the majority of plates studied, the standard model of the solar wind can reproduce the tail direction within the measurement errors. This is shown more clearly in figure IV.5, in which the observed aberration angles are plotted against those calculated for a radial component of the solar wind of $W_{sw}(r) = 400 \text{ km s}^{-1}$. The form of figure IV.5 supports the work of Celnik and Schmidt-Kaler (1987). They proposed that an average decrease then increase in the aberration angle between February 22nd and early April 1986 could be due to projection effects.

Previous authors have observed that at times of solar minimum there appears to be a strong solar latitudinal dependence of $W_{sw}(r)$ on the order of $10 \text{ km s}^{-1} \text{ degree}^{-1}$ from the solar equator. The observations here span the latitude range $7.5^\circ > b > -15.5^\circ$. The maps of Kozima and Kakinuma (1987) illustrate the average solar wind speed in 1985 as projected onto the solar disk. The mean speed increases above 400 km s^{-1} for $|b| > 15^\circ$. It is not surprising then that the majority of the tail vectors observed can be

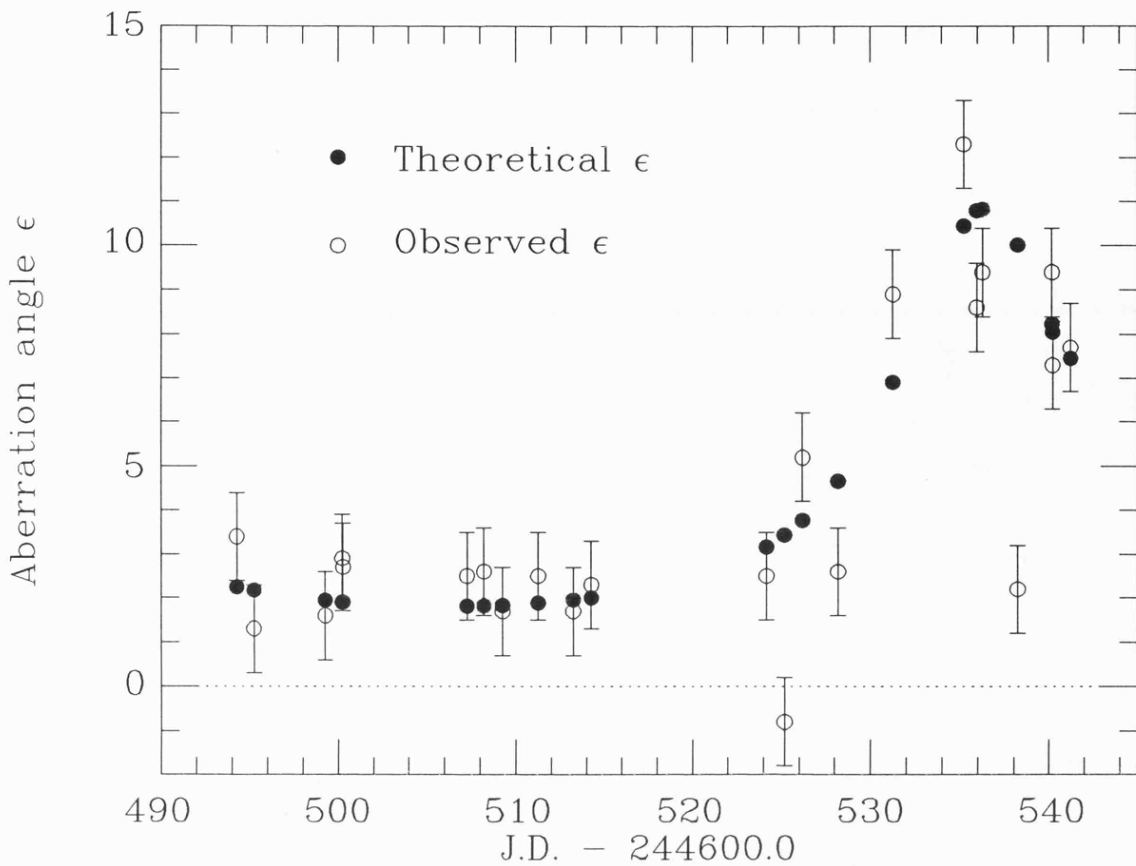


Figure IV.5: The variation of theoretical ($W_{sw}(r) = 400 \text{ km s}^{-1}$) and observed aberration angles.

explained with $W_{sw}(r) = 400 \text{ km s}^{-1}$. The few images studied not well represented by assuming $400 \text{ km s}^{-1} < W_{sw}(r) < 600 \text{ km s}^{-1}$ are discussed individually:

In image JB10982 there is some confusion with the background Milky-Way, and together with a faint plasma tail the error of measurement is certainly larger than 1° . If the aberration angle measured is correct, then there must exist a large polar component of the solar wind directed towards the solar equatorial plane. This would have to be in excess of 17 km s^{-1} assuming $W_{sw}(r) < 600 \text{ km s}^{-1}$, even though the comet was only 12° below the solar equator. This scenario is highly unlikely, implying an error in the

measurement of ε

Both plates JB10986 and JB11019 can have the observed aberration angle accounted for by allowing $W_{sw}(r) < 400 \text{ km s}^{-1}$. The resulting radial velocities of the solar wind are $W_{sw}(r) = 325 \text{ km s}^{-1}$ and $W_{sw}(r) = 350 \text{ km s}^{-1}$ respectively. Such velocities have often been observed, and indeed was the solar wind velocity prior to the Giotto encounter with Halley (Coates *et al.*, 1987).

JB11049 is a more interesting case. This measurement of $\varepsilon(\text{obs}) = 2.2 \pm 1.0^\circ$ is certainly the most bewildering of all the observations. Re-measurement of the plate gave the same value for the aberration angle within the errors. This is not surprising as the tail appears as a well defined sheet of plasma rather than being composed of individual streamers as on most occasions. The measurement of ε by Celnik and Schmidt-Kaler (1987) on the night of 17th April is $3.9 \pm 1.0^\circ$, confirming the value observed here. A radial component of $W_{sw}(r) = 1500 \text{ km s}^{-1}$ would be required to produce $\varepsilon = 2.9^\circ$, considerably larger than the highest speeds ever recorded of $\sim 900 \text{ km s}^{-1}$.

From figure IV.3, it was around this date that the tail vector was most sensitive to variations in $W_{sw}(\theta)$ and $W_{sw}(\phi)$, as the comet was in opposition. Using $W_{sw}(r) = 400 \text{ km s}^{-1}$, the influence of differing values of $W_{sw}(\phi)$ and $W_{sw}(\theta)$ was investigated. Assuming the $W_{sw}(\theta)$ component to be dominant, a poleward component of $\sim 150 - 200 \text{ km s}^{-1}$ would be required! Velocities

of this magnitude have never been observed in the equatorial plane.

Conversely, assuming $W_{sw}(\theta)$ to be negligible requires that $W_{sw}(\phi) = -16$ km s⁻¹. Such an azimuthal component would give an aberration angle of $\varepsilon = 1.9^\circ$, agreeing with that observed. The latter seems to be the most plausible explanation of the observed tail vector. The negative value however implies that solar wind flow is directed against the solar rotation. This may occur when a high-speed solar wind stream intersects the normal low velocity component. As described by Siscoe, Goldstein and Lazarus (1969), such a stream develops a high density ($n'/n \geq 3$) shock front, behind which the plasma flow is deviated against the solar rotation. Fulle and Pansecchi (1984) observed a very similar effect in Comet Austin 1983g, noting discontinuities and 'tail-wagging' that seemed to be produced by changes in $W_{sw}(\phi)$. They too attributed this to the intersection of the comet with high-velocity flows.

IV.4 MAGNETOTAIL STRUCTURE.

The field-line draping model of Alfvén (1957) was dramatically confirmed by the passage of the ICE spacecraft through the near-magnetotail of Comet P/Giacobinni-Zinner as reported by von Rosenhinge, Brandt and Farquahar (1986). However, the physical appearance of a cometary plasma tail is hardly that of a single uniform current sheet. A well developed ion tail generally displays such features as condensations, kinks, streamers and the mysterious tail rays. Indeed, before the ICE encounter there was no firm evidence that the observed ion tail is the optical manifestation of the central current sheet (Slavin *et al.*, 1986).

Two points must be borne in mind in the following work. Of all the six spacecraft to approach Halley in the Spring of 1986, not one passed through the magnetotail. ICE itself passed only 7800 km downstream of the nucleus of Comet Giacobini-Zinner. Our primary sources of knowledge about conditions in the distant plasma tail are ground-based observations and theoretical models. Secondly, it is assumed that the motions of plasma features downtail are true bulk motions, and not Alfvénic density waves. This view was substantiated in Chapter I.

To demonstrate the global aspects of the ion tail an analytical expression for the field-line morphology was sought, using the **B**-field given by Ip (1980) as a starting point. This can then be used to illustrate the results from ICE.

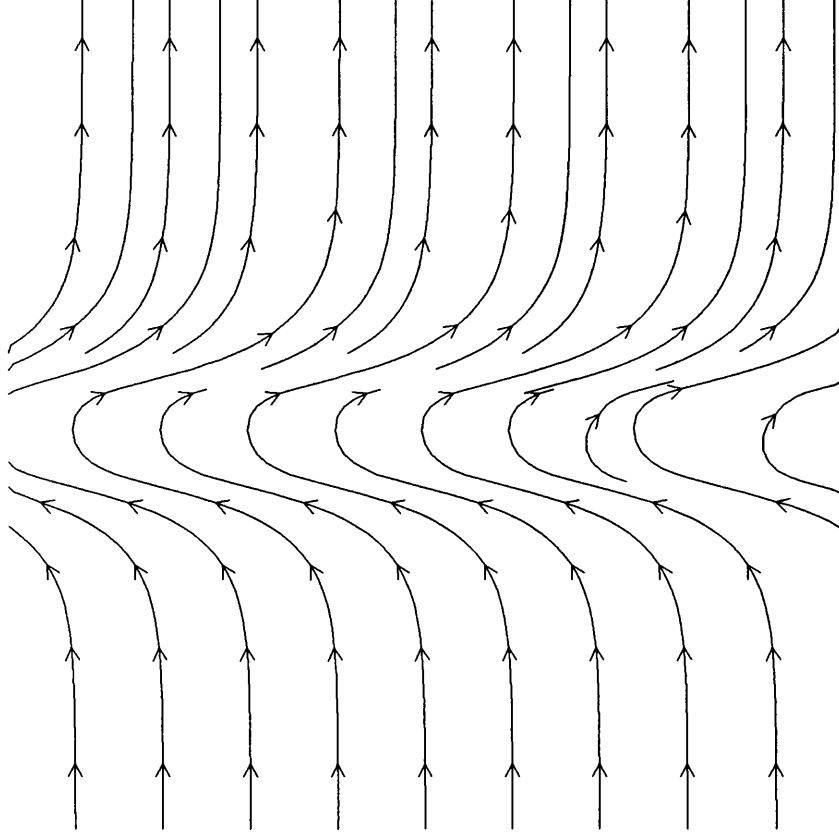


Figure IV.6: Magnetic field lines as given by equation IV.21. Apparent truncation of field lines was caused by the plotting program.

Expression IV.21 was eventually found by comparison with the field-line model presented by Kimmel *et al.* (1987).

$$\mathbf{B} = 2B_{y0} \sec\left(\frac{z}{z_0}\right) \tanh\left(\frac{z}{z_0}\right) \hat{\mathbf{y}} + B_{z0}(1 + \alpha e^{-y/y_0}) \hat{\mathbf{z}} \quad (\text{IV.21})$$

As it includes the effect of $B_y \rightarrow 0$ outside the tail lobes, this field-line configuration is more realistic than that derived by Ip (1980). The form of the captured IMF field lines is as shown in figure IV.6.

The sun lies in the $-y$ direction, and the field lines lie in the y - z plane. B_{y0} represents the maximum field strength in the tail lobes, while B_{z0} is the ambient solar wind field strength reached as $y \rightarrow \infty$. The decaying

exponential form of the \hat{z} component represents the bunching of the field lines near the nucleus. The constant α dictates the strength of the piled up field at the nucleus. As ICE measured the field strength to be only 5nT at $z = 0$, $y = 7800$ km, this bunching is presumed to be important only near the nucleus. Thus a value of 1 is assumed for α . Finally z_0 gives a measure of the width of the current sheet.

The Lorentz force on the ions may be calculated from (*e.g.* Priest, 1984b)

$$\mathbf{J} \times \mathbf{B} = (\nabla \times \mathbf{B}) \times \frac{\mathbf{B}}{\mu} = (\mathbf{B} \cdot \nabla) \frac{\mathbf{B}}{\mu} - \nabla \left(\frac{B^2}{2\mu} \right) \quad (\text{IV.22})$$

The last equality demonstrates that the Lorentz force may be considered as the sum of two separate terms, a magnetic tension lying along the field lines and a magnetic pressure force perpendicular to the field direction. The y component of the Lorentz force may be calculated from (IV.21) and (IV.22) to give

$$\begin{aligned} (\mathbf{J} \times \mathbf{B})_y &= \frac{1}{\mu_0} \left(\frac{\partial B_y}{\partial z} - \frac{\partial B_z}{\partial y} \right) B_z \\ &= \frac{B_{z_0}}{\mu_0} \left(1 + e^{-y/y_0} \right) \\ &\quad \left\{ \frac{2B_{y_0}}{z_0} \left[\text{sech}^3\left(\frac{z}{z_0}\right) - \tanh^2\left(\frac{z}{z_0}\right) \text{sech}\left(\frac{z}{z_0}\right) \right] + \frac{B_{z_0}}{y_0} e^{-y/y_0} \right\} \end{aligned} \quad (\text{IV.23})$$

For $B_{y_0} = 50\text{nT}$ and $z_0 = 1000$ km (as measured at G-Z by ICE), a midtail force of $\sim 10^{-15}$ N m $^{-3}$ is derived at $y = 7800$ km with $y_0 = 10^5$ to 10^6 km. The Lorentz force downtail as a function of distance z from the center of the tail is shown in figure IV.7(a) for the parameters above. This may

be compared with figure 7 of McComas *et al.* (1987). The behaviour of the tailward Lorentz force as measured by ICE is well represented in both gross structure and magnitude by the simple model presented here.

Some confusion may occur over the fact that in the tail lobes the derived acceleration on the ions is towards the nucleus. This is the case in the frame of reference of the field lines. As these are being swept past the comet via the solar wind, this actually represents the draping of the field lines caused by the mass-loading of the plasma flow.

Wallis and Johnstone (1982) were first to investigate the motion of the individual pick-up ions in the large scale magnetic field. They solved the equation of motion as a function of the point of origin (i.e. the position in the coma where the neutral molecules are ionised). Their conclusion was that there are two favoured trajectories, a point well illustrated by the test particle paths calculated by Kimmel *et al.* (1987). Molecules ionised in the inner coma tend to be focused towards the tail-axis. Those ions created in the outer coma diverge from the tail. Again this can be understood from the B-field model given here. The cross-tail Lorentz force may be calculated as

$$\begin{aligned}
 (\mathbf{J} \times \mathbf{B})_z &= \frac{1}{\mu_0} \left(\frac{\partial B_z}{\partial y} - \frac{\partial B_y}{\partial z} \right) B_y \\
 &= -\frac{2B_{y0}}{\mu_0} \operatorname{sech}\left(\frac{z}{z_0}\right) \tanh\left(\frac{z}{z_0}\right) \\
 &\quad \left[\frac{B_{z0}}{y_0} e^{-y/y_0} + \frac{2B_{y0}}{z_0} \left\{ \operatorname{sech}^3\left(\frac{z}{z_0}\right) - \tanh^2\left(\frac{z}{z_0}\right) \operatorname{sech}\left(\frac{z}{z_0}\right) \right\} \right]
 \end{aligned}
 \tag{IV.24}$$

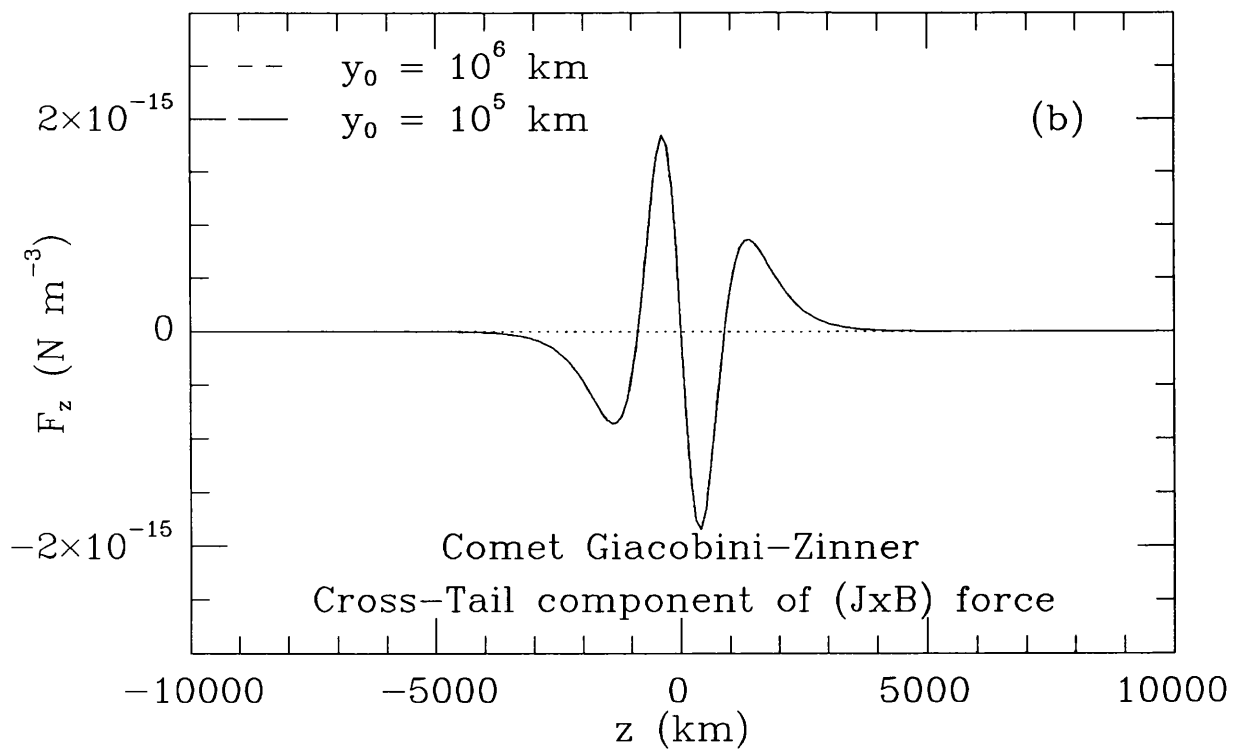
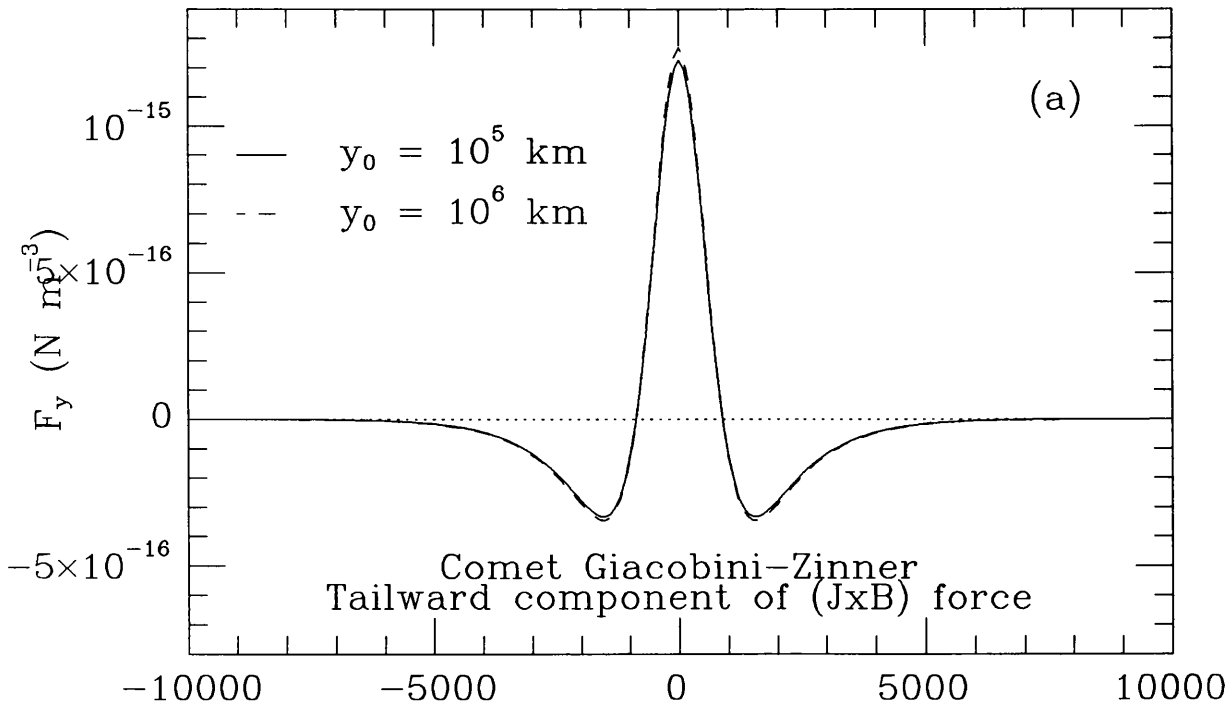


Figure IV.7: Lorentz force for ICE magnetotail parameters.

(a) Downtail force on ions. (b) Cross-tail force on ions.

$$\begin{aligned}
(\mathbf{J} \times \mathbf{B})_x &= \frac{1}{\mu_0}(\nabla \times \mathbf{B})_y B_z - \frac{1}{\mu_0}(\nabla \times \mathbf{B})_z B_y \\
&= 0
\end{aligned}
\tag{IV.25}$$

This is illustrated in figure IV.7(b). Within the inner-tail the curvature of the field lines acts always to accelerate the ions towards the centre ($z = 0$). However in the tail-lobes the magnetic pressure acts as to force the plasma away from the tail. As pointed out by Ershkovich, Niedner and Brandt (1982) in their analytical model, in reality the flaring of a cometary tail depends strongly on the pressure balance between the tail ions and the magnetic field.

Although not prominently noted before in the literature, this picture explains the basic morphological differences between the ion tails of short and long-period comets. Photographs of short-period comets that exhibit plasma tails tend to show them as narrow, well defined structures. This is due to the low production rate of the nucleus. For bright comets, the ion density in the outer coma is large enough so that the lobe structures start to become visible. A relevant example of this may be found by comparing a photograph of P/Giacobini-Zinner (Brandt *et al.*, 1988) with those of Halley shown in plate IV.1. It should not be supposed that this is the only possible explanation however. Another possibility is that the plasma tails of short-period comets are not dense enough to allow instabilities to form, which then may also play a part in widening the tail as described by Niedner, Ershkovich and Brandt (1983).

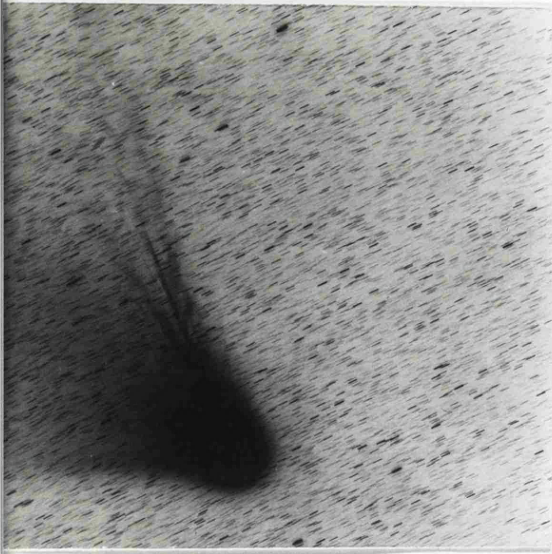
Plate	Time of Exposure (UT)	α (1950.0)	δ	$\epsilon(\text{obs})$
JB11037	11.09	13h 11.367m	$-41^{\circ} 15.13'$	$8.6 \pm 1.0^{\circ}$
JB11038	11.49	13h 10.850m	$-41^{\circ} 12.25'$	$8.0 \pm 1.0^{\circ}$
JB11039	12.58	13h 09.900m	$-41^{\circ} 07.12'$	$8.5 \pm 1.0^{\circ}$
JB11040	13.39	13h 09.367m	$-41^{\circ} 03.98'$	$9.1 \pm 1.0^{\circ}$
JB11041	14.22	13h 08.800m	$-41^{\circ} 00.73'$	$8.6 \pm 1.0^{\circ}$
JB11042	15.04	13h 08.233m	$-40^{\circ} 57.60'$	$9.1 \pm 1.0^{\circ}$
JB11043	15.52	13h 07.617m	$-40^{\circ} 54.00'$	$9.3 \pm 1.0^{\circ}$
JB11044	16.33	13h 07.067m	$-40^{\circ} 50.83'$	$10.2 \pm 1.0^{\circ}$
JB11045	17.16	13h 06.517m	$-40^{\circ} 47.65'$	$9.3 \pm 1.0^{\circ}$
JB11046	17.57	13h 05.983m	$-40^{\circ} 44.47'$	$9.2 \pm 1.0^{\circ}$
JB11047	18.38	13h 05.467m	$-40^{\circ} 41.38'$	$9.4 \pm 1.0^{\circ}$

Table IV.4: Plates taken on the night of 15th April 1986. Listed are the time of exposure, position of the nucleus and the observed aberration angle.

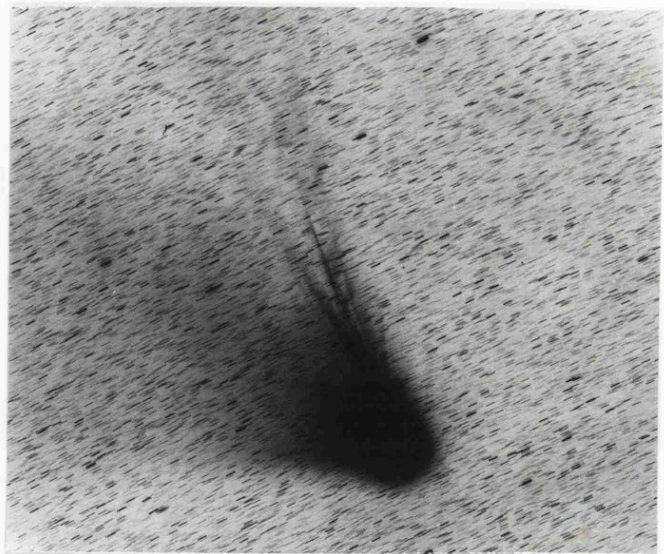
IV.5 THE VELOCITY FIELD IN THE ION TAIL.

IV.5.1 Observations.

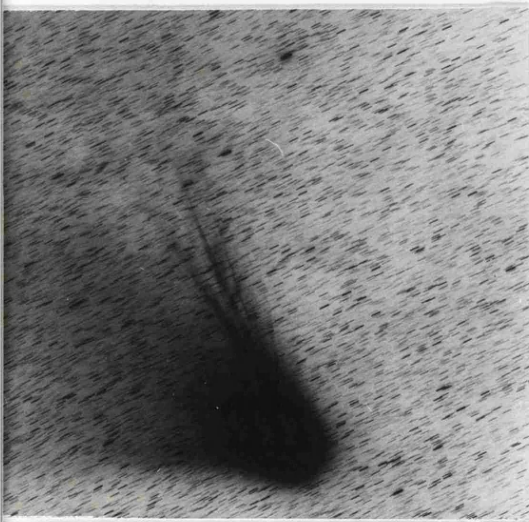
The United Kingdom Schmidt telescope (see section IV.2) was used to take a series of 11 JB plates on the night of the 15th April 1986. Each exposure was of duration 30 minutes except for JB11037 (29 minutes) and JB11047 (21 minutes). Table IV.4 lists the times of exposure of all the plates together with relevant geometric parameters. The position of the nucleus was calculated from an ephemeris generating computer program with an accuracy better



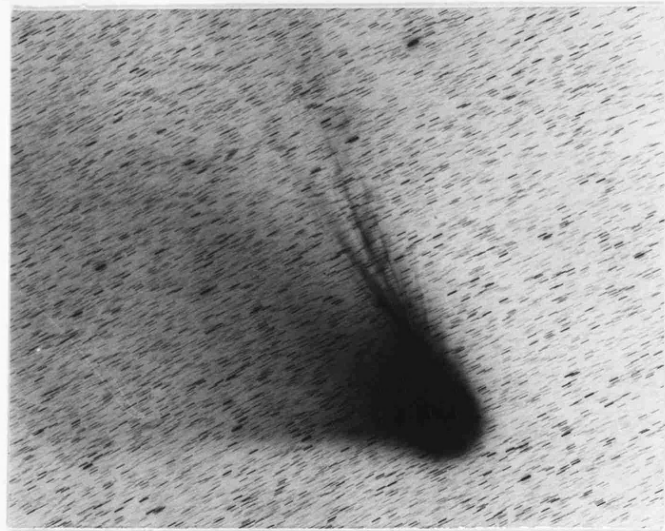
JB11037



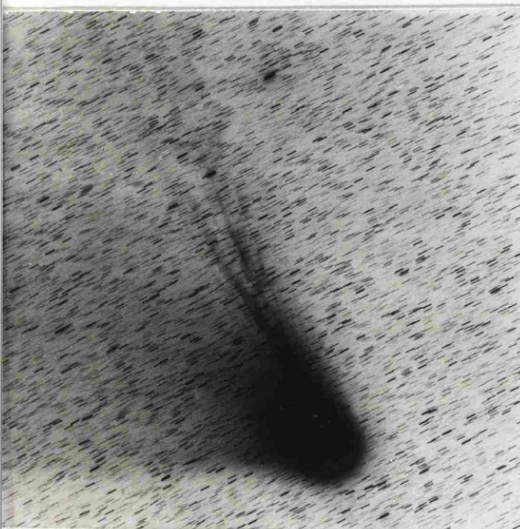
JB11039



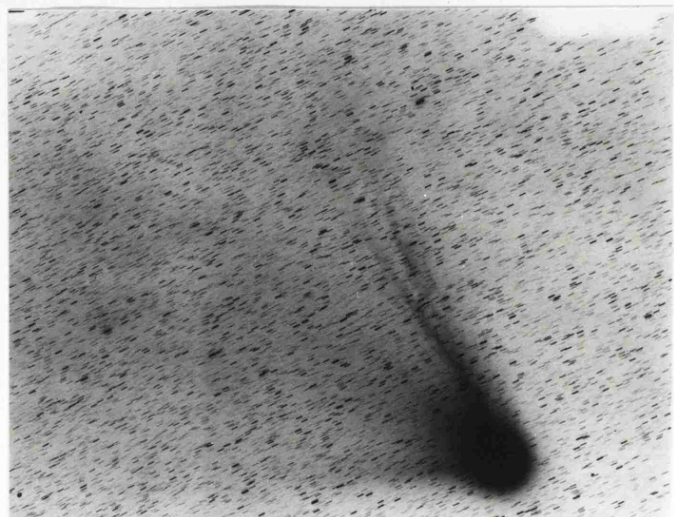
JB11041



JB11043



JB11045



JB11047

than 5 arcsec (S.F.Green, private communication). Position angles of the projected radius vector were calculated by hand.

At this time the comet was at a mean geocentric distance of 0.446 AU. Thus the plate scale of 1mm = 67.14 arcsec was equivalent to a linear dimension of 2.17×10^4 km at the head of the comet, and 2.37×10^4 km some 2° downtail (assuming the tail lies along the anti-solar vector). Six of these plates are shown in plate IV.2. The main formations in the ion tail consisted of a strong central streamer, with two bright streamers to the East and West joining the central feature at distances of $\sim 0.7^\circ$ and $\sim 1.7^\circ$ respectively. These streamers appeared 'clumpy', with many condensations within them. Upstream of the East streamer the main tail appeared to have a kink in it, similar to those observed in the past and connected with a change in direction of the ambient solar wind. Lying between and outside these streamers were fainter, more diffuse features.

IV.5.2 Reduction.

The measurement of the positions of discrete structures posed a difficult problem and three different approaches were tried. First of all a plate displaying many features in the plasma tail (JB10800) was digitised on the COSMOS measuring machine at the Royal Observatory Edinburgh. The resulting 512x512 pixel image had a resolution of 35 arcsec (0.5mm on plate).

Inspection of the image was performed using the image processing package ASPIC on the STARLINK Vax 11/750 computer at Leicester University. It quickly became apparent that the digitisation had made identification of small features in most cases impossible. Various image processing techniques were used, such as unsharp masking and differentiating the image to first order by using a linear shift. These only produced a slight improvement in the visibility of the features under study.

From then on it was decided to work with film copies of the plates. These lose little of the contrast and resolution of the original plates, whilst being in a very usable format. These were of a very high quality, some of which has subsequently been lost in the transition to the copies shown on plate IV.2. Indeed, some features on the original plates themselves only became apparent after careful inspection.

To measure positions of plasma features, an X-Y measuring table was tried but had to be abandoned, due to the loss of contrast involved when inspecting the plates through the microscopic viewer. It was concluded that the most accurate method available was measuring the positions by hand.

The CHART facility was used to produce an overlay of the plate field with the positions of the the nucleus clearly marked. The position of a feature on an image was determined by using a sheet of transparent graphpaper marked at intervals of 1mm, together with a handheld magnifying eyepiece

with a scale ruled every 0.1mm. The total error due to the superposition of the reference grid and the identification of the exact position of each ion structure was judged to be at most $\pm 0.5\text{mm}$. Table IV.5 gives a description of the 25 separate features measured on the plates. These are all plotted in figure IV.8. For all the features studied, the first point measured is that nearest the nucleus. As expected all the features are moving downstream from the coma.

Supposing a radial component of the solar wind of $W_{sw}(r) = 450 \text{ km s}^{-1}$ and a polar component of $W_{sw}(\theta) = -1 \text{ km s}^{-1}$, the tail would be out of the orbital plane of the comet by only $\sim 0.1^\circ$. Thus the tail can be assumed to lie in the orbital plane. The radial distance of a feature downstream from the nucleus was then derived through simple trigonometry. To calculate the velocities of the features an average speed was arrived at by averaging over three successive plates. If a feature is measured to be at r_i on plate i , then the velocity at the mean position r_{i+1} is given by:

$$V(r_{i+1}) = \frac{r_{i+2} - r_i}{\Delta t_{i+2} + \Delta t_{i+1}} \quad (\text{IV.26})$$

Here Δt_{i+1} is the time between mid-exposure of plate i and plate $i + 1$. The resulting velocities are plotted in figure IV.9, and are divided into two categories. Filled circles denote velocities measured within the three main streamers. Open circles indicate velocities derived from structures lying outside these features.

Ref.	Feature	Plates	x_0	y_0
(a)	cloud	37-46	-22.1	64.8
(b)	cloud	37-46	-24.1	62.9
(c)	cloud	37-44	-25.5	44.6
(d)	cloud	37-43	-29.4	50.9
(e)	cloud	37-42	-34.8	57.2
(f)	kink	40-46	-6.9	31.0
(g)	cloud	42-44	-7.2	19.8
(h)	kink	43-47	-3.3	16.8
(i)	kink	37-39	-10.3	22.3
(j)	cloud	38-43	-15.6	34.5
(k)	filament	37-40	-28.3	72.2
(l)	filament	37-40	-37.7	87.9
(m)	filament	37-44	-36.1	89.1
(o)	kink	39-43	-42.6	87.8
(p)	kink	32-47	-12.7	26.6
(q)	kink	44-46	-32.0	51.0
(r)	kink	41-46	-8.2	43.2
(s)	kink	37-39	-54.3	134.5
(t)	kink	41-45	-41.8	126.2
(u)	kink	44-46	-64.8	174.4
(v)	kink	43-45	-15.7	62.2
(w)	kink	41-43	-36.0	99.7
(x)	filament	43-47	-41.1	90.8
(y)	kink	37-40	-53.7	109.3
(z)	cloud	38-45	-30.7	60.0

Table IV.5: Discrete features observed on plates JB11037-JB11047. Position of a feature is in mm relative to the nucleus on the first plate it was observed.

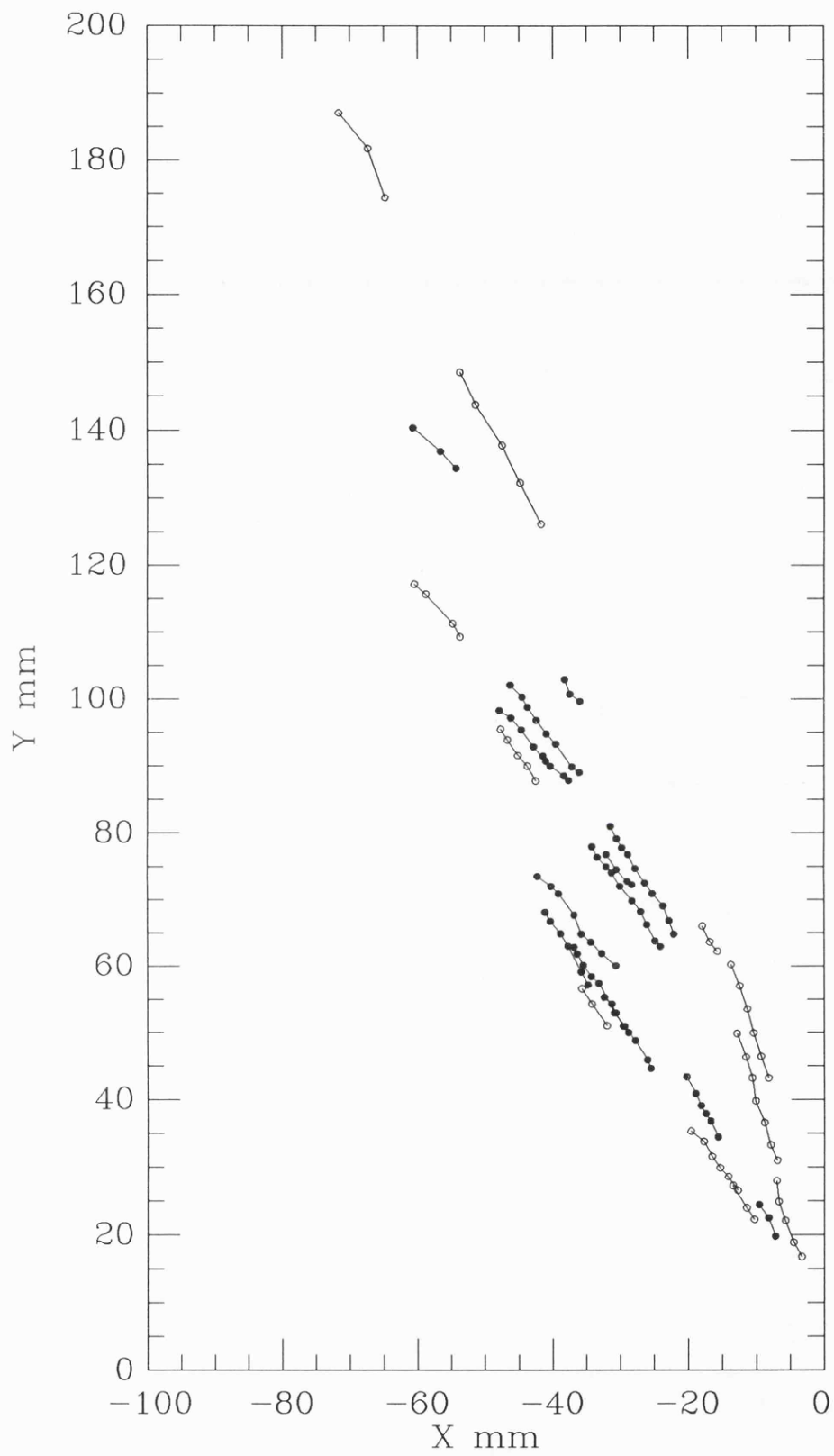


Figure IV.8: Positions of all features relative to the nucleus at (0,0). Lines connect measurements of the same feature. Open circles indicate positions outside the main streamers.

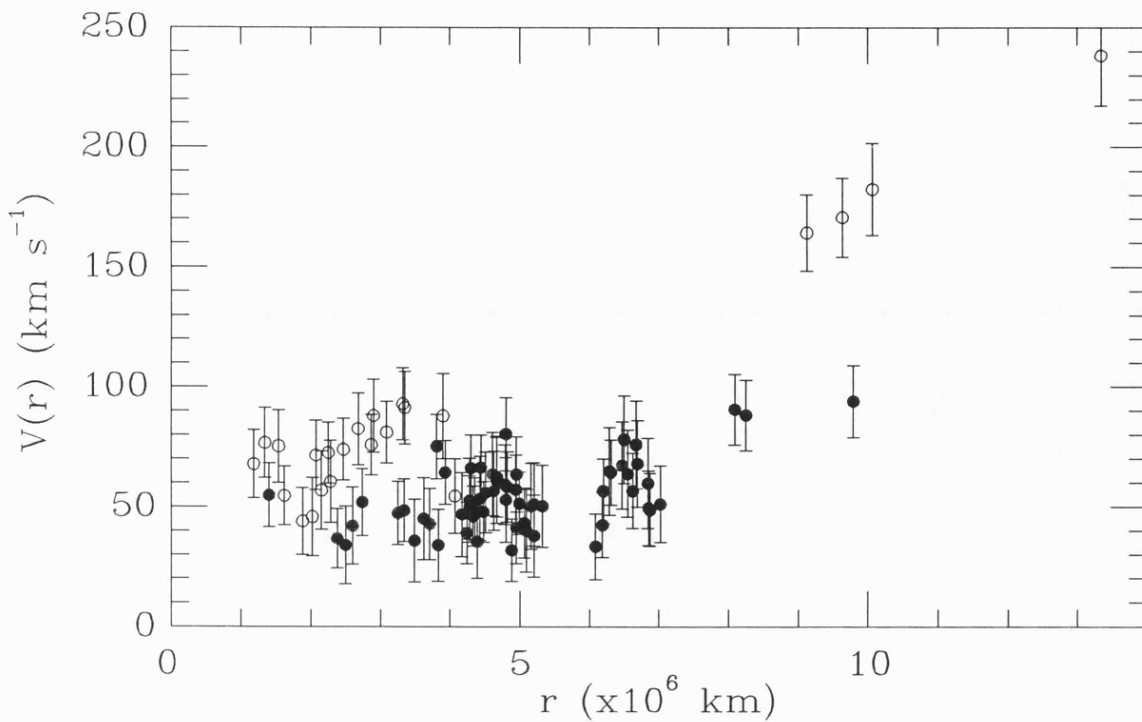


Figure IV.9: Radial velocities of features listed in Table IV.5 against distance r from the nucleus.

IV.5.3 The Observed Velocity Field.

From figure IV.9, the velocity in the inner tail appears to vary only slightly between 10^6 km and 6×10^6 km from the nucleus, the mean value appearing to lie at ~ 50 km s^{-1} . As the magnetic field is frozen into the plasma, this implies that the field line tension serving to 'pull' the line back into shape (i.e. downtail) is relatively ineffective. The mass of the ions accreted on the field lines may be large enough so that the resulting acceleration is small, mass loading may still be taking place or a combination of these two effects may be possible. Several other studies of velocity flows in Halley's plasma tail have been published. The results of those which investigate the distances under

Date of Observation	r (km)	V (km s ⁻¹)	ref
6/12/85	2.0 → 6.0 × 10 ⁶	50-80	Guerin & Koulchy (1986)
31/12/85	0.5 → 1.0 × 10 ⁶	55-60	Saito <i>et al.</i> (1987)
10/1/86	0.0 → 1.0 × 10 ⁶	20-80	Tonita (1987)
10/1/86	4.0 → 6.0 × 10 ⁶	50-100	Guerin & Koulchy (1986)
9/3/86	3.0 → 5.0 × 10 ⁶	~53	Neidner & Schwingenschuh (1987)
-	0.0 → 5.0 × 10 ⁶	20-30	Celnik & Th.Schmidt-Kaler (1987)
20/3/86	2.0 → 6.0 × 10 ⁶	38-40	Brosius <i>et al.</i> , (1987)
11/4/86	2.0 → 5.0 × 10 ⁶	60	Brosius <i>et al.</i> , (1987)

Table IV.6: Previous determinations of velocities in Halleys' ion tail.

consideration here are summarised in table IV.6. The result of this thesis is in excellent agreement with the previous studies. In particular Niedner and Schwingenschuh (1987) note that studies of plasma features typically give downtail velocities of $\sim 50 \text{ km s}^{-1}$.

From the studies listed in Table IV.6, it seems that the effect of the accelerations on the ions only appear at around $6 \times 10^6 < y < 10^7 \text{ km}$. The existence of only one determined velocity at this distance precludes confirmation of this effect. It should be noted though that the measured velocity of $94 \pm 15 \text{ km s}^{-1}$ at $r = 9.79 \times 10^6 \text{ km}$ does indeed lie above any of the other inner tail velocities measured.

Magnetohydrodynamic models such as those of Wegmann *et al.* (1987) predict that as one moves away from the tail axis, the bulk velocity of the

ions increases monotonically until the prevalent solar wind speed is reached. The rate at which the velocity is shown to increase varies from model to model. The ICE probe (Bame *et al.*, 1986) recorded a fairly linear change in velocity from 500 km s^{-1} to $\sim 20 \text{ km s}^{-1}$ over the range $10^5 \text{ km} > z > 0$ km. However this was a comet with an ion production rate a factor of 10 less than that of Halley, and the impact parameter was only $y = 7800 \text{ km}$. The flaring of the magnetotail behind the nucleus assures that for a large comet at $y > 10^6 \text{ km}$, the width of the slowed plasma flow would certainly be much greater than that measured by ICE.

The only previous study of the variation in velocity perpendicular to the tail axis was that performed by Jockers and Lüst (1972). They found that the velocities of the features lying on the outer edges of the tail were generally higher than those in the center. The same result is clearly demonstrated in figure IV.9. Features outside the main plasma tail are indicated by open circles. These tend to possess higher velocities than those within the inner tail (filled circles).

To quantify this observation, a study was made of the measured velocity as a function of z , the distance from the tail axis. Assuming the tail axis lies at an aberration angle of $\simeq 9^\circ$ is unsatisfactory, due to the pronounced bend in the tail near the coma. Instead the central streamer is identified as being the optical counter-part of the current sheet lying at $\epsilon = 13.2^\circ$.

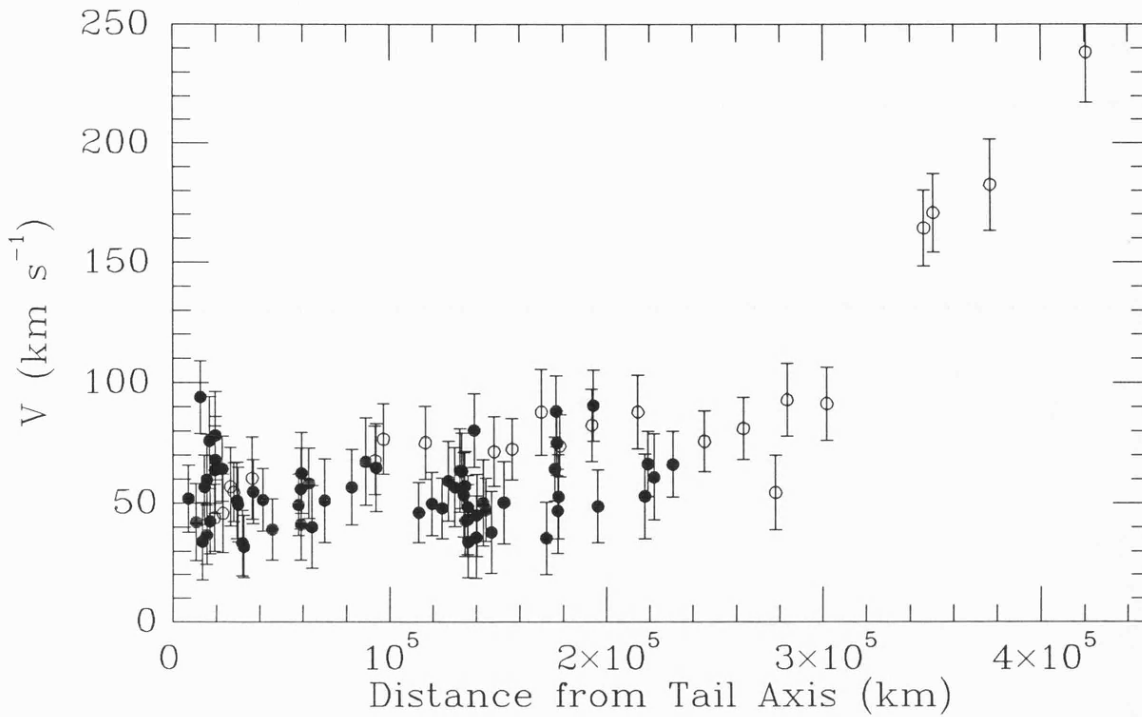


Figure IV.10: Radial velocities of features listed in table IV.5 as a function of distance from the tail axis.

The resulting velocity distribution is shown in figure IV.10. It is evident that features tend to have higher velocities at larger distances from the tail. Surprising is the fact that there seems to be little increase in velocity for $z < 2 \times 10^5$ km, implying a main tail width of at least 4×10^5 km. The model of Halley generated by Wegmann *et al.* (1987) does seem to predict a fairly constant velocity profile 3×10^5 km either side of the tail axis at a distance of $z = 10^6$ km, but direct comparison is difficult due to the method by which their results are displayed.

In interpreting this diagram, account must be taken of projection effects. These would place the position of features, and hence the respective velocities, nearer the tail than is actually the case. If this is non-negligible then

this would imply that steady plasma velocities of $50\text{-}70 \text{ km s}^{-1}$ hold over the whole width of the visible tail ($d \sim 4 \times 10^5 \text{ km}$). Whatever the case, the slow variation of $V(z)$ points to there being negligible curvature of the field lines threading the tail. Otherwise a noticeable acceleration would result. Such a conclusion is supported by the MHD model of Halley presented by Luhmann *et al.* (1988). Their diagram of severely draped field lines at $y < 1.2 \times 10^6$ suggests that there is both little magnetic tension or pressure in this region.

IV.5.4 The tail B-field.

The velocity observations allow an estimation of the field strength in the distant ion tail. This calculation was performed using the Cowley-Southward model of the distant geomagnetic tail (Cowley and Southward, 1980). Their description of field lines connected to the IMF at large distances should be readily applicable to the similar environment of a comet tail.

The basis of the model is the assumption of stress balance between the ions flowing into the current sheet and the field-line tension. If P_{\parallel} and P_{\perp} are the plasma pressures parallel and perpendicular to the field, then

$$P_{\parallel} - P_{\perp} = \frac{B^2}{\mu_0} \quad (\text{IV.27})$$

where B is the lobe field-strength. In the rest frame of the field lines, $P_{\perp} = 0$ and thus

$$2nm_i v^2 = \frac{B^2}{\mu_0}$$

$$\text{or } v = V_A = \frac{B}{\sqrt{2nm_i\mu_0}} \quad (\text{IV.28})$$

where n and m_i are the number density and mass of the ions. Thus the required bulk velocity of the ions for stress balance is just the Alfvén speed in the tail lobes.

The field lines themselves will be moving downtail in the rest-frame of the comet nucleus. The velocity of the ions flowing into the central tail is given by

$$V_f = V_m + V_A \quad (\text{IV.29})$$

where V_m is the initial velocity of the ions in the tailward direction. Once the ions have reached the current sheet, in the field-line frame they will emerge with a velocity V_A directed downtail. In the comets' nucleus frame of reference they will have picked up a large amount of kinetic energy through interaction with the current sheet. The observed outflow velocity in the comets' rest frame will then be

$$V_O = V_A + V_f = 2V_A + V_m \quad (\text{IV.30})$$

Equations (IV.27) and (IV.29) may be combined to give

$$B^2 = \frac{\mu_0 n m_i}{2} (V_O - V_m)^2 \quad (\text{IV.31})$$

The lobe field-strength then depends on the observed plasma velocity, together with the density and original velocity of the ions.

The initial velocity of the ions V_m is expected to be of the order of the outflow speeds of the neutral molecules ($\sim 1 \text{ km s}^{-1}$), which is negligible compared to the observed velocities of $\sim 50 \text{ km s}^{-1}$. This will be true as long as the ionisation process does not impart significant kinetic energy to the ion. The ionic density is estimated from the densities measured by *Giotto* in the coma given by Krankowsky *et al.* (1986) and Korith *et al.* (1987). From comparing these results at distances $r = 10^4 \text{ km}$ and $r = 10^5 \text{ km}$, $n(H_2O)/n(ions) \simeq 10^{-2}$ in this region, where $n(ions)$ is the number density of water group ions.

Taking this ratio to be true for the production rates, then as all ions will be accelerated downtail the average density in this region is

$$\rho \simeq \frac{Q_{ions}}{\pi r^2 V_O} m_i \quad (\text{IV.32})$$

where r is the radius of the tail considered, $r \simeq 10^5 \text{ km}$. Combining this with $Q_{H_2O} \simeq 10^{29} \text{ s}^{-1}$ (Schloerb, Claussen and Tacconi-Gaman, 1987) and equation (IV.30)

$$B^2 \sim \frac{\mu_0 Q_{ions} m_i}{2 \pi r^2} V_O \quad (\text{IV.33})$$

$$B \sim 5 \text{ nT} \quad (\text{IV.34})$$

Thus the B-field strength in the distant tail lobes is similar to that prevalent in the IMF. This result is in agreement with the calculations by Ershkovich

(1978), and more recently the detailed modelling by Wegmann *et al.* (1987).

IV.6 CONCLUSIONS AND FUTURE WORK.

The two fundamental results of this work have been as follows:

a) The aberration angle of the ion tail of comet P/Halley during its' 1985/86 apparition can be explained (and indeed could have been predicted) using a standard model of the solar wind velocity field. However on one, or possibly two occasions, the solar wind displayed large directional peculiarities. Such events have been noted in previous studies.

b) The spacecraft missions showed that the predictions of MHD models for the ionic velocity field in the coma were correct. It has been shown unambiguously here that the same is true for the distant magnetotail; the bulk velocity of the ions increases as one travels further from the tail axis. The actual measurements show that the velocity of the tail ions is steady within the confines of the current sheet boundaries. In turn the velocities observed point to a confining magnetic field with a similar strength to that found in the IMF.

The inclusion of the UK Schmidt plates in the IHW archive with those taken on other telescopes will, in the near future, allow the study presented here to be performed again but with a time span covering the whole apparition. This will hopefully make possible an investigation into whether the tail velocity field varies or remains constant over a range of heliocentric distances. What would be really desirable is the passage through the distant

plasma tail of a comet by a spacecraft such as the proposed (but shelved) Cometary Rendezvous and Asteroid Flyby mission. The problem with a flyby is the same as that faced by the ICE mission planners, that of predicting the solar wind velocity and the corresponding aberration angle (see Brandt *et al.*, 1988).

In light of the remoteness of such an encounter, theoretical studies will remain an important area of future work. All recent models qualitatively agree on the structure of the plasma tail for distances out to $y = 10^6$ km. A concerted effort is now needed on the distant tail. How do the physical parameters of the tail (density, velocity, field strength) vary as one proceeds to $y > 10^7$ km downstream for various values of $Q(\text{ions})$, W_{sw} and heliocentric distance? Noting that these structures can extend for up to $\sim 3 \times 10^8$ km from the nucleus, how can they remain stable against the numerous instabilities that can exist in plasmas? It is only right that such questions should be answered, as ion tails are what make comets some of the most beautiful objects in the heavens.

IV.7 REFERENCES

- Alfven, H., 1957, *Tellus*, **9**, 92.
- Bame, S.J., Anderson, R.C., Asbridge, J.R., Baker, D.N., Feldman, F.D., Fuselier, S.A., Gosling, J.T., McComas, D.J., Thomsen, M.F., Young, D.T. & Zwickl, R.D., 1986, *Science*, **232**, 356.
- Belton, M.J.S. & Brandt, J.C., 1966, *Astrophys. J. Suppl.*, **13**, 125.
- Biermann, L., 1951, *Z. Astrophys.*, **29**, 274.
- Brandt, J.C., Harrington, R.S. & Roosen, R.G., 1973, *Astrophys. J.*, **184**, 27.
- Brandt, J.C., Farquhar, R.W., Maran, S.P., Niedner Jr., M.B. & von Rosenhinge, T.T., 1988, in *Exploration of Halley's Comet*, ed. Grewing, M., Praderie, F. & Reinhard, R., Springer-Verlag, 969.
- Brosius, J.W., Holman, G.D., Niedner, M.B., Brandt, J.C., Slavin, J.A., Smith, E.J., Zwickl, R.D. & Bame, S.J., 1987, *Astron. Astrophys.*, **187**, 267.
- Celnik, W.E. & Schmidt-Kaler, Th., 1987, *Astron. Astrophys.*, **187**, 233.
- Chamberlain, J.W., 1961, *Astrophys. J.*, **133**, 675.
- Coates, A.J., Johnstone, A.D., Thomsen, M.F., Formisano, V., Amata, E., Wilken, B., Winningham, J.D., Borg, H. & Bryant, D.A., 1987, *Astron. Astrophys.*, **187**, 55.
- Cowley, S.W.H. & Southward, D.J., 1980, *Geophys. Res. Lett.*, **7**, 833.

- Eberhardt, P., Krankowsky, D., Schulte, W., Dolder, U., Lämmerzahl, P., Berthelier, J.J., Woveries, J., Stubbemann, U., Hodges, R.R., Hoffmann, J.H. & Illano, J.M., 1987, *Astron. Astrophys.*, **187**, 481.
- Ershkovich, A.I., 1978, *Mon. Not. R. astr. Soc.*, **184**, 755.
- Ershkovich, A.I., Niedner Jr., M.B. & Brandt, J.C., 1982, *Astrophys. J.*, **262**, 396.
- Finson, M.L. & Probst, R.F., 1968, *Astrophys. J.*, **154**, 327.
- Fulle, M. & Pansecchi, L., 1984, *Icarus*, **57**, 410.
- Guerin, P., Koulchy, S. & Vial, J.C., 1986, *Astron. Astrophys.*, **167**, 395.
- Hartle, R.E. & Sturrock, P.A., 1968, *Phys. Rev. Lett.*, **16**, 628.
- Ip, W.-H., 1980, *Astron. Astrophys.*, **81**, 260.
- Jockers, K., 1985, *Astron. Astrophys. Suppl. Ser.*, **62**, 791.
- Jockers, K. & Lüst, R., 1972, *Astron. Astrophys.*, **21**, 199.
- Kimmel, C.D., Luhmann, J.G. & Phillips, J.L., 1987, *J. Geophys. Res.*, **92**, 8536.
- Krankowsky, D., Lämmerzahl, P., Herrewerth, I., Woveries, J., Eberhardt, P., Dolder, U., Herrmann, U., Schulte, W., Berthelier, J.J., Illiano, J.M., Hodges, R.R. & Hoffmann, J.H., 1986, *Nature*, **321**, 326.
- Korth, A., Richter, A.K., Mendis, D.A., Anderson, K.A., Carlson, C.W., Curtis, D.W., Lin, R.P., Mitchell, D.L., Rème, H., Sauvaud, J.A. & d'Uston, C., 1987, *Astron. Astrophys.*, **187**, 149.

- Kozima, M. & Kakinuma, T., 1987, *J. Geophys. Res.*, **92**, 7269.
- Luhmann, J.G., Fedder, J.A. & Winske, D., 1988, *J. Geophys. Res.*, **93**, 7532.
- Magnani, L. & A'Hearn, M.F., 1986, *Astrophys. J.*, **302**, 477.
- McComas, D.J., Gosling, J.T., Bame, S.J., Slavin, J.A., Smith, E.J. & Steinberg, J.L., 1987, *J. Geophys. Res.*, **92**, 1139.
- Meyer, F. & Schmidt, H., 1967, *Z. Astrophys.*, **65**, 274.
- Niedner Jr., M.B., Ershkovich, A.I. & Brandt, J.C., 1983, *Astrophys. J.*, **272**, 362.
- Niedner Jr., M.B. & Schwengenschuh, K., 1987, *Astron. Astrophys.*, **187**, 103.
- Oyama, K.-i., Hirao, K., Hirano, T., Yumoto, K. & Saito, T., 1986, *Nature*, **321**, 310.
- Parker, E.N., 1958, *Astrophys. J.*, **128**, 664.
- Priest, E.R., 1984a, in *Solar Magnetohydrodynamics*, D. Reidel Publish. Co., p424.
- Priest, E.R., 1984b, in *Solar Magnetohydrodynamics*, D. Reidel Publish. Co., p101.
- Saito, T., Yumoto, K., Hirao, K., Minami, S., Saito, K. & Smith, E., 1987, *Astron. Astrophys.*, **187**, 209.
- Schloerb, F.P., Claussen, M.J. & Tacconi-Gaman, L., 1987, *Astron.*

Astrophys., **187**, 469.

Siscoe, G.L., Goldstein, B. & Lazarus, A.J., 1969, *J. Geophys. Res.*, **74**, 1759.

Slavin, J.A., Smith, E.J., Daly, P.W., Flammer, K.R., Gloeckler, G., Goldberg, B.A., McComas, D.J., Scarf, F.L. & Steinberg, J.L., 1986, *20th ESLAB Symp., ESA SP-250*, **I**, 81.

Smith, E.J., 1979, *Rev Geophys. Space Res.*, **17**, 624.

Tomita, K., Saito, T. & Minami, S., 1987, *Astron. Astrophys.*, **187**, 215.

von Rosenhinge, T.T., Brandt, J.C. & Farquhar, 1986, *Science*, **232**, 353.

Wallis, M.K. & Johnstone, A.D., 1982, in *Cometary Exploration, I, Proc. International Conf. Cometary Exploration*, ed. T.I. Gombosi, p307.

Weber, E.J. & Davis, L., 1967, *Astrophys. J.*, **148**, 217.

Weber, E.J. & Davis, L., 1970, *J. Geophys. Res.*, **75**, 2419.

Wegmann, R., Schmidt, H.U., Huebner, W.F. & Boice, D.C., 1987, *Astron. Astrophys.*, **187**, 339.

Appendix

The following pages contain a complete list of the cometary magnitudes observed from La Palma in December 1985 and May 1986, and South Africa in March 1986. All the tables are in a similar format. Each record consists of 2 lines. The first line lists in order:

- The date of observation
- The position of the measurement in arcsec relative to the nucleus. Positive x and y are to the East and North of the nucleus respectively.
- The diameter of the aperture in arcsec.

The second line then lists the above atmosphere magnitudes of the comet at that date, position and aperture size. In tables A1–A3 the position listed is the beam direction for the filters OH, BC, CN, C₃ and CO⁺ only. The magnitudes for the remaining four filters 177 arcsec North of that position *i.e.* at Y_{pos}+177. For example, a complete set of magnitudes centered on the nucleus would be obtained by taking the OH, BC, CN, C₃ and CO⁺ measurements at X_{pos}= 0, Y_{pos}= 0, followed by the CV, C₂, RC and H₂O⁺ measurements listed under X_{pos}= 0, Y_{pos}= -177. For the other tables (A4–A13) the position listed is correct for all magnitudes tabulated. A magnitude of -1.00 indicates a non-detection.

Table A1. Reduced magnitudes for the night of December 7th 1985.

Date	Xpos	Ypos	Aper.	OH	BC	CN	C ₃	CO ⁺	VC	C ₂	RC	H ₂ O ⁺
7.8580			62		0	0	62					
8.31	10.69	7.95	9.19	10.32	13.24	9.93	12.73	12.45				
7.8620			62		0	-177	62					
9.81	15.27	9.86	13.53	15.00	9.52	7.94	8.65	8.49				
7.8883	1500	0	62									
14.35	-1.00	15.04	18.03	-1.00	16.46	15.86	14.73	14.77				
7.8930	1500	-177	62									
14.34	-1.00	15.14	-1.00	-1.00	-1.00	16.53	-1.00	14.88				
7.8983	1200	0	62									
13.68	-1.00	14.23	17.58	-1.00	17.21	15.38	-1.00	-1.00				
7.9005	1200	-177	62									
13.56	-1.00	14.18	16.52	17.00	17.65	15.18	-1.00	-1.00				
7.9035	900	0	62									
12.69	-1.00	13.22	18.77	-1.00	16.89	14.30	-1.00	-1.00				
7.9056	900	-177	62									
12.90	-1.00	13.31	18.77	-1.00	17.64	14.22	-1.00	-1.00				
7.9088	600	0	62									
11.74	-1.00	12.03	17.02	16.99	16.28	12.93	15.91	-1.00				

Table A1 (continued).

Date	Xpos	Ypos	Aper.	OH	BC	CN	C ₃	CO ⁺	VC	C ₂	RC	H ₂ O ⁺
7.9108	600	-177	62									
11.83	-1.00	12.22	18.77	17.74	13.26	12.67	-1.00	-1.00				
7.9138	300	0	61									
10.57	16.33	10.62	11.78	16.55	15.26	11.36	-1.00	-1.00				
7.9158	300	-177	62									
11.04	17.32	11.33	15.75	16.23	16.13	11.28	-1.00	-1.00				
7.9189	1800	0	62									
15.22	-1.00	15.86	17.25	-1.00	16.00	16.51	-1.00	-1.00				
7.9210	1800	-177	62									
15.95	18.06	16.41	-1.00	17.73	16.27	16.51	-1.00	-1.00				
7.9241	-300	0	62									
10.58	14.56	10.15	13.88	14.19	13.55	10.85	13.02	12.49				
7.9261	-300	-177	62									
10.79	16.55	10.51	14.95	15.69	13.38	10.57	12.81	12.33				
7.9304	-600	0	62									
11.81	15.35	11.21	15.24	15.33	14.30	12.23	13.64	12.92				
7.9342	-600	-177	62									
11.97	17.29	11.34	16.99	16.72	15.02	12.22	14.71	-1.00				

Table A1 (continued).

Date	Xpos	Ypos	Aper.	OH	BC	CN	C ₃	CO ⁺	VC	C ₂	RC	H ₂ O ⁺
7.9345	-900	0	62									
12.95	17.28	11.97	16.23	16.35	15.07	13.39	17.09	13.97				
7.9376	-900	-177	62									
13.07	17.27	12.06	17.22	17.71	16.87	13.56	-1.00	15.79				
7.9406	-1200	0	62									
13.59	16.52	12.51	16.78	16.70	15.77	14.49	-1.00	16.54				
7.9427	-1200	-177	62									
13.56	-1.00	12.66	17.97	17.70	16.25	14.44	14.01	15.55				
7.9457	-1500	0	62									
14.06	16.81	12.98	16.77	18.44	18.36	15.59	-1.00	16.85				
7.9478	-1500	-177	62									
14.27	16.49	13.11	17.52	-1.00	16.85	15.99	-1.00	-1.00				
7.9508	-1800	0	62									
15.77	17.24	13.39	17.95	16.92	17.16	17.08	16.33	15.44				
7.9528	-1800	-177	62									
14.98	16.23	13.41	17.94	18.43	18.35	17.08	-1.00	-1.00				
7.9551	-2100	0	62									
-1.00	17.98	13.74	18.69	18.42	18.35	16.20	-1.00	14.00				

Table A1 (continued).

Date	Xpos	Ypos	Aper.	OH	BC	CN	C ₃	CO ⁺	VC	C ₂	RC	H ₂ O ⁺
7.9573	-2100	-177	62									
15.69	16.46	13.87	16.74	16.91	-1.00	18.58	-1.00	-1.00				
7.9697	0	0	62									
8.44	10.65	7.95	9.16	10.27	13.42	9.97	13.05	12.38				
7.9723	0	-181	62									
10.09	14.82	9.91	13.58	14.83	9.48	7.91	8.59	8.41				
7.9771	0	-362	62									
10.93	16.68	10.93	15.92	16.08	13.81	10.14	13.74	12.79				
7.9792	0	-545	62									
11.73	-1.00	11.70	17.11	16.83	14.99	11.40	14.54	14.08				
7.9820	0	-726	62									
12.35	16.65	12.53	16.49	18.32	16.18	12.54	15.29	15.39				
7.9842	0	-906	62									
13.19	16.63	13.09	16.65	17.12	16.78	13.50	17.04	-1.00				
7.9871	0	-1087	62									
13.16	17.81	13.67	17.07	-1.00	16.78	14.18	14.53	14.84				
7.9891	0	-1267	62									
13.70	17.79	14.19	16.82	16.79	-1.00	15.15	-1.00	-1.00				

Table A1 (continued).

Date	Xpos	Ypos	Aper.						
OH	BC	CN	C ₃	CO ⁺	VC	C ₂	RC	H ₂ O ⁺	
7.9924	0	-1449	62						
13.98	-1.00	14.51	16.61	17.08	-1.00	15.99	15.52	-1.00	
7.9944	0	-1629	62						
13.59	-1.00	14.86	16.04	16.76	17.06	18.49	-1.00	-1.00	
7.9975	0	-1810	62						
14.30	17.73	15.83	17.02	16.49	17.50	17.28	-1.00	13.13	
8.0005	0	-2168	62						
14.21	-1.00	16.13	17.76	-1.00	-1.00	16.96	-1.00	-1.00	

Table A2. Reduced magnitudes for the night of December 8th 1985.

Date	Xpos	Ypos	Aper.	OH	BC	CN	C ₃	CO ⁺	VC	C ₂	RC	H ₂ O ⁺
8.8648	0	0	62									
8.25	10.63	7.84	9.11	10.23	13.29	9.90	12.73	12.37				
8.8668	0	-177	62									
9.84	14.85	9.81	13.35	14.93	9.51	7.84	8.64	8.43				
8.8706	0	177	62									
9.94	14.37	9.72	13.35	14.30	15.36	11.36	14.39	14.81				
8.8726	0	354	62									
10.90	16.26	10.70	16.61	16.33	16.11	12.37	14.68	14.97				
8.8754	0	531	62									
11.63	16.69	11.34	17.36	16.64	17.30	13.22	14.24	14.81				
8.8775	0	708	62									
12.29	16.45	11.90	17.67	17.83	16.75	13.93	17.18	14.19				
8.8807	0	885	62									
12.88	-1.00	12.42	17.67	17.83	-1.00	14.60	15.06	14.76				
8.8830	0	1062	62									
13.38	17.00	12.92	-1.00	17.83	16.99	15.68	15.23	14.97				
8.8862	0	1239	62									
14.22	-1.00	13.45	-1.00	18.58	17.30	15.90	15.43	14.66				

Table A2 (continued).

Date	Xpos	Ypos	Aper.	OH	BC	CN	C ₃	CO ⁺	VC	C ₂	RC	H ₂ O ⁺
8.8882	0	1416	62									
14.65	-1.00	13.88	-1.00	-1.00	-1.00	-1.00	16.30	13.72	14.53			
8.8904	0	1593	62									
15.40	-1.00	14.41	17.67	-1.00	17.74	16.94	-1.00	16.92				
8.8924	0	1770	62									
16.14	-1.00	14.51	-1.00	-1.00	-1.00	16.94	-1.00	17.36				
8.8946	0	1947	62									
15.39	-1.00	14.84	-1.00	-1.00	17.74	-1.00	15.98	14.45				
8.8966	0	2124	62									
16.12	-1.00	15.10	-1.00	-1.00	-1.00	18.68	14.67	14.35				
8.9092	0	-354	62									
10.86	16.97	10.94	15.59	16.45	13.65	10.00	13.72	12.88				
8.9112	0	-531	62									
11.62	18.15	11.81	17.09	16.81	15.62	11.55	-1.00	15.99				
8.9194	0	0	41									
8.99	11.07	8.48	9.59	10.64	13.69	10.73	12.94	13.00				
8.9214	0	-177	41									
10.78	16.02	10.70	14.22	15.95	9.95	8.47	9.06	8.87				

Table A2 (continued).

Date	Xpos	Ypos	Aper.						
OH	BC	CN	C ₃	CO ⁺	VC	C ₂	RC	H ₂ O ⁺	
8.9253	0	-59	41						
9.83	13.28	9.52	11.58	12.98	13.09	10.11	12.46	12.22	
8.9275	0	-118	41						
10.28	14.54	10.15	12.95	14.37	11.97	9.41	11.28	10.92	
8.9305	0	-236	41						
11.18	16.00	11.13	15.24	16.04	12.21	9.52	11.55	11.19	
8.9325	0	-295	41						
11.53	18.11	11.53	16.21	16.79	13.52	10.24	12.96	12.53	
8.9354	0	-354	41						
11.78	17.35	11.85	16.42	17.03	14.64	10.92	14.38	13.47	
8.9375	0	-413	41						
12.09	-1.00	12.13	17.61	16.79	15.11	11.52	15.22	14.06	
8.9397	0	-472	41						
12.23	17.34	12.39	17.29	17.02	15.52	12.00	14.90	14.48	
8.9416	0	-531	41						
12.20	12.72	12.00	12.51	12.64	16.07	12.47	15.97	14.90	
8.9439	0	-590	41						
12.80	18.08	12.97	18.04	16.78	16.35	12.87	15.41	14.90	

Table A2 (continued).

Date	Xpos	Ypos	Aper.					
OH	BC	CN	C ₃	CO ⁺	VC	C ₂	RC	H ₂ O ⁺
8.9458	0	-649	41					
12.99	-1.00	13.18	-1.00	17.77	16.51	13.24	-1.00	14.64
8.9565	0	59	41					
9.85	12.86	9.29	11.31	12.56	14.83	11.30	13.80	13.77
8.9585	0	59	41					
9.86	12.90	9.31	11.32	12.56	14.75	11.32	14.90	13.82
8.9615	0	118	41					
10.44	14.26	9.98	12.87	13.94	15.50	11.82	16.40	14.78
8.9635	0	177	41					
10.96	15.14	10.54	14.02	14.91	16.32	12.25	16.40	14.88
8.9656	0	236	41					
11.32	16.06	10.95	15.12	15.62	16.69	12.64	15.04	15.00
8.9698	0	354	41					
12.01	-1.00	11.55	16.47	16.22	16.92	13.30	15.64	15.21
8.9718	0	295	41					
11.69	16.47	11.30	15.72	16.21	17.67	12.94	15.20	15.58
8.9740	0	413	41					
12.19	17.96	11.78	16.46	15.86	17.67	13.51	15.40	15.47

Table A2 (continued).

Date	Xpos	Ypos	Aper.						
OH	BC	CN	C ₃	CO ⁺	VC	C ₂	RC	H ₂ O ⁺	
8.9760	0	472	41						
12.44	17.20	12.01	16.97	16.35	16.91	13.78	16.39	15.81	
8.9872	0	0	41						
9.17	11.09	8.45	9.56	10.68	14.24	10.62	14.63	13.43	
8.9906	-62	0	41						
9.93	12.90	9.53	11.43	12.56	14.01	10.79	13.99	13.00	
8.9939	-124	0	41						
10.49	13.91	10.08	12.58	13.46	14.01	10.95	14.12	13.04	
8.9969	-186	0	41						
11.07	14.50	10.52	13.47	17.64	14.21	11.29	14.26	13.20	
8.9998	-248	0	41						
11.31	15.28	10.90	14.33	14.75	14.26	11.51	13.81	13.09	
9.0028	-310	0	41						
11.89	15.37	11.14	14.83	15.17	14.35	11.81	17.12	13.34	
9.0057	-372	0	41						
12.01	15.97	11.32	15.31	15.55	14.65	12.09	15.00	13.52	
9.0094	-434	0	41						
12.59	16.18	11.53	15.95	16.08	14.57	12.36	15.91	13.70	

Table A2 (continued).

Date	Xpos	Ypos	Aper.						
OH	BC	CN	C ₃	CO ⁺	VC	C ₂	RC	H ₂ O ⁺	
9.0117	0	-496	41						
12.76	16.91	11.71	17.02	15.92	14.92	12.22	-1.00	14.10	
9.0147	0	-558	41						
12.35	16.86	11.86	16.57	16.80	15.00	12.60	-1.00	14.16	
9.0180	0	-620	41						
13.07	-1.00	12.03	17.72	17.07	15.23	13.09	-1.00	14.93	
9.0210	0	-682	41						
13.23	-1.00	12.21	-1.00	17.51	15.41	12.92	-1.00	16.06	

Table A3. Reduced magnitudes for the night of December 9th 1985.

Date	Xpos	Ypos	Aper.		
OH	BC	CN	C ₃	CO ⁺	VC
9.8405	-59	0	41		
9.35	13.21	9.13	11.16	12.91	14.39
9.8416	-118	0	41		
10.05	15.09	9.97	12.92	14.68	14.67
9.8429	-177	0	41		
10.68	15.97	10.62	14.34	15.61	15.25
9.8443	-236	0	41		
11.06	16.48	11.17	15.24	17.12	15.80
9.8455	-295	0	41		
11.48	16.72	11.63	16.40	18.62	15.80
9.8467	-354	0	41		
11.76	16.72	12.01	16.79	-1.00	15.63
9.8479	-413	0	41		
11.91	-1.00	12.32	16.79	-1.00	17.75
9.8491	-472	0	41		
12.22	-1.00	12.59	17.15	-1.00	16.55
9.8503	-531	0	41		
12.49	-1.00	12.84	17.15	-1.00	-1.00

Table A3 (continued).

Date	Xpos	Ypos	Aper.		
OH	BC	CN	C ₃	CO ⁺	VC
9.8514	-590	0	41		
12.64	-1.00	13.04	17.39	-1.00	16.11
9.8526	-649	0	41		
12.77	-1.00	13.22	18.14	-1.00	-1.00
9.8537	-708	0	41		
13.02	-1.00	13.51	16.95	-1.00	17.30
9.8671	0	0	28		
9.35	11.27	8.87	9.86	10.91	15.04
9.8684	0	-177	28		
11.54	18.21	11.47	15.09	16.01	10.11
9.8713	-59	-177	41		
10.65	15.95	10.57	14.14	15.42	11.67
9.8724	-118	-177	41		
10.85	15.71	10.77	14.73	15.75	12.81
9.8738	-177	-177	41		
11.10	16.26	11.01	15.06	16.23	13.49
9.8750	-236	-177	41		
11.38	17.45	11.27	15.16	16.11	13.98

Table A3 (continued).

Date	Xpos	Ypos	Aper.		
OH	BC	CN	C ₃	CO ⁺	VC
9.8763	-295	-177	41		
11.74	15.95	11.50	15.69	16.67	14.49
9.8774	-354	-177	41		
12.03	17.01	11.63	16.39	17.42	14.84
9.8786	-413	-177	41		
12.30	16.46	11.85	16.28	16.86	15.35
9.8797	-472	-177	41		
12.49	-1.00	12.05	16.63	17.10	15.71
9.8810	-531	-177	41		
12.61	18.20	12.10	18.13	16.66	15.55
9.8821	-590	-177	41		
12.79	17.45	12.27	16.94	17.10	15.55
9.8835	-649	-177	41		
12.94	-1.00	12.37	17.38	17.41	15.99
9.8846	-708	-177	41		
13.19	17.00	12.57	-1.00	17.10	16.54
9.8875	0	0	41		
8.64	10.83	8.18	9.32	10.43	14.06

Table A3 (continued).

Date	Xpos	Ypos	Aper.		
OH	BC	CN	C ₃	CO ⁺	VC
9.8887	0	-177	41		
10.65	16.69	10.56	14.26	15.90	9.67
9.8906	0	0	62		
7.95	10.39	7.46	8.79	10.00	13.18
9.8918	0	-177	62		
9.78	14.88	9.68	13.38	14.54	9.27
9.9300	0	0	14		
10.74	12.14	10.25	10.92	11.60	16.35
9.9312	0	-177	14		
12.92	18.10	12.87	16.22	17.80	10.91
9.9330	0	0	84		
7.52	10.10	7.00	8.44	9.72	12.51
9.9341	0	-177	84		
9.23	14.36	9.01	12.62	13.98	8.95
9.9358	0	0	112		
7.05	9.80	6.53	8.13	9.44	11.79
9.9371	0	-177	112		
8.55	13.60	8.36	11.94	13.31	8.69

Table A3 (continued).

Date	Xpos	Ypos	Aper.		
OH	BC	CN	C ₃	CO ⁺	VC
9.9594	0	-177	41		
10.93	16.25	10.52	14.25	15.47	9.67
9.9606	59	-177	41		
10.98	16.24	10.71	14.64	15.79	12.04
9.9619	118	-177	41		
11.17	16.79	11.03	15.16	16.36	13.57
9.9631	177	-177	41		
11.46	-1.00	11.37	15.80	16.36	14.56
9.9643	236	-177	41		
11.66	-1.00	11.72	16.23	16.72	15.47
9.9655	295	-177	41		
12.00	16.77	12.02	16.47	16.96	15.71
9.9667	354	-177	41		
12.09	-1.00	12.26	-1.00	17.27	16.66
9.9682	413	-177	41		
12.54	-1.00	12.55	17.97	16.35	17.21
9.9695	472	-177	41		
12.62	-1.00	12.74	-1.00	-1.00	16.15

Table A3 (continued).

Date	Xpos	Ypos	Aper.		
OH	BC	CN	C ₃	CO ⁺	VC
9.9706	531	-177	41		
12.87	-1.00	13.08	-1.00	-1.00	16.46
9.9718	590	-177	41		
13.41	17.92	13.21	17.95	-1.00	17.21
9.9731	649	-177	41		
13.37	-1.00	13.39	-1.00	-1.00	16.01
9.9776	177	-118	41		
11.23	15.39	10.75	14.41	15.23	13.21
9.9797	177	-59	41		
11.04	14.62	10.52	13.83	14.73	13.57
9.9802	177	0	41		
11.01	14.29	10.46	13.41	13.95	14.07
9.9813	177	59	41		
11.04	14.03	10.50	13.31	13.47	14.55
9.9826	177	118	41		
11.30	14.28	10.69	13.77	14.05	15.51
9.9837	177	177	41		
11.38	15.06	10.86	14.32	14.51	15.51

Table A3 (continued).

Date	Xpos	Ypos	Aper.		
OH	BC	CN	C ₃	CO ⁺	VC
9.9850	177	236	41		
11.80	15.14	11.08	15.24	15.25	16.43
9.9862	177	295	41		
11.99	15.88	11.36	15.63	15.89	16.86
9.9882	177	-236	41		
11.67	17.06	11.28	17.12	18.37	13.90
9.9893	177	-295	41		
12.11	17.04	11.59	-1.00	18.37	14.30
9.9906	177	-354	41		
12.10	16.59	11.82	-1.00	-1.00	14.66
9.9917	177	-413	41		
12.65	-1.00	12.15	-1.00	-1.00	15.27
9.9952	0	177	41		
11.04	15.36	10.39	14.16	15.33	15.64
9.9964	-59	177	41		
11.24	14.71	10.46	14.01	15.39	15.95
9.9977	-118	177	41		
11.27	14.71	10.64	14.24	15.31	16.59

Table A3 (continued).

Date	Xpos	Ypos	Aper.		
OH	BC	CN	C ₃	CO ⁺	VC
9.9988	-177	177	41		
11.76	14.91	10.85	14.43	14.59	15.72
10.0001	-236	177	41		
11.61	15.30	11.05	14.79	14.85	15.63
10.0012	-295	177	41		
11.93	15.17	11.30	15.24	15.16	15.53
10.0025	-354	177	41		
12.36	15.06	11.44	15.18	14.71	15.31
10.0038	-413	177	41		
12.46	14.79	11.57	15.59	14.80	15.37

Table A4. Reduced magnitudes for the night of March 13th 1986.

Date	Xpos	Ypos	Aper.	BC	CN	C ₃	CO ⁺	VC	C ₂	RC	H ₂ O ⁺
13.1161			30	8.41	6.06	7.42	8.07	7.26	5.82	6.40	6.28
13.1229			30	8.40	6.04	7.42	8.07	7.25	5.83	6.40	6.28
13.1336			10	9.78	8.12	9.10	9.36	8.55	7.63	7.61	7.52
13.1381			60	7.68	4.92	6.71	7.33	6.46	4.83	5.74	5.59
13.1506			90	7.26	4.36	6.36	6.89	6.10	4.33	5.34	5.18

Table A5. Reduced magnitudes for the night of March 14th 1986.

Date	Xpos	Ypos	Aper.	BC	CN	C ₃	CO ⁺	VC	C ₂	RC	H ₂ O ⁺
14.0978			90		0	0					
	7.34	4.50			6.48	6.96	6.18	4.47	5.40	5.24	
14.1078			60		0	0					
	7.81	5.09			6.83	7.43	6.63	4.97	5.84	5.69	
14.1119			45		0	0					
	8.12	5.53			7.12	7.78	6.99	5.38	6.18	6.03	
14.1212			30		0	0					
	8.62	6.18			7.58	8.29	7.50	6.00	6.69	6.54	
14.1255			20		0	0					
	9.13	6.90			8.09	8.75	7.99	6.65	7.17	7.00	
14.1078			90		0	0					
	7.35	4.49			6.47	6.97	6.17	4.44	5.39	5.23	

Table A6. Reduced magnitudes for the night of March 15th 1986.

Date	Xpos	Ypos	Aper.	BC	CN	C ₃	CO ⁺	VC	C ₂	RC	H ₂ O ⁺
15.0824			90	7.01	4.21	6.05	6.61	5.79	4.11	4.99	4.85
15.0922			60	7.37	4.81	6.38	6.96	6.14	4.63	5.29	5.18
15.1016			45	7.61	5.27	6.65	7.20	6.38	5.03	5.50	5.40
15.1109			30	7.96	5.95	7.05	7.56	6.74	5.60	5.82	5.73
15.1219			20	8.38	6.62	7.51	7.94	7.13	6.21	6.26	6.16
15.1285			90	7.02	4.21	6.06	6.61	5.79	4.10	4.99	4.84
15.1337			45	7.61	5.28	6.67	7.22	6.39	5.02	5.51	5.41

Table A7. Reduced magnitudes for the night of March 17th 1986.

Date	Xpos	Ypos	Aper.	BC	CN	C ₃	CO ⁺	VC	C ₂	RC	H ₂ O ⁺
17.0859			90	7.42	4.70	6.38	7.05	6.20	4.58	5.39	5.28
17.0956			60	7.80	5.22	6.71	7.45	6.61	5.06	5.79	5.69
17.1053			45	8.07	5.65	6.97	7.72	6.90	5.43	6.01	5.95
17.1150			30	8.45	6.27	7.39	8.09	7.28	5.98	6.41	6.31
17.1244			20	8.85	6.94	7.84	8.45	7.66	6.57	6.74	6.69
17.1350			90	7.39	4.65	6.34	7.01	6.17	4.51	5.37	5.24

Table A8. Reduced magnitudes for the night of March 18th 1986.

Date	Xpos	Ypos	Aper.	BC	CN	C ₃	CO ⁺	VC	C ₂	RC	H ₂ O ⁺
18.0684			90		0	0					
	7.11	4.35	6.16	6.73	5.89	4.22	5.07	4.96			
18.0779			30		0	0					
	8.43	6.28	7.46	8.06	7.24	5.97	6.36	6.27			
18.0877			20		0	0					
	8.97	7.04	8.04	8.61	7.78	6.67	6.90	6.83			
18.0975			60		0	0					
	7.57	5.06	6.60	7.18	6.35	4.55	5.50	5.38			
18.1073			45		0	0					
	8.05	5.77	7.07	7.61	6.78	4.42	5.94	5.88			
18.1166			90		0	0					
	7.12	4.38	6.19	6.74	5.92	4.25	5.10	4.96			
18.1278		45	0	30							
	10.42	7.12	9.81	9.98	9.20	7.23	8.62	8.26			
18.1368			30		0	-45					
	10.27	7.21	9.70	9.94	9.19	7.35	8.41	8.24			

Table A9. Reduced magnitudes for the night of May 6th 1986.

Date	Xpos	Ypos	Aper.					
BC	CN	C ₃	CO ⁺	VC	C ₂	RC	H ₂ O ⁺	
6.9046	0	0	41					
11.38	9.59	10.35	10.85	10.07	9.21	9.01	8.93	
6.9055	0	0	41					
11.34	9.58	10.35	10.85	10.05	9.22	9.04	8.92	
6.9149	0	0	41					
11.34	9.59	10.33	10.85	10.05	9.22	9.03	8.92	
6.9157	0	0	41					
11.34	9.56	10.35	10.85	10.06	9.22	9.01	8.94	
6.9202	300	0	41					
15.13	11.76	15.03	15.23	15.04	12.11	12.52	13.46	
6.9214	600	0	41					
-1.00	13.52	17.63	15.83	15.79	14.25	14.19	-1.00	
6.9230	900	0	41					
-1.00	14.71	-1.00	16.14	-1.00	-1.00	13.44	-1.00	
6.9242	1200	0	41					
-1.00	14.71	17.63	16.58	-1.00	16.85	13.64	-1.00	
6.9266	0	0	41					
11.31	9.58	10.35	10.87	10.05	9.21	9.02	8.92	

Table A9 (continued).

Date	Xpos	Ypos	Aper.					
BC	CN	C ₃	CO ⁺	VC	C ₂	RC	H ₂ O ⁺	
6.9278	0	0	41					
11.32	9.56	10.36	10.86	10.04	9.24	8.97	8.94	
6.9481	0	0	41					
11.31	9.57	10.36	10.88	10.06	9.22	9.03	8.92	
6.9497	1500	0	41					
-1.00	16.41	16.40	-1.00	16.52	-1.00	-1.00	-1.00	
6.9561	-300	0	41					
13.94	11.40	13.72	13.60	13.32	11.69	12.59	11.98	
6.9572	-600	0	41					
14.41	12.53	14.50	14.10	14.40	13.10	13.87	12.69	
6.9587	-900	0	41					
15.29	13.19	14.87	14.79	14.40	14.04	14.62	13.24	
6.9598	-1200	0	41					
15.29	13.52	15.07	15.18	14.57	14.22	15.37	14.05	
6.9613	-1500	0	41					
16.03	13.78	15.31	15.34	15.32	14.22	13.87	13.53	
6.9629	-1800	0	41					
16.78	14.64	15.45	15.78	-1.00	15.07	-1.00	13.81	

Table A9 (continued).

Date	Xpos	Ypos	Aper.					
BC	CN	C ₃	CO ⁺	VC	C ₂	RC	H ₂ O ⁺	
6.9710	-1800	0	41					
16.00	14.10	15.79	15.52	15.30	15.62	-1.00	15.11	
6.9726	-2100	0	41					
16.74	14.24	16.34	16.52	15.74	15.30	-1.00	13.61	
6.9740	-2400	0	41					
16.74	14.84	16.34	16.51	14.74	-1.00	-1.00	14.56	
6.9754	-2400	-300	41					
16.74	15.15	14.93	15.52	16.49	15.06	13.86	13.52	
6.9777	-2400	-600	41					
15.54	14.59	14.92	15.00	14.74	15.05	13.41	13.80	
6.9788	-2400	-900	41					
15.22	14.83	15.26	15.14	14.73	14.68	14.61	14.36	
6.9815	-1200	-300	41					
14.76	13.72	14.57	14.86	14.73	14.19	12.85	13.05	
6.9826	-1200	-600	41					
15.94	13.93	15.56	16.05	-1.00	14.40	14.60	14.19	
6.9844	-900	-300	41					
14.57	13.29	14.63	14.29	13.97	13.78	12.97	12.76	

Table A9 (continued).

Date	Xpos	Ypos	Aper.					
BC	CN	C ₃	CO ⁺	VC	C ₂	RC	H ₂ O ⁺	
6.9859	-600	-900	41					
14.73	12.68	14.79	14.53	14.52	13.33	13.09	13.04	
6.9876	-300	-300	41					
15.16	12.11	14.78	14.62	13.96	12.60	12.48	12.89	
6.9898	0	0	41					
11.36	9.61	10.36	10.86	10.08	9.24	9.01	8.96	
7.0052	0	0	41					
11.36	9.59	10.36	10.85	10.06	9.24	9.05	8.94	
7.0064	0	-300	41					
15.33	11.51	14.52	14.65	14.02	11.77	13.21	12.92	
7.0078	0	-600	41					
15.32	12.77	15.63	16.39	15.21	13.65	13.82	14.53	
7.0089	0	-900	41					
-1.00	13.90	17.37	17.14	-1.00	14.78	13.81	15.08	
7.0104	0	-1200	41					
15.74	14.20	-1.00	-1.00	-1.00	15.53	15.32	-1.00	
7.0115	0	-1500	41					
-1.00	14.94	-1.00	16.37	16.38	15.52	15.31	16.27	

Table A9 (continued).

Date	Xpos	Ypos	Aper.					
BC	CN	C ₃	CO ⁺	VC	C ₂	RC	H ₂ O ⁺	
7.0135	0	300	41					
14.96	11.70	14.84	15.17	14.27	12.05	13.37	13.26	
7.0144	0	-600	41					
-1.00	12.87	15.59	16.36	16.37	13.84	15.31	15.07	
7.0158	0	-900	41					
16.45	13.86	-1.00	-1.00	-1.00	14.96	13.80	15.07	
7.0167	0	1200	41					
16.43	14.36	-1.00	-1.00	-1.00	15.20	15.31	15.51	
7.0183	0	1500	41					
-1.00	15.34	17.31	17.09	15.17	15.51	14.11	15.51	
7.0201	0	0	41					
11.38	9.59	10.37	10.84	10.09	9.26	9.05	8.93	

Table A10. Reduced magnitudes for the night of May 7th 1986.

Date	Xpos	Ypos	Aper.				
BC	CN	C ₃	CO ⁺	VC	C ₂	RC	H ₂ O ⁺
7.9535	0	0	138				
10.00	7.50	8.82	9.51	8.78	7.47	7.84	7.69
7.9543	0	0	138				
10.02	7.50	8.81	9.51	8.78	7.47	7.85	7.69
7.9557	0	0	138				
10.01	7.50	8.81	9.52	8.77	7.47	7.84	7.70
7.9565	0	0	138				
10.02	7.50	8.81	9.51	8.78	7.47	7.84	7.70
7.9611	0	0	110				
10.26	7.80	9.03	9.76	9.00	7.77	8.07	7.93
7.9612	0	0	110				
10.27	7.80	9.02	9.76	9.03	7.77	8.08	7.91
7.9639	0	0	110				
10.25	7.79	9.03	9.76	9.01	7.76	8.08	7.91
7.9648	0	0	110				
10.23	7.80	9.04	9.75	8.99	7.77	8.05	7.92
7.9672	0	0	84				
10.63	8.24	9.35	10.09	9.32	8.20	8.38	8.25

Table A10 (continued).

Date	Xpos	Ypos	Aper.				
BC	CN	C ₃	CO ⁺	VC	C ₂	RC	H ₂ O ⁺
7.9680	0	0	84				
10.57	8.24	9.35	10.10	9.34	8.18	8.36	8.24
7.9694	0	0	84				
10.59	8.25	9.35	10.08	9.31	8.20	8.39	8.24
7.9702	0	0	84				
10.59	8.24	9.36	10.08	9.32	8.19	8.35	8.24
8.0199	0	0	41				
11.26	9.26	10.10	10.83	9.96	9.06	9.01	8.95
8.0207	0	0	41				
11.22	9.24	10.11	10.77	9.98	9.09	9.04	8.94
8.0221	0	0	21				
12.15	10.45	11.09	11.68	10.95	10.25	9.97	9.90
8.0250	0	0	21				
12.21	10.51	11.08	11.73	10.89	10.14	10.01	9.83
8.0244	0	0	62				
10.63	8.48	9.51	10.27	9.46	8.35	8.53	8.40
8.0252	0	0	62				
10.62	8.44	9.52	10.28	9.41	8.35	8.53	8.40

Table A11. Reduced magnitudes for the night of May 9th 1986.

Date	Xpos	Ypos	Aper.					
BC	CN	C ₃	CO ⁺	VC	C ₂	RC	H ₂ O ⁺	
9.8992	0	0	41					
11.31	9.17	10.02	10.75	10.01	9.05	9.04	8.97	
9.9000	0	0	41					
11.28	9.17	10.00	10.80	10.03	9.03	9.04	8.92	
9.9026	-60	0	41					
13.17	10.26	11.91	12.61	11.94	10.23	10.93	10.86	
9.9038	-120	0	41					
14.03	10.90	13.03	13.18	12.69	10.95	11.65	11.63	
9.9052	-180	0	41					
14.29	11.42	13.60	13.61	13.07	11.48	12.24	11.83	
9.9064	-240	0	41					
14.29	11.87	13.96	13.84	13.38	11.90	12.37	12.27	
9.9077	-300	0	41					
14.63	12.06	14.12	14.14	13.51	12.28	12.68	12.33	
9.9086	-360	0	41					
14.94	12.29	14.58	14.26	13.82	12.61	12.68	12.53	
9.9095	-420	0	41					
14.77	12.24	14.64	14.64	13.82	12.82	13.43	12.79	

Table A11 (continued).

Date	Xpos	Ypos	Aper.					
BC	CN	C ₃	CO ⁺	VC	C ₂	RC	H ₂ O ⁺	
9.9108	-480	0	41					
15.14	12.46	14.79	14.64	13.82	13.03	12.77	12.64	
9.9121	-540	0	41					
14.77	12.57	14.78	14.73	13.73	13.24	13.43	12.93	
9.9130	-600	0	41					
15.38	12.60	15.15	14.95	14.13	13.20	13.87	13.02	
9.9338	0	0	41					
11.27	9.15	9.94	10.71	9.95	9.01	9.01	8.87	
9.9347	60	0	41					
13.21	10.02	11.78	12.65	11.90	10.07	11.03	10.88	
9.9361	120	0	41					
14.23	10.99	13.34	13.85	12.96	11.02	12.11	11.97	
9.9371	180	0	41					
14.88	11.53	14.41	15.05	13.56	11.68	12.76	12.70	
9.9386	240	0	41					
15.32	11.93	15.11	16.11	14.38	12.30	13.11	13.54	
9.9395	300	0	41					
15.62	12.14	16.10	15.80	14.99	12.70	13.86	14.06	

Table A11 (continued).

Date	Xpos	Ypos	Aper.				
BC	CN	C ₃	CO ⁺	VC	C ₂	RC	H ₂ O ⁺
9.9410	360	0	41				
16.06	12.61	15.85	15.79	14.75	13.10	-1.00	-1.00
9.9418	420	0	41				
16.81	12.71	16.41	16.10	14.74	13.47	14.61	14.82
9.9451	480	0	41				
16.80	12.90	16.40	17.29	16.49	13.63	-1.00	15.57
9.9465	540	0	41				
16.80	13.46	16.08	-1.00	-1.00	14.04	15.36	16.32
9.9474	600	0	41				
16.79	13.61	16.08	-1.00	16.48	14.44	-1.00	-1.00
9.9512	0	0	41				
11.19	9.13	9.96	10.70	9.97	9.00	9.00	8.90
9.9527	0	0	41				
11.23	9.14	9.98	10.70	9.99	9.02	9.04	8.90
9.9718	0	0	41				
11.25	9.20	10.04	10.77	10.02	9.07	9.07	8.97
9.9728	0	-60	41				
13.23	10.13	11.97	12.92	12.13	10.21	11.33	11.12

Table A11 (continued).

Date	Xpos	Ypos	Aper.					
BC	CN	C ₃	CO ⁺	VC	C ₂	RC	H ₂ O ⁺	
9.9741	0	-120	41					
14.29	10.92	13.28	13.82	13.04	10.96	11.93	11.99	
9.9750	0	-180	41					
15.16	11.39	14.19	14.36	13.30	11.68	12.55	12.22	
9.9764	0	-240	41					
15.15	11.75	14.80	14.61	14.32	12.20	13.39	13.10	
9.9774	0	-300	41					
14.90	12.12	15.23	15.27	14.32	12.69	15.33	13.80	
9.9793	0	-360	41					
16.64	12.35	15.22	15.70	14.93	12.98	13.59	14.18	
9.9796	0	-420	41					
-1.00	12.54	15.53	15.46	15.67	13.41	15.33	-1.00	
9.9810	0	-480	41					
15.44	12.76	17.47	16.00	-1.00	13.63	15.33	13.91	
9.9820	0	-540	41					
-1.00	12.85	15.52	-1.00	16.42	13.98	15.33	16.29	
9.9833	0	-600	41					
15.86	13.05	15.52	-1.00	15.67	14.26	14.57	-1.00	

Table A11 (continued).

Date	Xpos	Ypos	Aper.					
BC	CN	C ₃	CO ⁺	VC	C ₂	RC	H ₂ O ⁺	
9.9869	0	0	41					
11.35	9.17	10.01	10.71	10.05	9.06	9.03	8.92	
9.9917	0	0	41					
11.23	9.17	9.99	10.71	10.00	9.03	9.04	8.90	
9.9926	0	60	41					
12.88	9.67	11.30	12.38	11.57	9.79	10.77	10.60	
9.9941	0	120	41					
14.15	10.51	12.73	13.45	12.94	10.68	11.96	11.75	
9.9950	0	180	41					
14.77	11.22	13.82	14.76	13.69	11.44	12.93	12.59	
9.9966	0	240	41					
16.51	11.81	14.89	15.02	15.19	12.13	13.80	13.03	
9.9976	0	300	41					
16.49	12.15	15.12	16.38	15.62	12.47	15.31	14.02	
9.9994	0	360	41					
-1.00	12.38	15.42	16.36	14.87	13.02	14.11	14.53	
10.0003	0	420	41					
16.47	12.56	17.37	17.12	16.37	13.09	-1.00	14.33	

Table A11 (continued).

Date	Xpos	Ypos	Aper.					
BC	CN	C ₃	CO ⁺	VC	C ₂	RC	H ₂ O ⁺	
10.0017	0	480	41					
14.96	12.77	17.35	-1.00	-1.00	13.70	15.30	15.08	
10.0026	0	540	41					
-1.00	12.98	-1.00	-1.00	-1.00	14.20	15.30	-1.00	
10.0039	0	600	41					
-1.00	12.91	16.58	-1.00	-1.00	14.32	15.30	-1.00	
10.0064	0	0	41					
11.31	9.16	9.96	10.70	9.99	9.01	9.00	8.87	

Table A12. Reduced magnitudes for the night of May 11th 1986.

Date	Xpos	Ypos	Aper.	BC	CN	C ₃	CO ⁺	VC	C ₂	RC	H ₂ O ⁺
11.9198			41		0	0					
11.41	10.18	10.10	10.96	10.16	9.25	9.26	9.14				
11.9212			41		0	0					
11.51	10.20	10.16	10.97	10.28	9.26	9.27	9.17				
11.9281			62		0	0					
10.94	9.54	9.62	10.45	9.78	8.59	8.76	8.69				
11.9296			62		0	0					
10.96	9.51	9.57	10.49	9.77	8.61	8.79	8.65				
11.9422			28		0	0					
11.92	10.84	10.57	11.39	10.65	9.83	9.64	9.56				
11.9435			28		0	0					
11.97	10.84	10.59	11.37	10.71	9.83	9.68	9.58				

Table A13. Reduced magnitudes for the night of May 13th 1986.

Date	Xpos	Ypos	Aper.	BC	CN	C ₃	CO ⁺	VC	C ₂	RC	H ₂ O ⁺
13.9515			41		0	0					
	11.61	9.89	10.72	11.20	10.42	9.58	9.38	9.28			
13.9530			41		-60	0					
	13.16	10.61	12.40	12.99	12.21	10.48	11.39	11.11			
13.9537			41		-60	-60					
	13.91	10.71	12.79	13.14	12.53	10.61	11.82	11.54			
13.9546			41		0	-60					
	13.46	10.52	12.31	12.95	12.18	10.44	11.46	11.09			
13.9698			41		0	0					
	11.78	10.03	10.82	11.35	10.53	9.66	9.54	-1.00			
13.9708			41		60	-60					
	14.09	10.71	12.65	13.45	12.57	10.68	11.53	11.32			
13.9723			41		60	0					
	13.64	10.50	12.25	13.04	12.10	10.47	11.37	11.03			
13.9762			41		60	60					
	13.88	10.64	12.92	13.85	12.89	10.72	12.41	11.89			
13.9777			41		0	60					
	13.72	10.44	12.37	13.19	12.19	10.51	11.65	11.10			

Table A13 (continued).

Date	Xpos	Ypos	Aper.					
BC	CN	C ₃	CO ⁺	VC	C ₂	RC	H ₂ O ⁺	
13.9784	-60	60	41					
14.47	10.77	12.84	13.45	12.54	10.78	11.86	11.67	
13.9793	-120	60	41					
14.76	10.98	13.46	13.93	12.87	11.19	13.05	11.99	
13.9878	0	0	41					
11.94	10.02	10.83	11.28	10.52	9.67	9.60	9.38	
13.9895	-120	0	41					
13.90	10.92	13.42	13.95	12.93	11.03	12.57	11.65	
13.9912	-180	0	41					
15.08	11.39	14.11	14.04	13.30	11.58	12.84	12.31	
13.9919	-240	0	41					
15.81	11.92	14.76	14.48	13.73	12.23	13.20	12.68	
13.9928	120	0	41					
-1.00	10.84	13.67	14.46	13.28	11.05	13.43	12.29	
13.9943	180	0	41					
15.02	11.42	13.97	16.40	14.46	11.72	13.74	12.79	
13.9982	0	-60	41					
14.21	10.79	12.85	13.48	12.74	10.69	11.77	11.66	

Table A13 (continued).

Date	Xpos	Ypos	Aper.					
BC	CN	C ₃	CO ⁺	VC	C ₂	RC	H ₂ O ⁺	
13.9997	60	-60	41					
15.69	11.00	13.15	14.22	12.84	10.95	12.03	11.94	
14.0014	120	-60	41					
14.90	11.21	13.97	15.10	14.15	11.30	12.62	12.62	
14.0030	180	-60	41					
-1.00	11.68	15.05	15.10	14.69	11.99	14.12	13.70	
14.0038	-60	-60	41					
14.42	10.87	13.23	13.57	12.80	10.92	11.73	11.74	
14.0047	-120	-60	41					
-1.00	11.06	13.66	14.00	13.07	11.11	12.07	12.03	
14.0061	-180	-60	41					
-1.00	11.42	13.81	14.29	13.60	11.46	12.47	12.29	
14.0131	0	-180	41					
-1.00	11.27	15.18	15.36	13.82	11.35	12.68	12.78	
14.0140	-60	-120	41					
14.63	11.35	14.25	14.92	13.48	11.43	13.28	12.22	
14.0153	-120	-120	41					
14.61	11.36	14.39	14.88	13.79	11.68	12.66	12.56	

Table A13 (continued).

Date	Xpos	Ypos	Aper.					
BC	CN	C ₃	CO ⁺	VC	C ₂	RC	H ₂ O ⁺	
14.0163	-180	-120	41					
-1.00	11.83	14.81	14.88	13.59	12.12	12.81	12.55	
14.0177	-240	-120	41					
15.29	12.39	14.53	14.28	14.50	12.60	12.80	12.09	
14.0186	-300	-120	41					
13.75	12.58	14.76	16.02	14.16	13.10	12.79	12.88	

Abstract

This work is concerned with the study of the coma and gas tail of Halley's Comet. The thesis begins with a summary of the relevant background material. Theories of origin are discussed, after which the known properties of cometary comae, nuclei and tails are described.

Narrow-band photometry of Halley's Comet both pre- and post-perihelion is documented. The observations of the OH band at 3080\AA are discussed first, as it is a product of H_2O . Production rates and lifetimes against photodissociation are calculated using both the Haser Model and the Average Random Walk Model.

The variation of production rates of CN, C_2 and C_3 are discussed in the light of current knowledge of Halley's nucleus. Photodestruction lifetimes of these trace species are found using a Monte-Carlo modelling technique.

The analysis of large-scale image of the plasma tail of Halley is described, resulting in the determination of the solar wind velocity at the comet. The dynamics of the ions in the tail are demonstrated using a simple analytical approximation to the magnetic field structure. Observations of discrete plasma formations within the tail allow the measurement of the internal velocity field, from which an estimate of the tail magnetic field strength is derived.